

12

AD A122888

Detection of High-Altitude Missile Exhaust Plumes at Submillimeter Wavelengths

G. C. LIGHT and P. F. ZITTEL
Chemistry and Physics Laboratory
The Aerospace Corporation
El Segundo, Calif. 90245

25 October 1982

APPROVED FOR PUBLIC RELEASE:
DISTRIBUTION UNLIMITED

ORIGINAL COPY

Prepared for
SPACE DIVISION
AIR FORCE SYSTEMS COMMAND
Los Angeles Air Force Station
P.O. Box 92960, Worldway Postal Center
Los Angeles, Calif. 90009

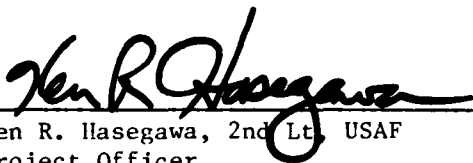
DTIC
JAN 3 1983
H

82 12 30 053

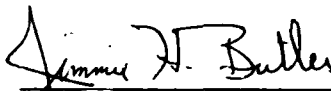
This report was submitted by The Aerospace Corporation, El Segundo, CA 90245, under Contract No. F04701-82-C-0083 with the Space Division, Deputy for Technology, P.O. Box 92960, Worldway Postal Center, Los Angeles, CA 90009. It was reviewed and approved for The Aerospace Corporation by S. Feuerstein, Director, Chemistry and Physics Laboratory. Lt K. R. Hasegawa, SD/YLVM, was the project officer for the Mission-Oriented Investigation and Experimentation (MOIE) Program.

This report has been reviewed by the Public Affairs Office (PAS) and is releasable to the National Technical Information Service (NTIS). At NTIS, it will be available to the general public, including foreign nations.

This technical report has been reviewed and is approved for publication. Publication of this report does not constitute Air Force approval of the report's findings or conclusions. It is published only for the exchange and stimulation of ideas.

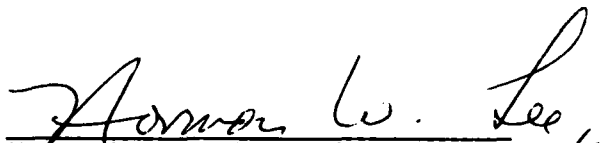


Ken R. Hasegawa, 2nd Lt, USAF
Project Officer



Jimmie H. Butler, Colonel, USAF
Director of Space Systems Technology

FOR THE COMMANDER


Norman W. Lee, Jr., Col, USAF
Deputy for Technology

UNCLASSIFIED

SECURITY CLASSIFICATION OF THIS PAGE (When Data Entered)

REPORT DOCUMENTATION PAGE		READ INSTRUCTIONS BEFORE COMPLETING FORM
1. REPORT NUMBER SD-TR-82-84	2. GOVT ACCESSION NO. AD-A122888	3. RECIPIENT'S CATALOG NUMBER
4. TITLE (and Subtitle) DETECTION OF HIGH-ALTITUDE MISSILE EXHAUST PLUMES AT SUBMILLIMETER WAVELENGTHS		5. TYPE OF REPORT & PERIOD COVERED
		6. PERFORMING ORG. REPORT NUMBER TR-0083(3945-04)-1
7. AUTHOR(s) Glenn C. Light and Paul F. Zittel		8. CONTRACT OR GRANT NUMBER(s) F04701-82-C-0083
9. PERFORMING ORGANIZATION NAME AND ADDRESS The Aerospace Corporation El Segundo, Calif. 90245		10. PROGRAM ELEMENT, PROJECT, TASK AREA & WORK UNIT NUMBERS
11. CONTROLLING OFFICE NAME AND ADDRESS Space Division Air Force Systems Command Los Angeles, Calif. 90009		12. REPORT DATE 25 October 1982
		13. NUMBER OF PAGES 90
14. MONITORING AGENCY NAME & ADDRESS (if different from Controlling Office)		15. SECURITY CLASS. (of this report) Unclassified
		15a. DECLASSIFICATION DOWNGRADING SCHEDULE
16. DISTRIBUTION STATEMENT (of this Report) Approved for public release; distribution unlimited.		
17. DISTRIBUTION STATEMENT (of the abstract entered in Block 20, if different from Report)		
18. SUPPLEMENTARY NOTES		
19. KEY WORDS (Continue on reverse side if necessary and identify by block number)		
Atmospheric interaction with plume	Clutter	
Atmospheric radiation	Earth limb	
Background radiation	557 GHz	
Calculated background spectra	High altitude	
Calculation of detectability	Parametric calculations	
	Physical and optical model	
20. ABSTRACT (Continue on reverse side if necessary and identify by block number)		
Studies are described of the detectability of low-thrust, high-altitude rocket motor plumes based on observation of their optical properties at submillimeter wavelengths. The report describes the physical and optical model for a high-altitude plume. The model includes a first approximation for the effects of interaction with a tenuous atmosphere. Results are presented for plume signature and its dependence on motor and plume parameters and on viewed-scene variables. A signal-to-noise calculation is presented.		

DD FORM 1473 (FACSIMILE)

UNCLASSIFIED
SECURITY CLASSIFICATION OF THIS PAGE (When Data Entered)

UNCLASSIFIED

SECURITY CLASSIFICATION OF THIS PAGE(When Data Entered)

19. KEY WORDS (Continued)

Plume signature	Submillimeter wavelengths
Pure rotational transitions	Variation in atmospheric properties
Signal-to-noise	Water vapor
Small-scale spatial structure	
Small thrust rocket plumes	

20. ABSTRACT (Continued)

Earth atmospheric structure relevant to the issue of background clutter is discussed. Results are presented of calculated background properties for different distributions of atmospheric properties and different viewing geometries. The effects are described of small-scale spatial structure at the mesopause.

It is tentatively concluded that low-thrust plumes can be observed at high altitudes by this technique. A number of issues that require further study are presented.

UNCLASSIFIED

SECURITY CLASSIFICATION OF THIS PAGE(When Data Entered)

CONTENTS

I. INTRODUCTION..... 7

II. ANTENNA TEMPERATURE CALCULATIONS..... 9

 A. Model..... 9

 B. Calculated Antenna Temperatures..... 14

 C. Signal-to-Noise Estimate..... 20

III. BACKGROUND RADIATION FROM THE ATMOSPHERE..... 25

 A. Atmospheric Structure..... 25

 B. Calculations of Background Radiation for
 Scales >1000 km..... 30

 C. Background Signature Variability at
 Smaller Scale Sizes..... 79

IV. CONCLUSIONS..... 83

V. ISSUES REQUIRING FURTHER STUDY..... 85

 A. Critical Issues..... 85

 B. Other Issues..... 87

REFERENCES..... 89

Accession For	
NTIS GRA&I	<input checked="" type="checkbox"/>
DTIC TAB	<input type="checkbox"/>
Unannounced	<input type="checkbox"/>
Justification	
By _____	
Distribution/	
Availability Codes	
Dist	Special
A	



FIGURES

1.	Rotational Energy Levels of Water.....	8
2.	The Plume Model.....	10
3.	Antenna Temperature Definition.....	12
4.	Plume Signal vs. Thrust.....	15
5.	Plume Signal vs. Plume Rotational Temperature.....	17
6.	Plume Signal vs. Field of View.....	18
7.	Plume Signal vs. Thrust, Viewed against Deep Space.....	19
8.	Plume Signal vs. Frequency.....	21
9.	Signal-to-Noise Calculation.....	22
10.	Schematic Latitude-Height Section of Zonal Mean Temperature at the Solstices.....	27
11.	Fourier Decomposition of Mean 50 mb Geopotential Height, Jan. 1958.....	28
12.	Atmospheric Temperature Distributions.....	32
13.	Atmospheric Humidity Distributions.....	33
14.	Altitude vs. Frequency at Fixed Optical Depth (= 0.1054).....	34
15.	Altitude vs. Frequency at Fixed Optical Depth (= 0.6931).....	35
16.	Altitude vs. Frequency at Fixed Optical Depth (= 1.022).....	36
17.	Altitude vs. Frequency at Fixed Optical Depth (= 2.303).....	37
18.	Altitude vs. Frequency at Fixed Optical Depth (= 4.605).....	38
19.	Altitude vs. Frequency at Fixed Optical Depth (= 6.908).....	39

FIGURES (Continued)

20. Altitude vs. Frequency at Fixed Optical Depth (≈ 10.0).....	40
21. Integrated Path Spectral Radiance.....	41
22. Radiance Contribution Profile for 18.57699 cm^{-1}	42
23. Cumulative Radiance Profile for 18.57699 cm^{-1}	43
24. Radiance Contribution Profile for 18.57709 cm^{-1}	44
25. Cumulative Radiance Profile for 18.57709 cm^{-1}	45
26. Radiance Contribution Profile for 18.57719 cm^{-1}	46
27. Cumulative Radiance Profile for 18.57719 cm^{-1}	47
28. Radiance Contribution Profile for 18.57729 cm^{-1}	48
29. Cumulative Radiance Profile for 18.57729 cm^{-1}	49
30. Radiance Contribution Profile for 18.57739 cm^{-1}	50
31. Cumulative Radiance Profile for 18.57739 cm^{-1}	51
32. Radiance Contribution Profile for 18.57749 cm^{-1}	52
33. Cumulative Radiance Profile for 18.57749 cm^{-1}	53
34. Radiance Contribution Profile for 18.57759 cm^{-1}	54
35. Cumulative Radiance Profile for 18.57759 cm^{-1}	55

FIGURES (Continued)

36. Radiance Contribution Profile for 18.57770 cm^{-1}	56
37. Cumulative Radiance Profile for 18.57770 cm^{-1}	57
38. Distribution of the Altitude of Peak Apparent Radiance with Doppler Shift from Line Center.....	59
39. Distribution of the Depth of the Emitting Layer with Doppler Shift from Line Center.....	60
40. Background Spectra for Various Model Atmospheres.....	61
41. Earth Limb Background Spectra.....	63
42. Radiance Contribution Profile for 18.57699 cm^{-1}	64
43. Cumulative Radiance Profile for 18.57699 cm^{-1}	65
44. Slant Path Radiance Profile for 18.57699 cm^{-1}	66
45. Radiance Contribution Profile for 18.57710 cm^{-1}	67
46. Cumulative Radiance Profile for 18.57710 cm^{-1}	68
47. Slant Path Radiance Profile for 18.57710 cm^{-1}	69
48. Radiance Contribution Profile for 18.57720 cm^{-1}	70
49. Cumulative Radiance Profile for 18.57720 cm^{-1}	71
50. Slant Path Radiance Profile for 18.57720 cm^{-1}	72
51. Radiance Contribution Profile for 18.57730 cm^{-1}	73

FIGURES (Continued)

52. Cumulative Radiance Profile for 18.57730 cm^{-1}	74
53. Slant Path Radiance Profile for 18.57730 cm^{-1}	75
54. Radiance Contribution Profile for 18.57760 cm^{-1}	76
55. Cumulative Radiance Profile for 18.57760 cm^{-1}	77
56. Slant Path Radiance Profile for 18.57760 cm^{-1}	78
57. Effect on Background Spectra of Variation in Mesopause Temperature.....	81
58. Altitude at Which Optical Depth is 1.0.....	86

TABLES

1. Thrust Required to Give S/N = 1 with Plume at 500 km Altitude.....	23
2. Conditions of Calculations.....	31

I. INTRODUCTION

The exhaust of a typical amine-fueled rocket motor contains a large mole fraction of H_2O vapor that can be cooled to very low temperatures ($\sim 50^\circ K$) during supersonic expansion. At high altitudes, where collisions with the ambient atmosphere are infrequent, the low temperature of exhaust species may persist many kilometers from the motor. Such a cloud of cold H_2O vapor can significantly attenuate the earth background radiation ($\sim 250^\circ K$ blackbody) at wavelengths corresponding to transitions between low-lying rotational states of H_2O . Alternatively, when viewed against the cold ($\sim 4^\circ K$) background of space, the cloud can be a significant emission source at the same wavelengths. In either case, the submillimeter optical properties of the cold plume may provide the basis for passive detection of low-thrust motors at high altitudes.

This scheme has been discussed at some length already by M. Litvak (Ref. 1 provides details). It is the purpose of this report to provide an independent assessment of the feasibility of the scheme, to extend the work already published, and to suggest certain issues that need more attention.

Figure 1 shows the rotational energy levels of the H_2O molecule, with solid lines indicating the allowed dipole transitions. At low temperatures, only the lowest levels are significantly populated ($kT_R \approx 33 \text{ cm}^{-1}$ for $T_R \approx 50^\circ K$). This study is primarily concerned with the 557-GHz ($\lambda = 0.539 \text{ mm}$) transition between the 1_{10} and 1_{01} rotational levels of H_2O .

Section II is devoted to describing the physical and optical model of a high-altitude plume and to presenting results of parametric calculations using this model. Section III discusses the characteristics of earth background radiation at the signal frequency and presents calculated background properties. Section IV presents conclusions from this study and Section V gives a brief and not necessarily exhaustive list of issues that require further study.

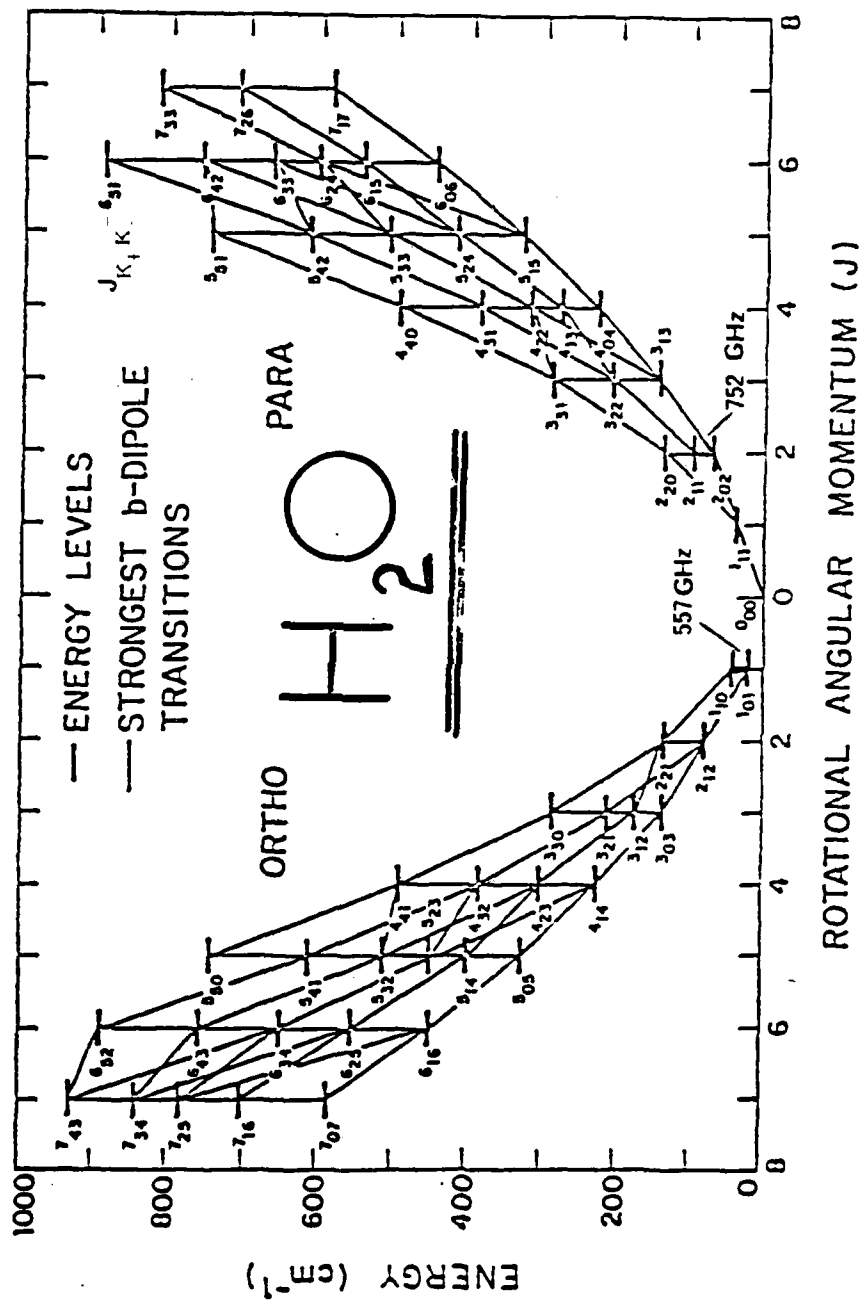


Fig. 1. Rotational Energy Levels of Water

II. ANTENNA TEMPERATURE CALCULATIONS

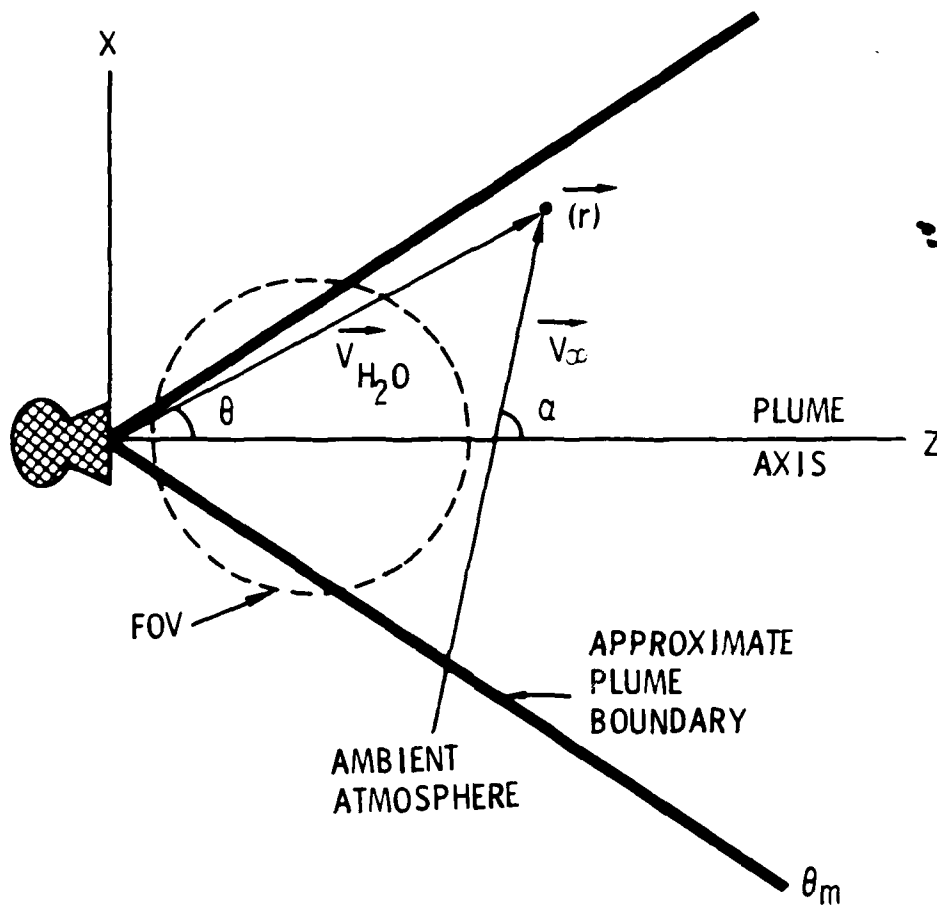
Section II. A outlines a model for describing the submillimeter absorption (and emission) properties of a typical high-altitude plume. The model is generally applicable to a variety of cold plume molecules and rotational transitions, although the discussion focuses on the 557-GHz transition of H_2O . The chosen figure of merit for plume detection is the antenna temperature T_A , which is defined to be directly proportional to the change in energy falling on a detector as a result of the introduction of the plume into the detector field of view against a blackbody background.

Section II. B reports a parametric study of the dependence of antenna temperature, or detectability, on various system parameters, including motor thrust, rotational temperature, detector field of view, etc. A brief consideration of the signal-to-noise ratio expected for a heterodyne detection system is also presented.

A. MODEL

Figure 2 schematically depicts a high-altitude plume in a coordinate system fixed on the rocket motor. Exhaust species including H_2O (~ 42 mole % for an Aerozine 50/ N_2O_4 -fueled motor) are emitted from the motor at high velocity ($v_{H_2O} = 3.2$ km/sec), but low rotational and translational temperature ($\sim 50^\circ K$). The angular distribution of exhaust density about the plume axis is frequently described by the Hill-Draper or Brook models for supersonic expansion into a vacuum, but for convenience is described in our calculations as independent of θ for $\theta < \theta_m = 38^\circ$ and proportional to the inverse square of distance from the motor. The use of different exhaust models has a minor effect on calculated antenna temperature. The ambient atmosphere ($> 90\%$ oxygen atoms above 300 km) streams into the plume at the vehicle speed ($v_w = 6$ km/sec), making an angle α with the thrust axis, which is characteristic of the vehicle attitude (i.e., $\alpha = 0^\circ$ implies forward thrust).

The effect of the ambient wind on the rotational temperature of the plume is modeled in a simple way. Since the relative translational energy between a plume molecule and a wind molecule is from 10^3 to 10^4 times the rotational



COLLISIONAL HEATING:

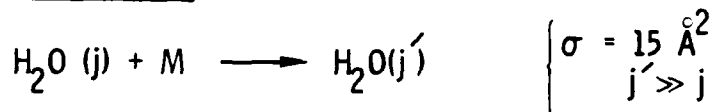


Fig. 2. The Plume Model

energy spacing of the low rotational levels of H_2O , it is assumed that a hard-sphere collision ($\sigma_{h.s.} = 15 \text{ \AA}^2$) promotes the water molecule to a high rotational state and effectively removes it from further consideration. For the viewing geometries considered, the rates of radiative and collisional cooling at high altitudes are insufficient to return a highly excited molecule to the low rotational levels of interest before the molecule exits a typical field of view fixed near the motor exit. For simplicity, it is assumed that only wind molecules that have not previously suffered a collision with a plume molecule can create such a rotational excitation. This assumption underestimates to some extent the deleterious effect of wind "heating" on the plume.

The mathematical formalism that describes the penetration of the wind into the plume, and consequently the density \hat{n}_{H_2O} of uncollided, or rotationally cold, H_2O molecules at each point in space within the plume, is straightforward. Such "first-collision, molecular flow" models have been utilized frequently in connection with collisional vibrational excitation of plume species under essentially single-collision conditions.

From the density distribution of uncollided H_2O molecules within the plume, one can determine the necessary optical characteristics of the plume at the relevant submillimeter wavelengths. An important parameter is the optical depth τ along a line of sight through the plume. In all calculations reported here, the line of sight is perpendicular to the plume axis (i.e., along the y-axis in Fig. 2). It is also assumed that the line of sight is perpendicular to the vehicle velocity vector (i.e., \vec{v}_∞ is in the x-z plane in Fig. 2), although this second assumption is easily relaxed (see Sec. II. B). τ is defined in the standard way by Eq. (4) in Fig. 3 and is clearly a function of frequency and location in the x-z plane. The absorption coefficient at each point along the line of sight (i.e., $\alpha(\nu, \vec{r})$) is determined from spectroscopic constants for the line of interest. The absorption lines are assumed to be Doppler broadened with a translational temperature of $T_T = 20^\circ\text{K}$ and appropriately shifted by the component of \vec{v}_{H_2O} along the line of sight. The line strength of the 557-GHz absorption of H_2O is taken to be 1.93×10^{-18} cm/molecule for $T_R = 50^\circ\text{K}$ and is easily calculated for other rotational temperatures. Since the thermal Doppler width of the absorption line at any

Antenna Temperature Definition

$$T_A = \frac{c^2}{2k\nu^2} [B_{B+S}^c - B_B^c] \quad (1)$$

$$B_B^c = \begin{cases} \text{"BRIGHTNESS" OF BACKGROUND} \\ \frac{2h\nu^3}{c^2} \cdot \frac{1}{e^{h\nu/kT_B} - 1} & \frac{\text{Watts}}{\text{cm}^2 \cdot \text{Hz} \cdot \text{sr}} \end{cases} \quad (2)$$

$$B_{B+S}^c = \begin{cases} \text{"BRIGHTNESS" OF BACKGROUND PLUS SOURCE} \\ B_B^c e^{-\tau} + \frac{2h\nu^3}{c^2} \cdot \frac{1}{e^{h\nu/kT_S} - 1} \cdot (1 - e^{-\tau}) \end{cases} \quad (3)$$

$$\tau(\nu) = \int_{-\infty}^{\infty} \hat{n}_{H_2O}(\vec{r}) \cdot \alpha(\nu, \vec{r}) \cdot dy \quad (4)$$

$$T_A \approx (T_S - T_B) \cdot (1 - e^{-\tau}) \quad \text{for } T_B, T_S \gg \frac{h\nu}{k} \quad (5)$$

Fig. 3. Antenna Temperature Definition

point in the plume (i.e., $\gamma_D \approx 0.2$ MHz hwhm) is much smaller than the range of Doppler shifts throughout the plume (i.e., ± 4 MHz), it is clear that only molecules in a small range of locations contribute to absorption at a particular frequency. For a broadside viewing geometry, for example, only those molecules close to the x-z plane of Fig. 2 contribute to absorption at the unshifted line center frequency, $\nu_0 = 556.91$ GHz. The assumed translational temperature of uncollided H_2O molecules is not critical to the calculation of τ as long as $\gamma_D < 4$ MHz.

The optical depth of the plume allows one to calculate the effect of interposing the plume between a background blackbody source and a distant observer tuned to detect radiant energy at frequency ν . Eq. (1) of Fig. 3 defines an antenna temperature T_A that is directly proportional to the change in spectral "brightness," a spectral steradiancy, as a result of the interposition of a plume with optical depth τ and temperature T_S ($= T_R$ for this application) in front of a background blackbody at temperature T_B . The antenna temperature is a function of frequency and the observer's line of sight by way of the optical depth τ . For a given field of view (FOV) (Fig. 2), the antenna temperature is averaged over the field of view. The resulting temperature is directly proportional to the change in spectral power, ΔP (watts/Hz), incident on a distant detector that subtends a solid angle Ω_{Det} and views an area A_{FOV} , i.e.,

$$\Delta P = \frac{2 \, k \nu^2}{c^2} A_{FOV} \Omega_{Det} T_A \quad (6)$$

T_A is clearly negative for occultation of a warm background by a cooler plume, and positive for emission by a plume against a cooler background.

It should be noted that for typical radio frequency applications where both T_B and T_S are $\gg h\nu/k$, the antenna temperature is simply related in Eq. (5) of Fig. 3 to optical depth and background and source temperatures. This relationship is not precisely correct for submillimeter wavelengths and low background temperatures. The useful definition of T_A in terms of radiant energy in Eqs. (1) through (4) is maintained in these calculations.

A final comment on the radiative lifetime of the 557-GHz transition of H_2O is necessary. The Einstein coefficients of the transition are calculated from the line strength to be $A_{ul} = 3.3 \times 10^{-3} \text{ sec}^{-1}$ and $B_{ul} = 3.1 \times 10^{18} \text{ cm}^3/\text{erg sec}^2$. Thus, the spontaneous lifetime for the transition is $\sim 300 \text{ sec}$ and the lifetime for induced emission and absorption for molecules near an infinite blackbody at $\sim 300^\circ\text{K}$ is $\sim 55 \text{ sec}$. Both times are much longer than the transit time ($\sim 1 \text{ sec}$) for plume molecules across a typical field of view positioned near a motor. Thus, spontaneous and induced radiative processes should not significantly alter rotational populations, or calculated antenna temperatures.

B. CALCULATED ANTENNA TEMPERATURES

The model described in Sec. II. A has been used to calculate antenna temperatures for typical high-altitude plumes. The dependence of T_A on several important motor and observational parameters is investigated. In all calculations, a typical low-thrust, liquid-fueled (Aerozine 50/ N_2O_4) motor is used. The viewing geometry is perpendicular to the plume axis and vehicle velocity vector (Fig. 2). With noted exceptions, the FOV is 3 km in diameter, centered on the plume axis, and adjusted along the axis to obtain the optimum FOV-averaged antenna temperature. For a 3-km FOV, the optimum invariably occurred when the FOV was centered 1.5 to 2.0 km downstream from the motor. The thrust, or attack, angle α was 90° in all calculations. The calculations are relatively insensitive to α at altitudes above 300 km. With noted exceptions, all calculations were made for the unshifted line center frequency $\nu_0 = 556.92 \text{ GHz}$, which is optimum for broadside viewing. The dependence of T_A on frequency is considered briefly. The translational temperature (not necessarily equal to the rotational temperature) of the plume is assumed to be 20°K , although calculations are essentially insensitive to the assumed value up to large translational temperatures. With a noted exception, the plume is viewed against a blackbody background at 250°K .

Figure 4 shows the dependence of T_A on thrust level at two different altitudes. At 500 km the ambient atmosphere is too thin to collisionally "heat" the plume ($\lambda_{\text{mean free path}} \approx 250 \text{ km}$), and T_A ceases to change with

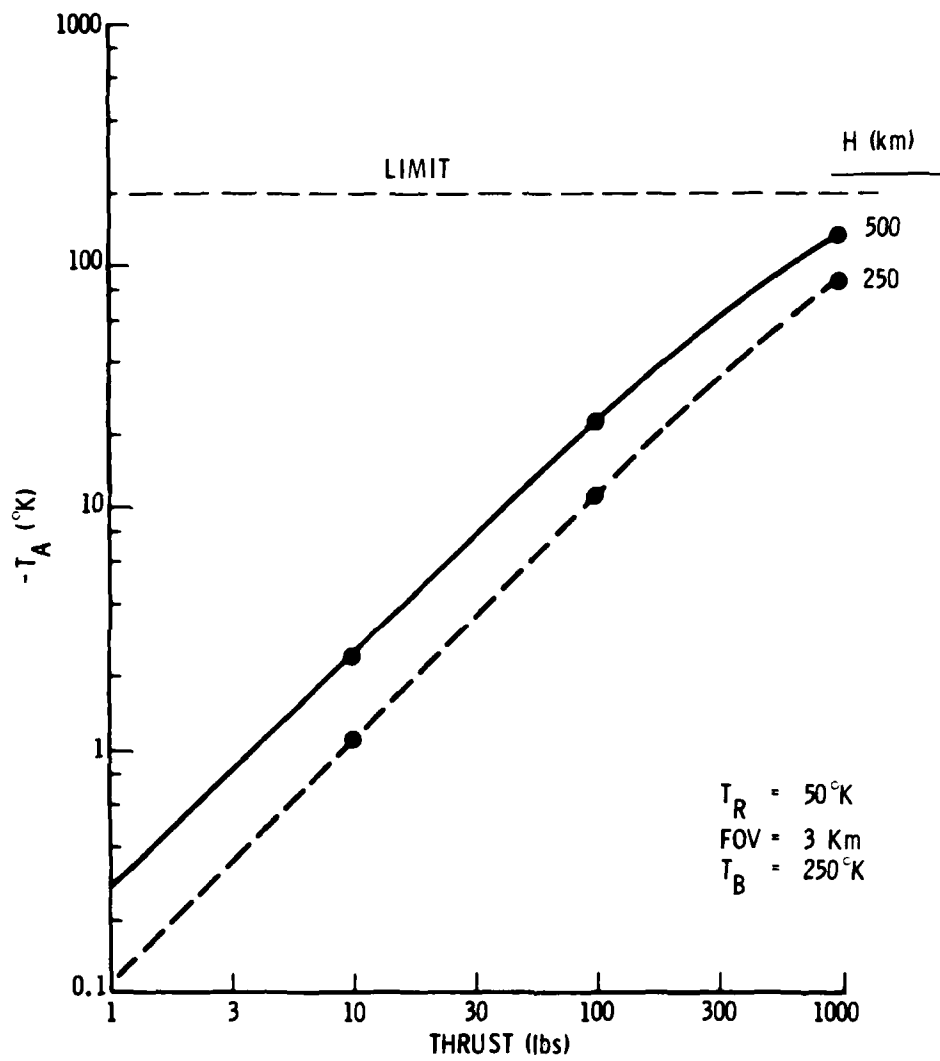


Fig. 4. Plume Signal vs. Thrust

increasing altitude. Below 250 km ($\lambda_{\text{mfp}} < 3$ km), collisional heating quickly reduces T_A . Figure 4 shows that T_A depends linearly on thrust until the plume becomes optically thick over the FOV. For an optically dense plume, T_A eventually approaches the limiting value, equal to $T_R - T_B$ ($\approx -200^\circ\text{K}$).

Figure 5 shows the dependence of antenna temperature on the assumed rotational temperature T_R (i.e., the rotational temperature of the supersonically expanded exhaust gases prior to atmospheric collisions). A rotational temperature of 50°K is frequently assumed, or calculated, for the supersonic expansion into vacuum of small motor exhausts; however, actual temperatures may depend to some extent on thrust level, fuel, and motor design. The rotational temperature is a critical parameter because of its strong effect on the relative populations of the rotational levels connected by the radiative transition.

Figure 6 illustrates the dependence of T_A on the detector field of view. Smaller fields of view can be positioned closer to the motor, where the plume is denser and less perturbed by ambient collisions. Thus, larger (absolute magnitude) antenna temperatures are achievable. Fig. 6 also indicates the antenna size required to produce a diffraction-limited spot size equal to the assumed field of view at geosynchronous distance.

Calculated antenna temperatures depend on the temperature of the background against which the plume is viewed. A simple expression relates the antenna temperatures for two different background blackbody temperatures, T_B and \hat{T}_B ,

$$\frac{T_A(\hat{T}_B)}{T_A(T_B)} = \frac{e^{\frac{h\nu/k\hat{T}_B} - e^{\frac{h\nu/kT_R}}}{e^{\frac{h\nu/k\hat{T}_B} - 1}}}{\frac{e^{\frac{h\nu/kT_B} - 1}}{e^{\frac{h\nu/kT_B} - e^{\frac{h\nu/kT_R}}}}} \quad (7)$$

Eq. (7) may be used to convert antenna temperatures typically calculated at $T_B = 250^\circ\text{K}$ to other background temperatures. Figure 7 is a plot of T_A against motor thrust for a plume viewed against a cold sky (i.e., $T_B = 4^\circ\text{K}$) and is analogous to Fig. 4, which corresponds to viewing against the earth disk.

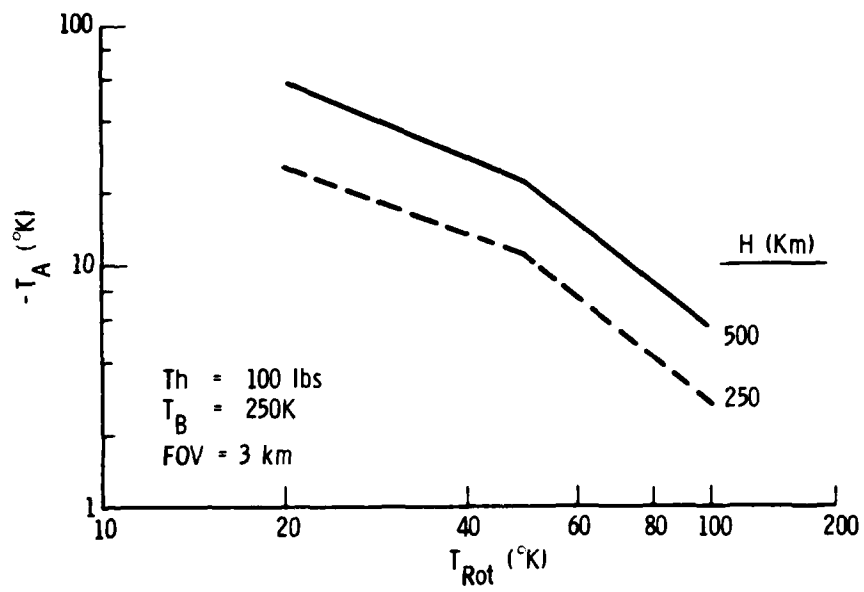


Fig. 5. Plume Signal vs. Plume Rotational Temperature

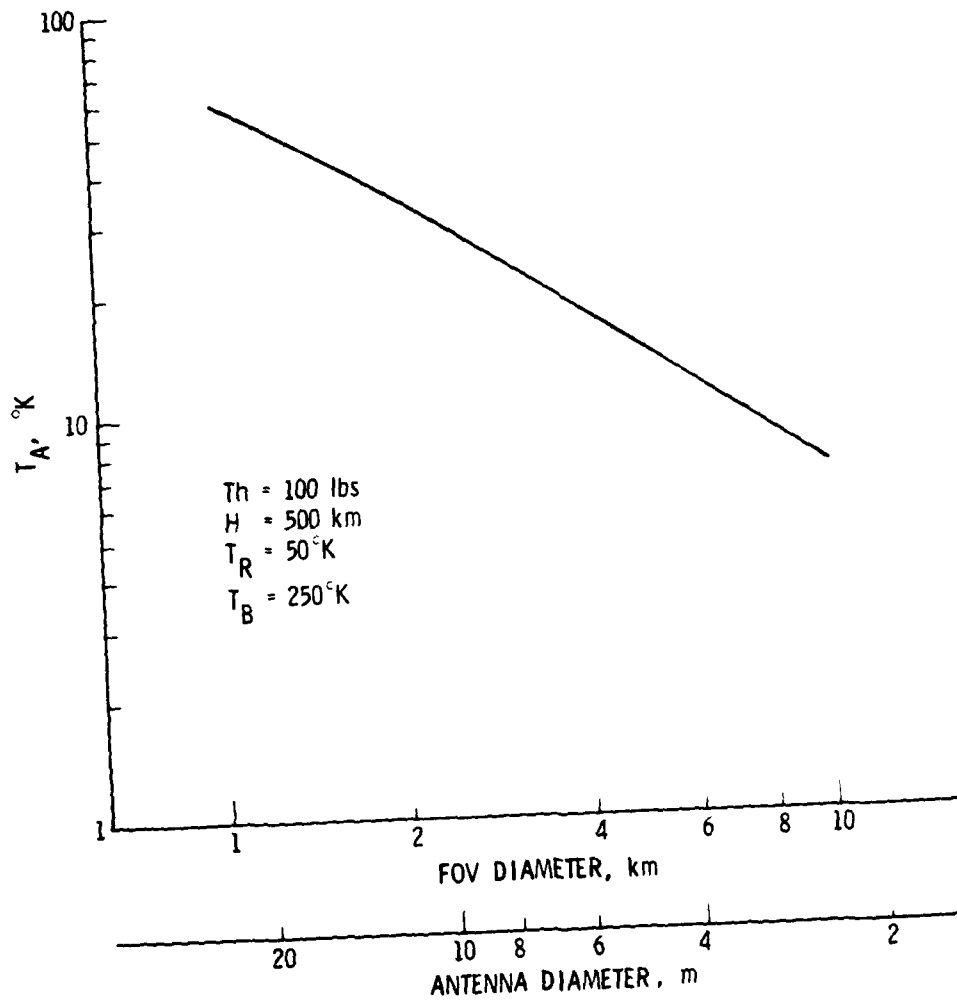


Fig. 6. Plume Signal vs. Field of View

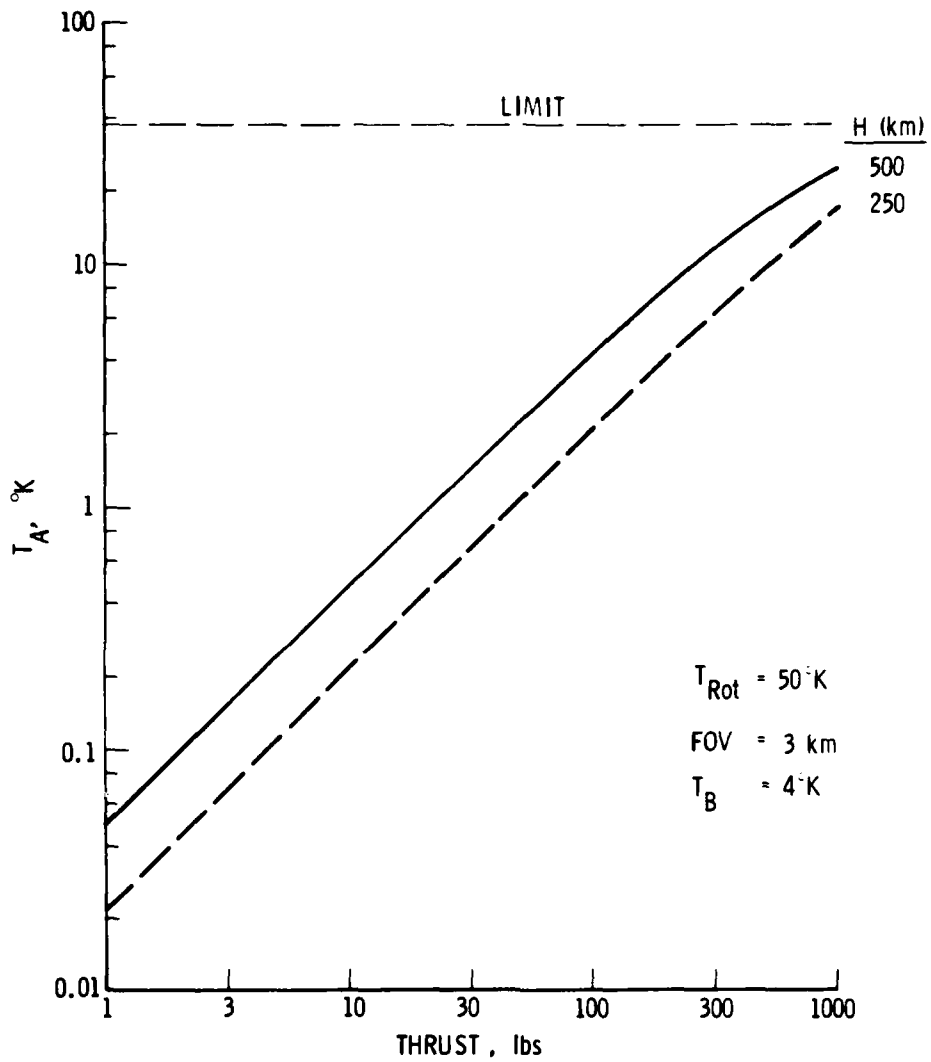


Fig. 7. Plume Signal vs. Thrust, Viewed against Deep Space

Against a 4°K background, the plume is seen in emission, and for a dense plume T_A approaches an upper limit approximately equal to the plume rotational temperature.

The optical depth of a plume, and thus the antenna temperature, depends on the observation frequency. In this study, calculations are generally made for the normal line center frequency ν_0 of the 557-GHz line, which is the optimum frequency for broadside viewing. Detectors, whether incoherent or heterodyne, accept a range of frequencies; thus, the spectral line shape of the absorption feature is important. Figure 8 shows antenna temperature as a function of frequency offset from line center for a typical plume. The optical depth of the plume is significant for frequency shifts up to the maximum Doppler shift of $\Delta\nu_m$ for those molecules emitted in the y-z plane with axis angle θ_m (Fig. 2). The calculated "lineshape" for T_A is to some extent a function of the model used for the dependence of plume density on the off-axis angle θ . The choice of a Hill-Draper, or Brook, plume model would result in a less sharp cutoff at $\Delta\nu_m$, but in a very similar line width and peak antenna temperature.

Viewing geometries that are not at 90° to both the plume axis and vehicle velocity are not specifically considered in our calculations. Results for viewing normal to the plume axis but non-normal to the vehicle velocity vector are, however, simply derived from our results. Antenna temperatures and lineshapes are essentially identical to the current results, but shifted in frequency by the Doppler component of the vehicle velocity along the line of sight. For a geostationary observer, the maximum line center shift for a terrestrial vehicle speed of ~ 6 km/sec is ~ 11 MHz. For viewing that is not normal to the plume axis, lineshapes may be complicated and not necessarily symmetrical about a Doppler-shifted line center frequency. The maximum line center Doppler shift for non-normal viewing is ~ 17 MHz.

C. SIGNAL-TO-NOISE ESTIMATE

Figure 9 displays a very rough estimate of the signal-to-noise ratio for a typical high-altitude plume observed against the earth, which is assumed to present a benign background, from geosynchronous orbit with a ~ 3-km FOV. The

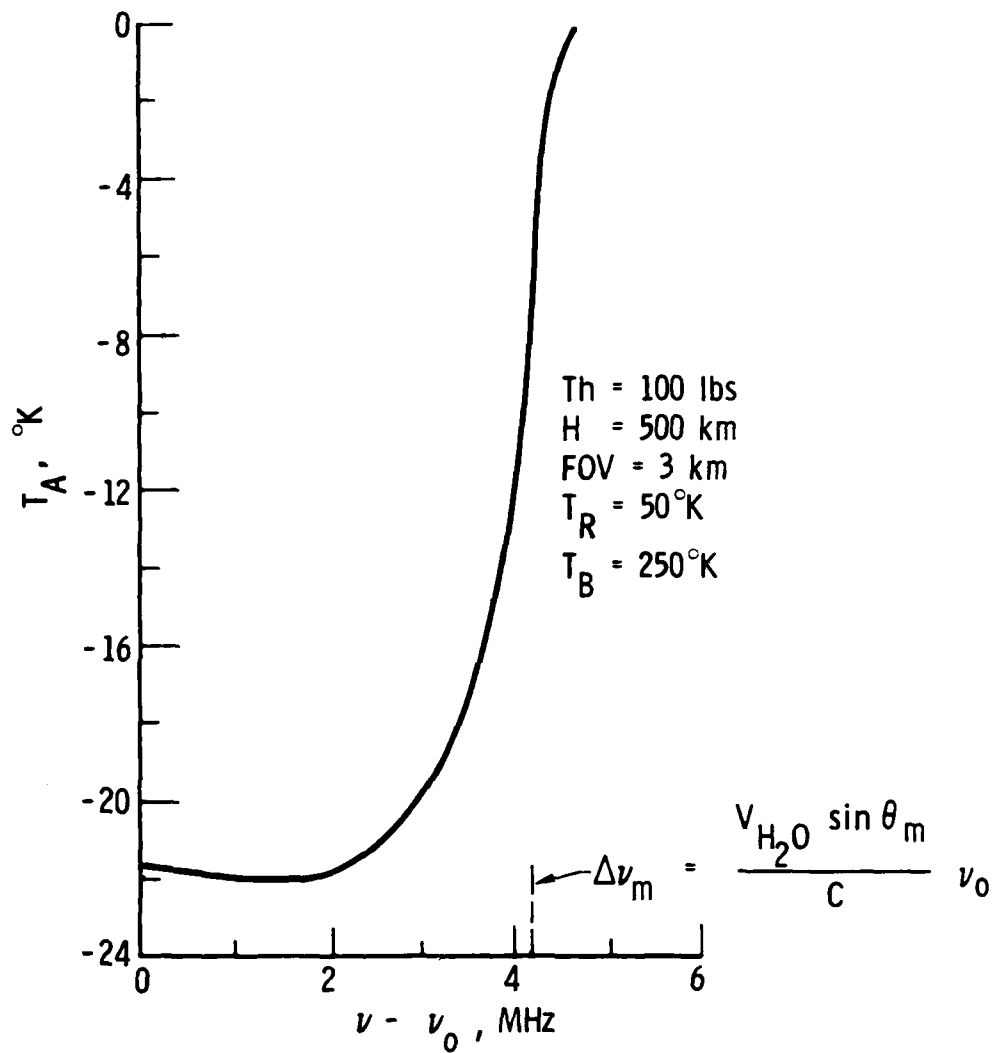


Fig. 8. Plume Signal vs. Frequency

SIGNAL-TO-NOISE OF COHERENT DETECTION SCHEME

$$\text{SIGNAL} = T_A \cdot \Delta\nu \cdot t$$

$$\text{NOISE} = T_{\text{sys}} \sqrt{\Delta\nu \cdot t}$$

$$\text{LET} \quad \left\{ \begin{array}{l} T_A = 20^\circ\text{K} \quad (\sim 100\text{-lb motor}) \\ \Delta\nu = 8 \text{ MHz} \\ t = 1 \text{ sec} \\ T_{\text{sys}} = 3000^\circ\text{K} \end{array} \right.$$

$$\text{THEN} \quad \frac{\text{SIGNAL}}{\text{NOISE}} = \frac{T_A}{T_{\text{sys}} \sqrt{\Delta\nu \cdot t}} = \frac{20^\circ\text{K}}{1^\circ\text{K}} = 20$$

$$\text{IF } t = 10^{-3} \text{ sec, then } \frac{\text{SIGNAL}}{\text{NOISE}} = 0.6$$

Fig. 9. Signal-to-Noise Calculation

intrinsic noise level of the heterodyne detection system is characterized by a system temperature T_{sys} (currently a few thousand degrees for submillimeter detectors). The IF bandpass of the detector is set equal to the full line-width of the absorption line, 8 MHz, over which T_A is roughly constant and equal to its peak value. In order to cover the maximum range of Doppler-shifted signal frequencies, this bandpass should be ~34 MHz. The use of 8 MHz assumes either a frequency scanning capability or a viewing geometry that entails less than the maximum Doppler shift. The dwell time t is roughly the transit time of the plume across the field of view and should be ~1 sec for a staring, or ~1 msec for a scanning, observational arrangement.

Using the system parameters defined in Fig. 9, the thrust levels required to produce a $S/N = 1$ with a benign background are presented in Table 1 for viewing above the horizon and below the horizon and for scanning and staring modes of observation.

Table 1. Thrust Required to Give $S/N = 1$ with Plume at 500 km Altitude

	Below Horizon	Above Horizon
Scanning ($t = 10^{-3}$ sec)	150 lbs	>1000 lbs
Staring ($t = 1$ sec)	4 lbs	25 lbs

Lower limits on detectability depend on the required observation mode, and on improvements in intrinsic detector noise for a heterodyne detection system.

III. BACKGROUND RADIATION FROM THE ATMOSPHERE

The basic question being addressed is: What is the variation of background radiation from place to place across the earth when viewed from space at and near the center of the particular water rotational lines of interest? In different terms, the problem is to evaluate the variations in atmospheric spectral radiance as the sensor field of view is scanned across the earth as viewed from outside the atmosphere. Spatial variation in background radiation will ultimately depend on the distributions of temperature, pressure, and humidity in the atmosphere along different representative lines of sight.

The answer to the question is expected to be complex and, in fact, not fully answerable at this time, owing to limited knowledge of atmospheric structure. As will be seen below, we are concerned with the region between about 35 km and 100 km altitude. This includes the entire mesosphere (~ 50 to 90 km), the upper portion of the stratosphere (35 to 50 km), and a little of the lower thermosphere (~ 90 to 100 km). In this region, there are phenomena leading to structure in atmospheric properties on all scale sizes from global to less than a typical plume size.

In Sec. III. A is presented a brief review of the elements of atmospheric structure in the altitude range of interest. In Sec. III. B are presented the results from calculations of radiative transfer using different models of atmospheric properties and different viewing geometries. This will give a broad picture of the characteristics of this background radiation and its variability on a global scale. In Sec. III. C the effects of atmospheric structure on a smaller physical scale are discussed.

A. ATMOSPHERIC STRUCTURE

Phenomena leading to atmospheric structure are discussed below, roughly in order of decreasing characteristic scale size. This section is a synopsis of information taken from several much more detailed discussions in the literature. (Refs. 2 through 5).

It is convenient to speak of the global atmospheric properties averaged over all longitudes, the "zonal mean" atmosphere, and deviations from this

mean. The zonal mean atmosphere is formed largely by the interplay of radiative transfer and induced fluid motions. The zonal mean atmosphere changes with an annual periodicity and with semiannual and weaker biennial periodicities. An example of zonal mean temperature distribution is shown in Fig. 10.

When the longitudinal dependence of atmospheric properties is examined, the first few Fourier components are called planetary waves. These first few Fourier components account for nearly all of the deviation from zonal mean values of atmospheric properties in the stratosphere, except on much smaller scale sizes. They are much stronger in the winter than in other seasons and are stronger in the stratosphere than the mesosphere. An example of planetary waves showing the results of Fourier decomposition into waves 1 through 4 is shown in Fig. 11. The plotted quantity is the altitude where the pressure is 50 mb for the Fourier components, which vary as $\sin\theta$, $\sin 2\theta$, $\sin 3\theta$, and $\sin 4\theta$, respectively, where θ is longitude.

There are tidal oscillations of the atmosphere generated in part gravitationally by the sun and moon, but in greater part thermally by the sun. In the upper atmosphere, the 24-h tide is of greatest importance. The tidal motion is vertical with wavelengths of 20 to 30 km. Its important effects are confined to latitudes less than 50° . There is also an important 12-h component near the mesopause.

To this point, the discussion has been concerned with components of atmospheric structure that, because of their large physical scale, probably will not contribute to variations in the background intensity during the observation of any one particular high-altitude missile. They may contribute, however, to differences between observed backgrounds at places separated by more than, say, 1000 km. Other components of atmospheric structure occur on a smaller scale, so that they could produce sensible background variations during one scan event. One of these is termed gravity waves. These are generated by a variety of sources, including aurorae, at high altitudes, and by tropospheric weather systems, jet streams, and tropospheric winds interacting with surface topography. They have a short period cut-off of about 5

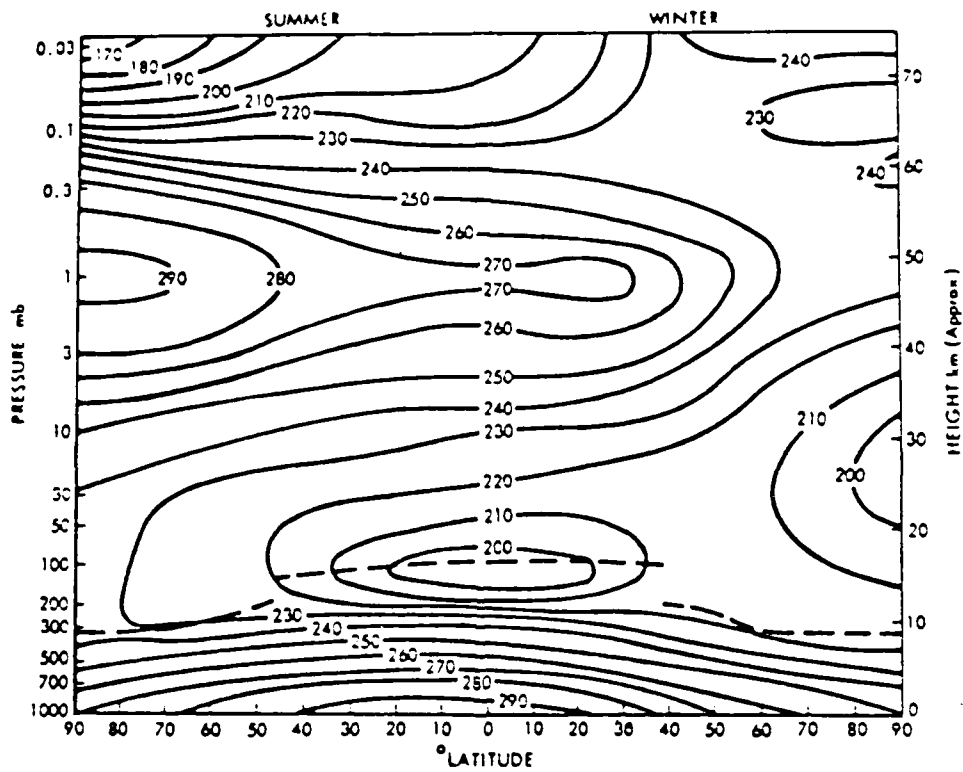


Fig. 10. Schematic Latitude-Height Section of Zonal Mean Temperature at the Solstices (Ref. 2)

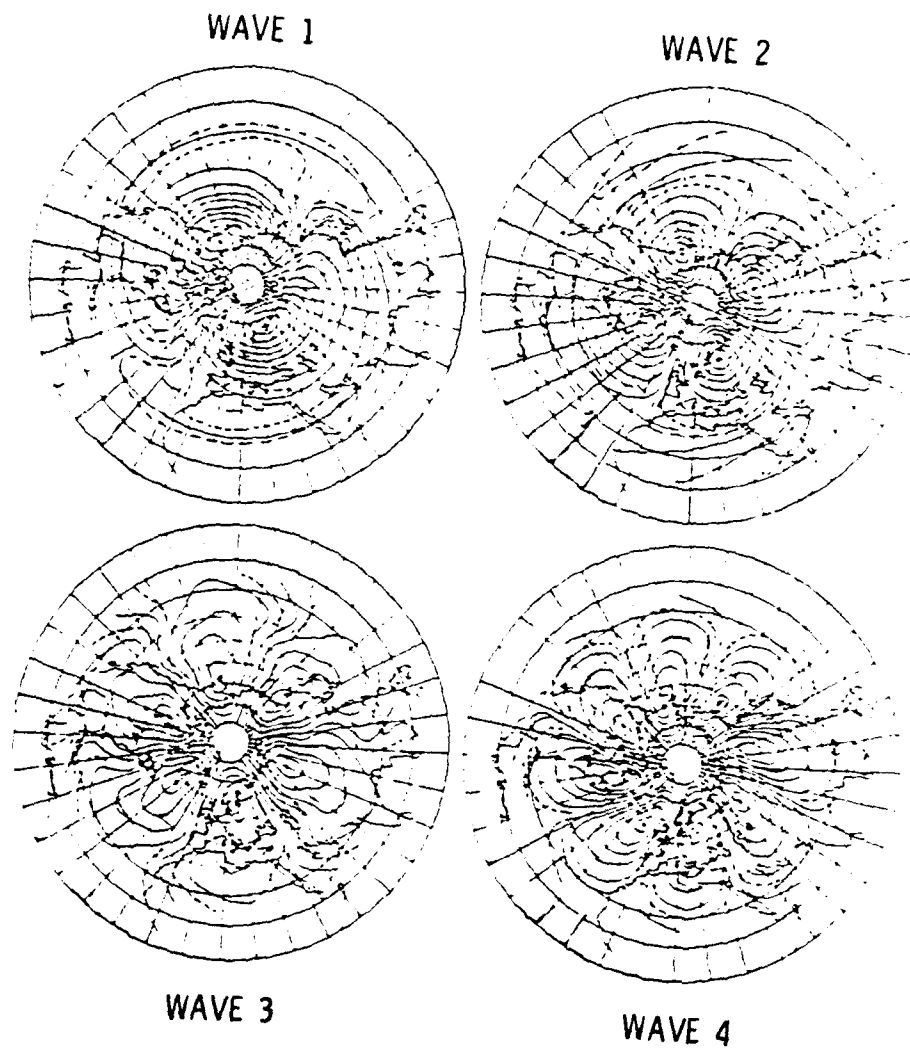


Fig. 11. Fourier Decomposition of Mean 50 mb Geopotential Height, Jan. 1958 (Ref. 2)

to 10 min in the upper mesosphere. The strongest waves have periods of 1 to 3 h. The horizontal scale size is 10 to 300 km and the vertical scale size is 5 to 50 km.

Gravity waves have been observed in meteor trail radar echoes, in VHF radar neutral backscatter data, in the luminosity patterns of noctilucent clouds and, in fact, have been photographed in the near-infrared through their influence on hydroxyl chemiluminescence. As these waves propagate vertically upward, they grow in amplitude owing to the decreasing atmospheric density and the requirement for conservation of energy flux. At some point near the mesopause, the waves tend to become unstable, undergoing nonlinear interactions leading to viscous dissipation and possibly to generation of turbulence.

Turbulence gives rise to the smallest scale variations in atmospheric properties of any of the mechanisms operating in the mesosphere and of potential importance to this problem. At the mesopause, scale sizes as small as ~ 50 m are to be expected and decreasing sizes occur with decreasing altitude. Turbulence has been observed at up to 105 km altitude in the trail of rocket-borne vapor releases and in meteor radar observations in the range 80 to 100 km. It is sporadic in time and space and is generally horizontally stratified.

The extent of detailed knowledge of these various mechanisms leading to structure in the atmosphere increases rapidly with the scale size. Earth satellites are unique in their ability to obtain global measurements on a repeated basis with regular sampling in space and time. Coverage is very good for large-scale processes that do not change rapidly in times of much less than a day. Our knowledge of the zonal mean atmosphere, its variation with the seasons, and planetary waves has developed over the last two decades almost entirely from these satellite observations. On the other hand, repeated and widespread use of radiosonde and sounding rocket atmospheric probes has given much information about the vertical distributions at many particular locations throughout the globe. In the context of the above discussion of structure-generating mechanisms, our knowledge of the extent, frequency, and intensity of gravity waves and turbulence in the upper

stratosphere and mesosphere is meager. It will not be possible to realistically describe the effects of these mechanisms on the background radiation. Instead the results of simple illustrative calculations will be reported.

B. CALCULATIONS OF BACKGROUND RADIATION FOR SCALES > 1000 km

It is necessary first to define the region of the atmosphere that gives rise to radiation seen as background by the proposed sensor system. We shall be describing results of calculations of radiative transfer in the atmosphere in a small frequency range centered on the water vapor rotational transition at 18.577 cm^{-1} . Other water vapor rotational transitions that have been discussed are expected to give similar background properties. The frequency range in the calculations is dictated largely by the range of Doppler shifts to be expected in an exhaust plume from a missile traveling at 6 km/sec. This corresponds to a frequency range of about $\pm .0006 \text{ cm}^{-1}$.

The calculations were performed by means of a set of versatile computer programs already in existence for computing the radiative properties of the atmosphere. These programs have been devised over a period of time by Dr. C. M. Randall to model numerous problems in atmospheric radiative transfer. The user specifies vertical distributions of pressure, temperature, and humidity in the atmosphere, as well as the viewing geometry. The program uses the AFGL Line Atlas to prescribe line positions, line strengths, pressure-broadening coefficients, and upper- and lower-state energy levels for finding Boltzmann population factors. Both pressure broadening and Doppler broadening were important in the altitude range of interest and so a Voigt line shape was used.

The program divides the atmosphere into a number of layers, each of which is assumed to be homogeneous. It then calculates the apparent spectral radiance of each layer as viewed by the sensor, consistent with absorption and stimulated emission in the intervening layers. Contributions to the spectral absorptivity from the far wings of distant pressure-broadened lines are included, but are not important in the frequency range of interest, which is narrowly confined to near the line center. The calculations of layer-by-layer

apparent spectral radiance are then manipulated in several different ways to illustrate the nature of the background radiation.

Calculations were done for three different models of temperature distribution and two different models of water vapor distribution, all shown graphically in Figs. 12 and 13. These were done in the combinations shown in Table 2. The U. S. Standard Atmosphere (Ref. 6) pressure distribution was used in all cases.

Table 2. Conditions of Calculations

Calculation No. (Case)	Temperature Distribution	Water Distribution	Line of Sight	Tangent Height (km)
1	Ref. 7	Ref. 9	Vertical	--
2	Ref. 6	Ref. 9	Vertical	--
3	Ref. 6	Ref. 10	Vertical	--
4	Ref. 8	Ref. 10	Vertical	--
5	Ref. 6	Ref. 10	Limb view	0
6	Ref. 6	Ref. 10	Limb view	90
7	Ref. 6	Ref. 10	Limb view	70
8)	} Ref. 6 but with depressed mesopause	Ref. 10	Vertical	--
9)		Ref. 10	Limb view	70

The three temperature distributions used represent examples of warm, cold, and mean mesospheric conditions. There is much uncertainty currently about the mesospheric water content. There are other models available that would undoubtedly give somewhat different radiance distributions than the ones we have used.

1. Viewing below the Earth Disc Horizon (Cases 1 to 5)

A set of computer-generated plots for calculation no. 3 (Table 2) is shown in Figs. 14 through 37. For this case, the U. S. Standard Atmosphere temperature distribution (Ref. 6) and the Crutzen-enhanced H₂O model (Ref. 10) were used. Figures 14 through 20 show the altitude at which different fixed values of optical depth are obtained as a function of frequency. Figure 21 shows the background apparent spectral radiance. Figures 22 through 37 show the distribution with altitude of apparent volumetric spectral emission and

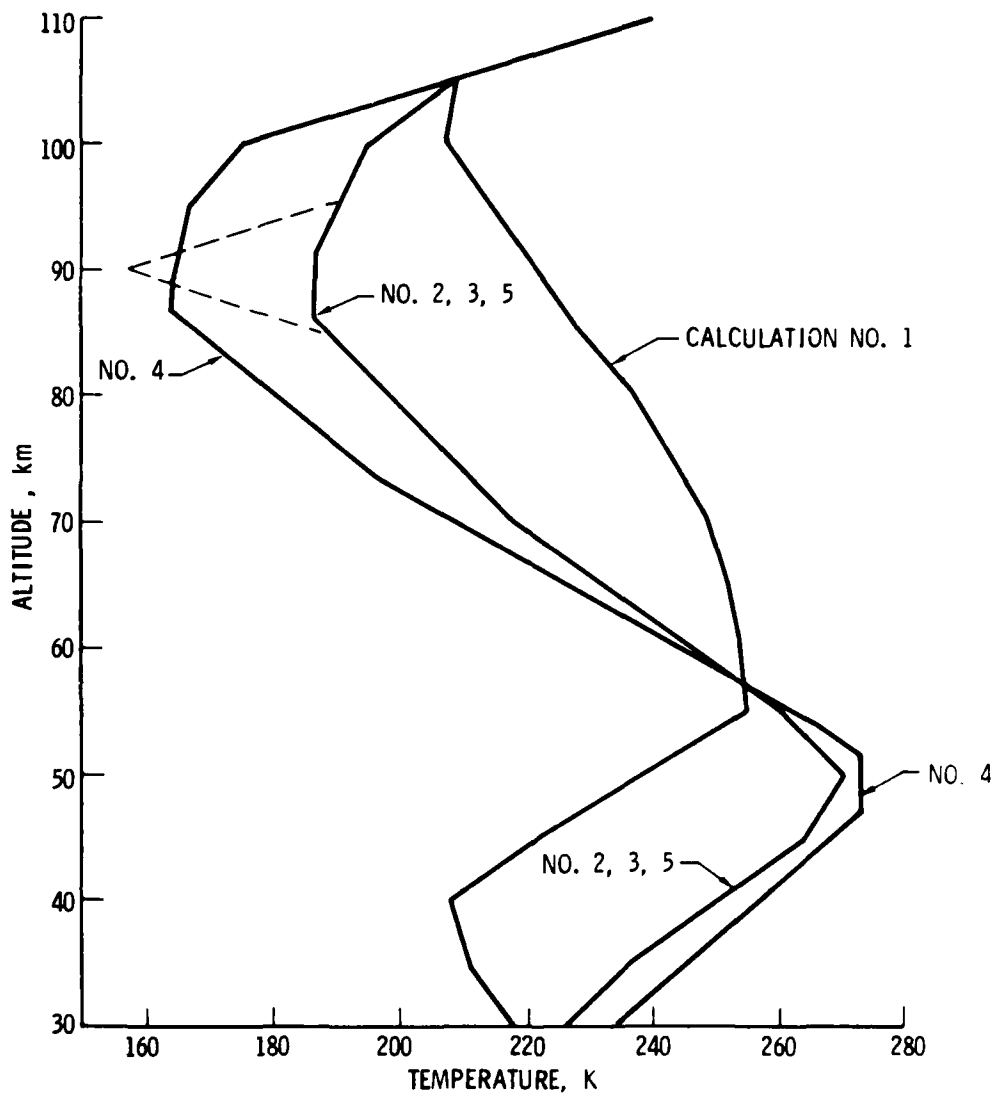


Fig. 12. Atmospheric Temperature Distributions

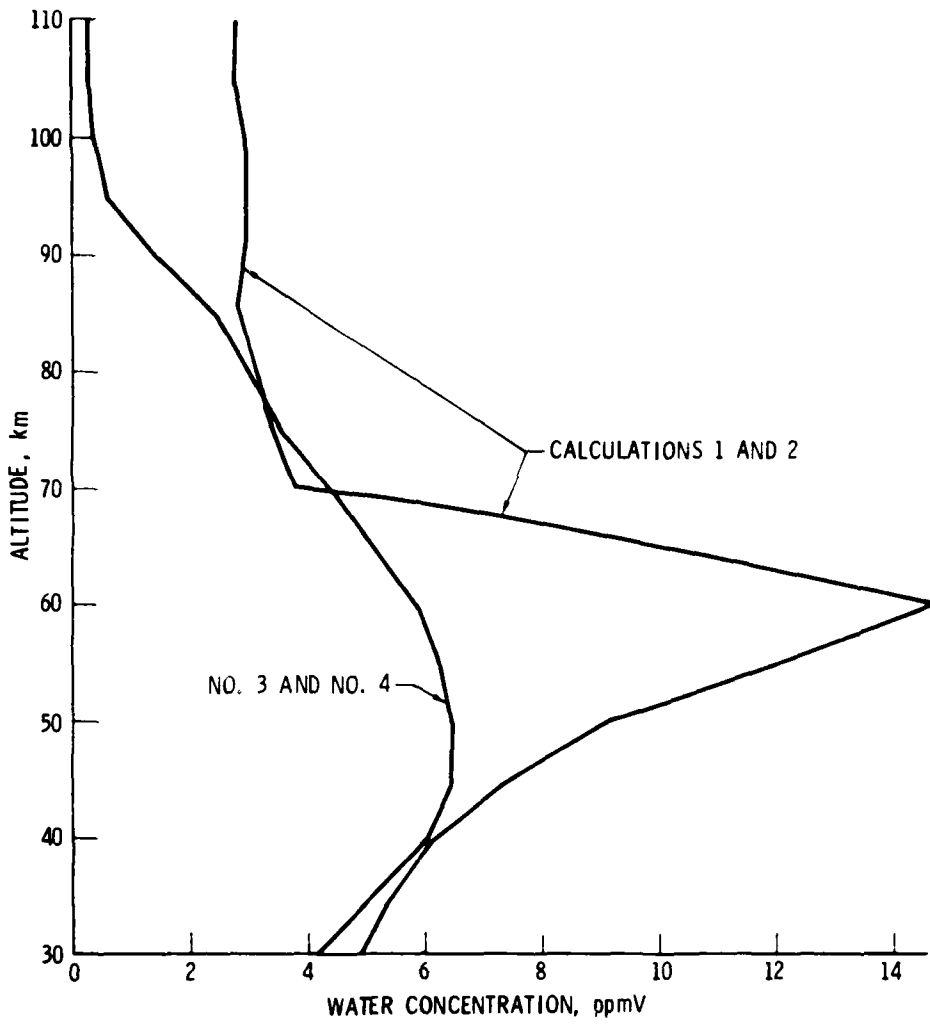
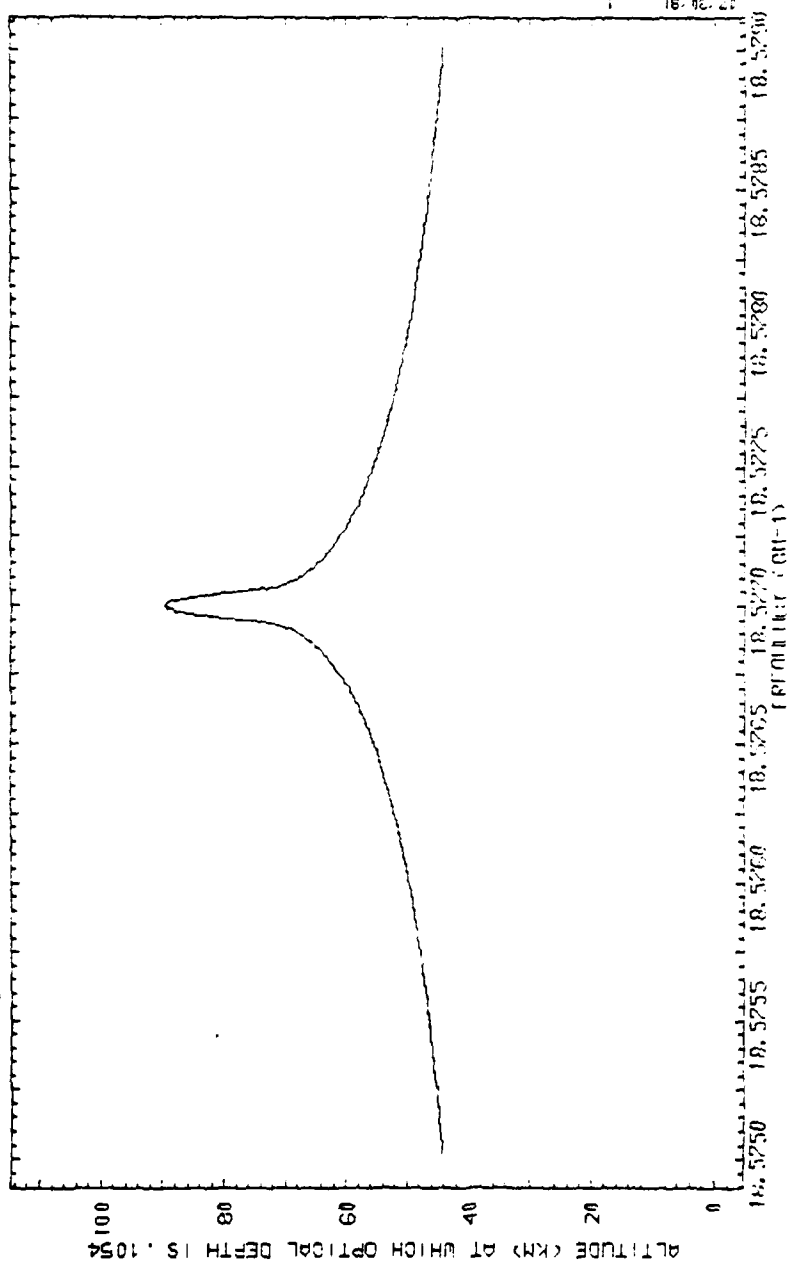


Fig. 13. Atmospheric Humidity Distributions

ALTITUDE AT FIXED OPTICAL DEPTH = 0.1054

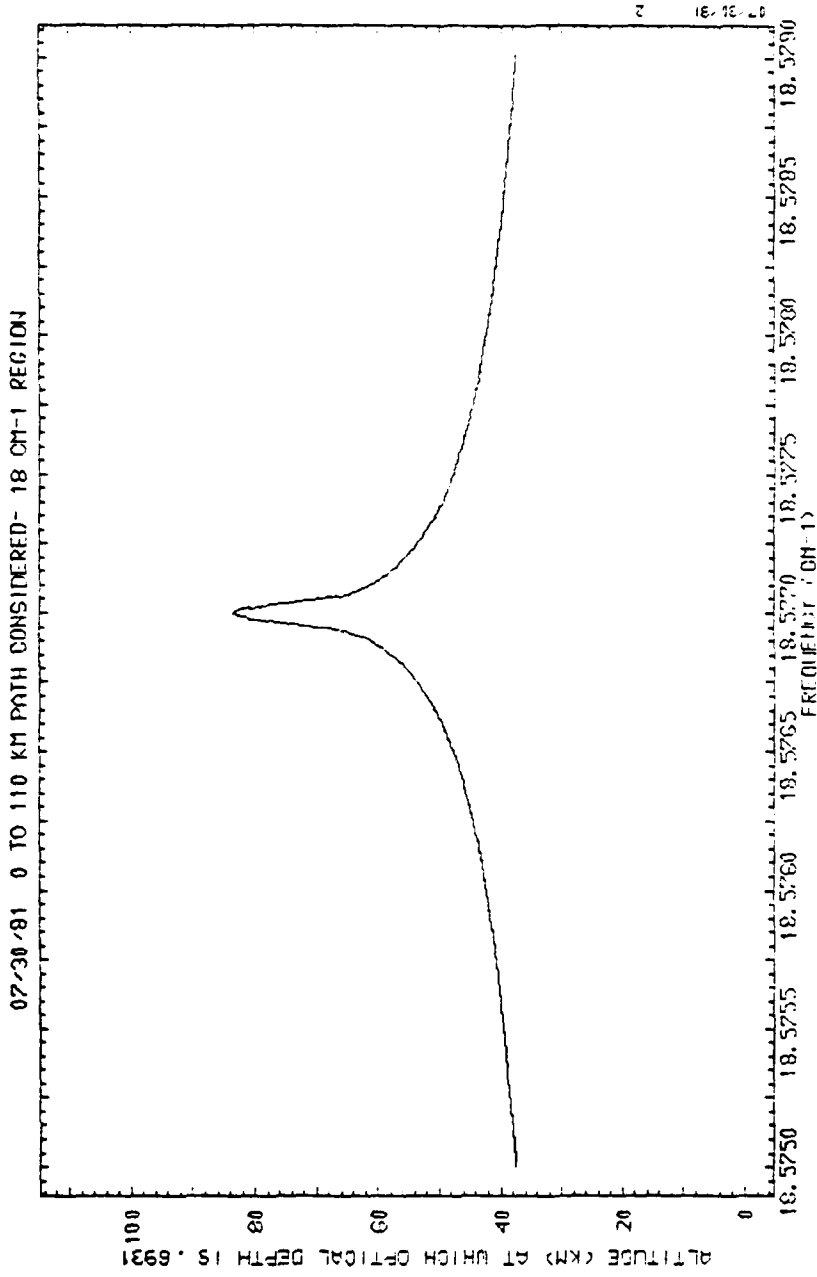
07-30-81 0 TO 110 KM PATH CONSIDERED- 18 CM-1 REGION



OPTICAL PATH CONSIDERED WAS FROM 0.0000 TO 110.0000 KM

Fig. 14. Altitude vs. Frequency at Fixed Optical Depth (= 0.1054)

OPTICAL DEPTH = 0.6931

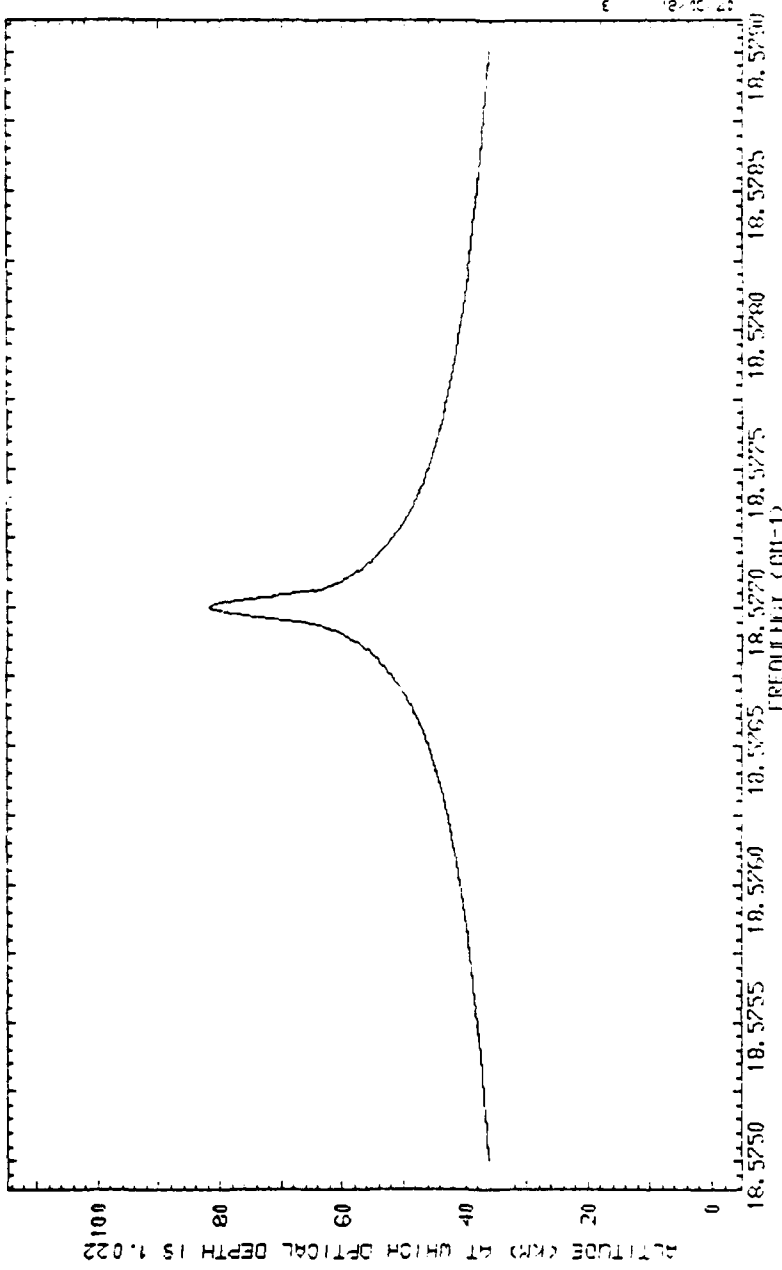


OPTICAL PATH CONSIDERED WAS FROM 0.0000 TO 110.0000 KM

Fig. 15. Altitude vs. Frequency at Fixed Optical Depth (= 0.6931)

OPTICAL DEPTH = 1.022

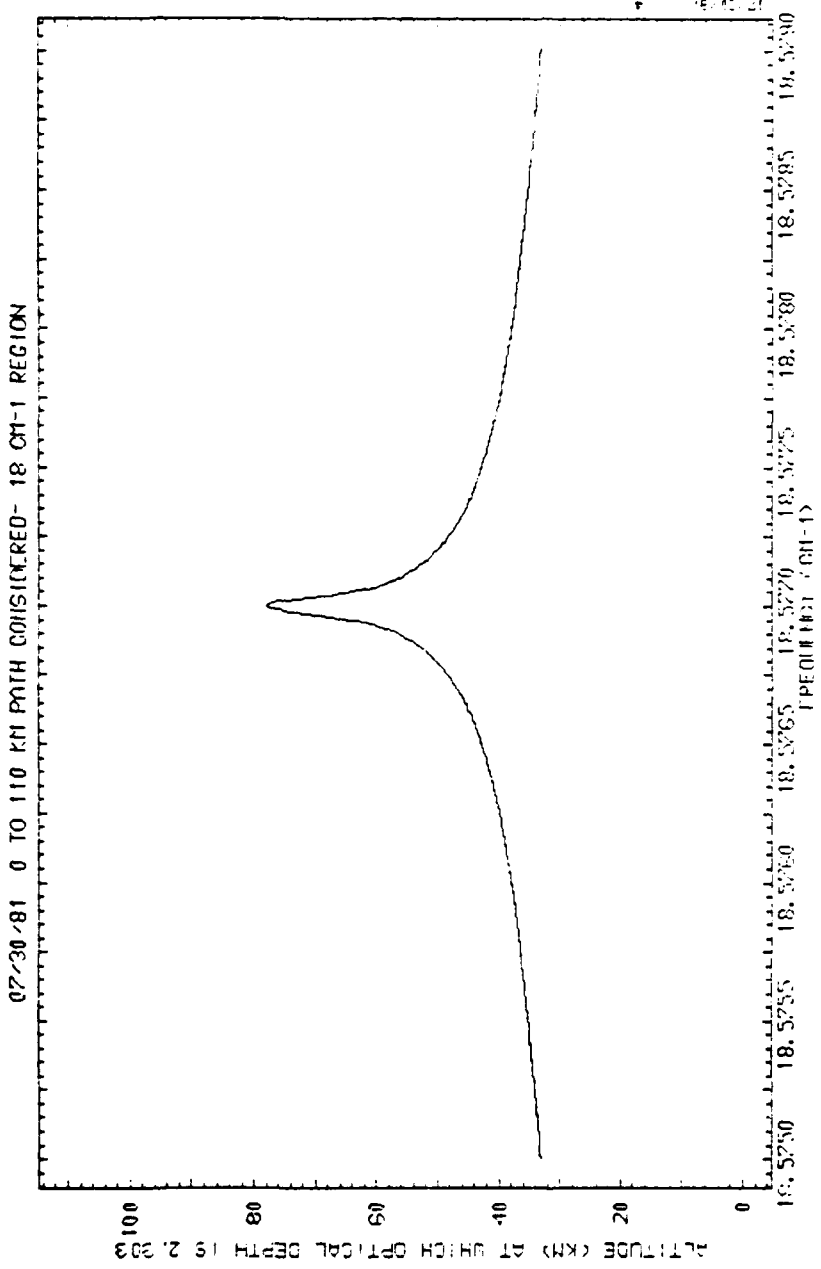
07/30/81 0 TO 110 KM PATH CONSIDERED - 18 CM-1 REGION



OPTICAL PATH CONSIDERED WAS FROM 0.0000 TO 110.0000 KM

Fig. 16. Altitude vs. Frequency at Fixed Optical Depth (= 1.022)

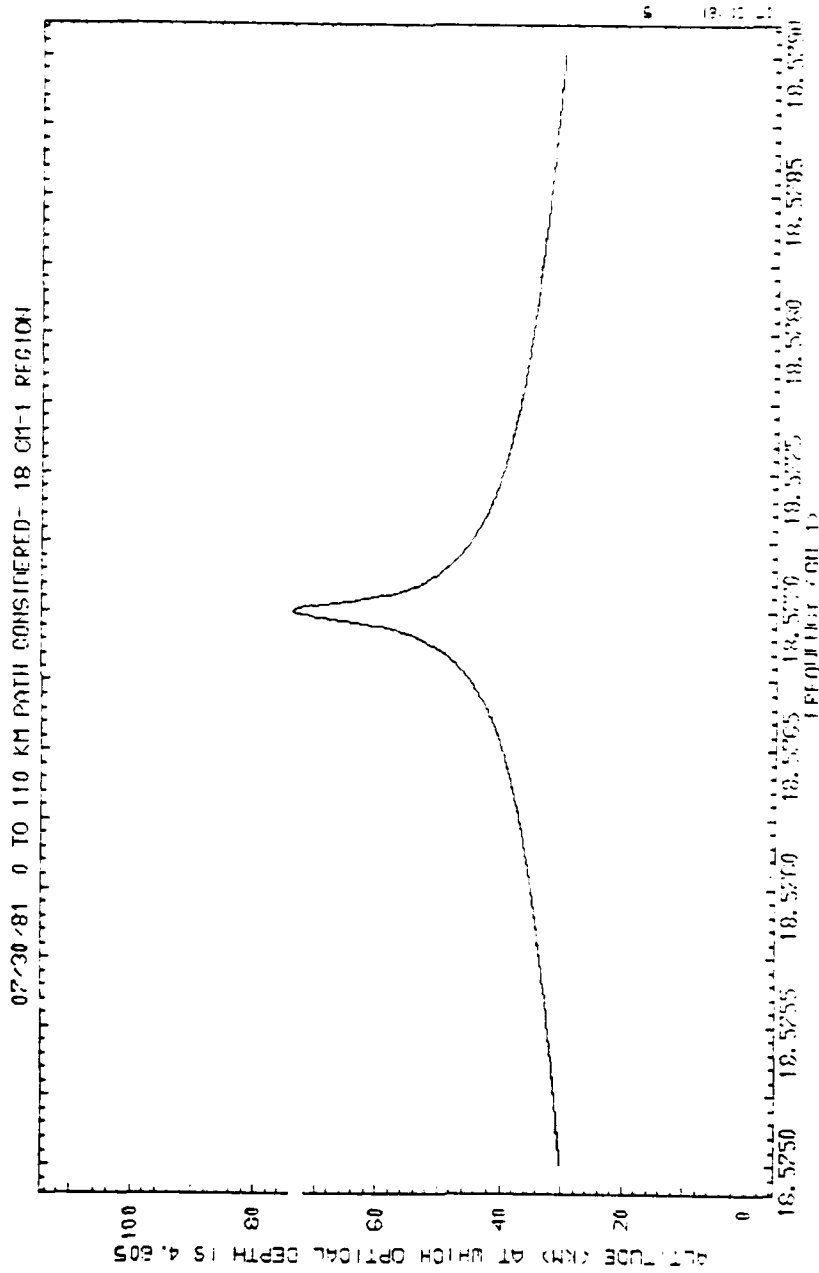
OPTICAL DEPTH = 2.303



OPTICAL PATH CONSIDERED WAS FROM 0.0000 TO 110.0000 KM

Fig. 17. Altitude vs. Frequency at Fixed Optical Depth (= 2.303)

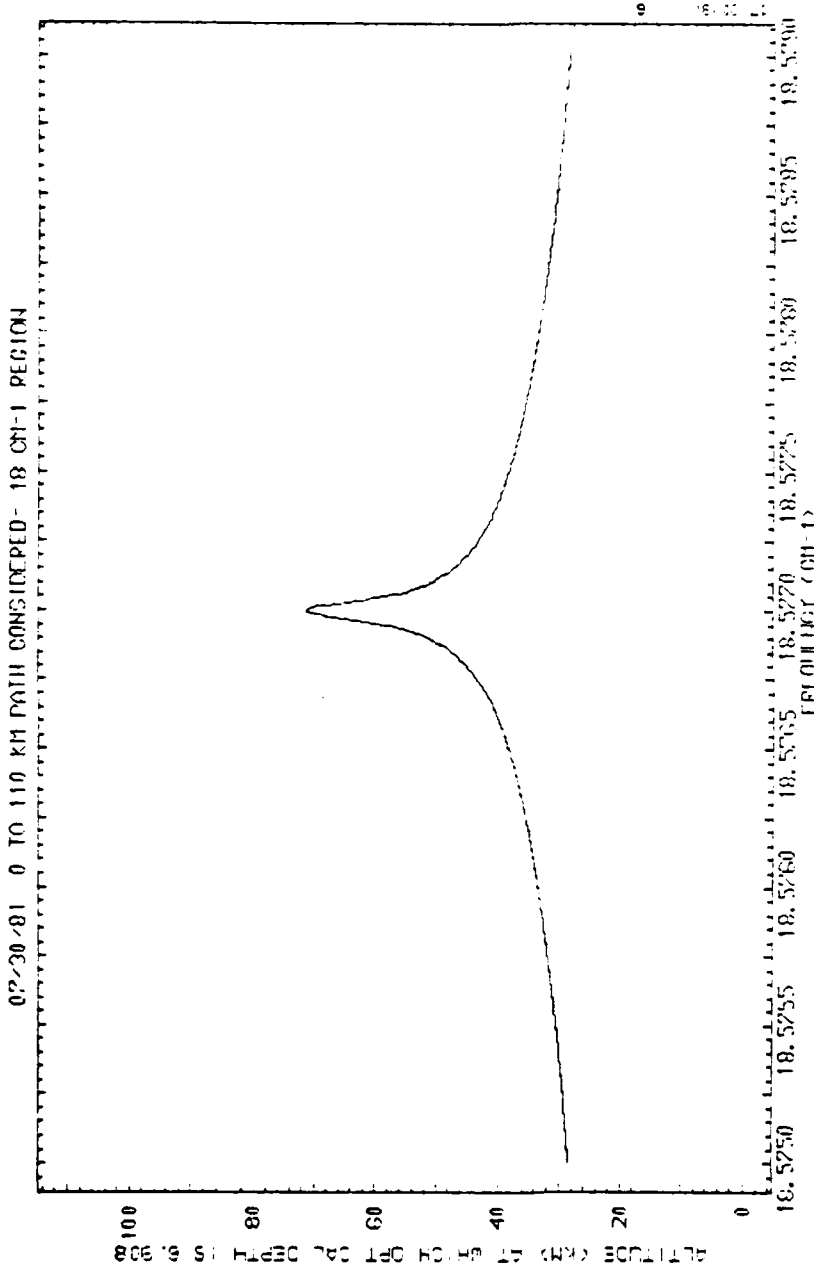
OPTICAL DEPTH = 4.605



OPTICAL PATH CONSIDERED WAS FROM 0.0000 TO 110.0000 KM

Fig. 18. Altitude vs. Frequency at Fixed Optical Depth (= 4.605)

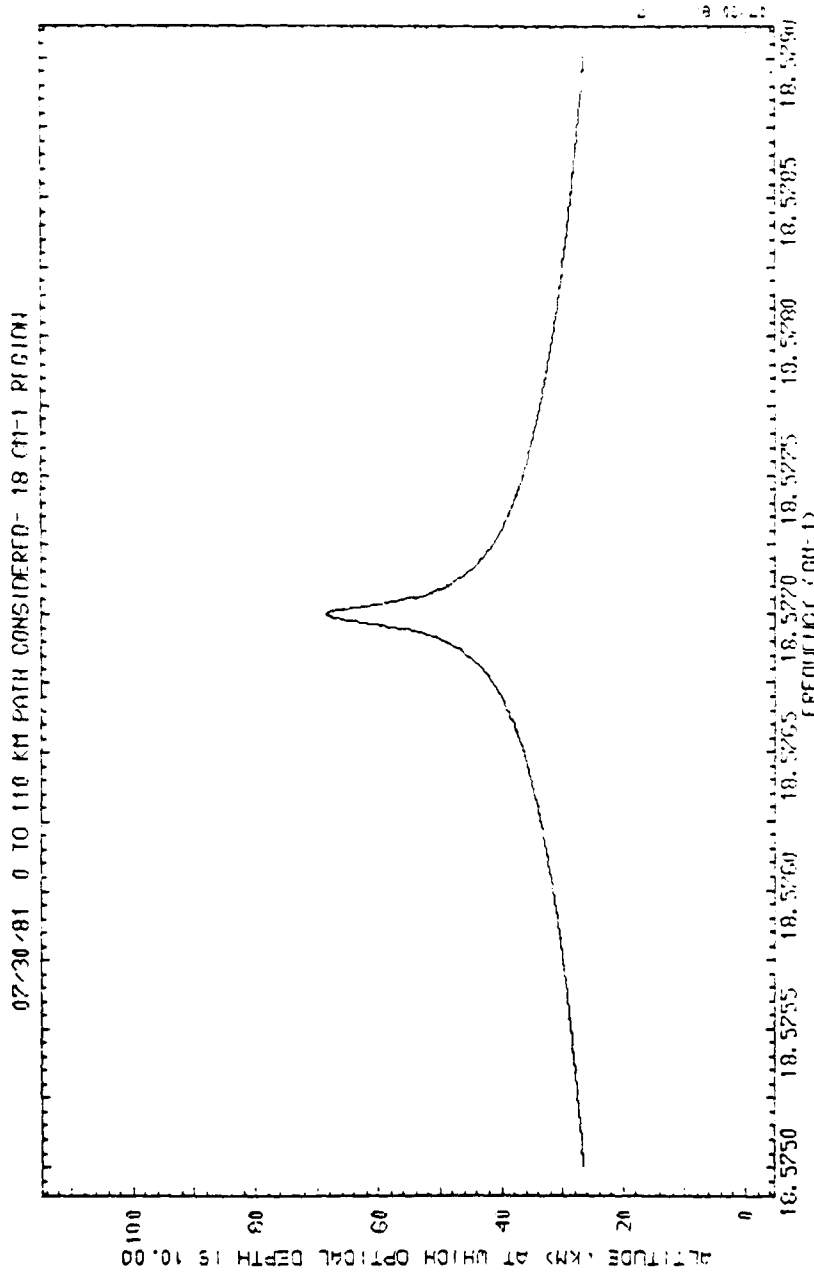
OPTICAL DEPTH = 6.908



OPTICAL PATH CONSIDERED WAS FROM 0.0000 TO 110.0000 KM

Fig. 19. Altitude vs. Frequency at Fixed Optical Depth (= 6.908)

OPTICAL DEPTH = 10.0



OPTICAL PATH CONSIDERED WAS FROM 0.0000 TO 110.0000 KM

Fig. 20. Altitude vs. Frequency at Fixed Optical Depth (= 10.0)

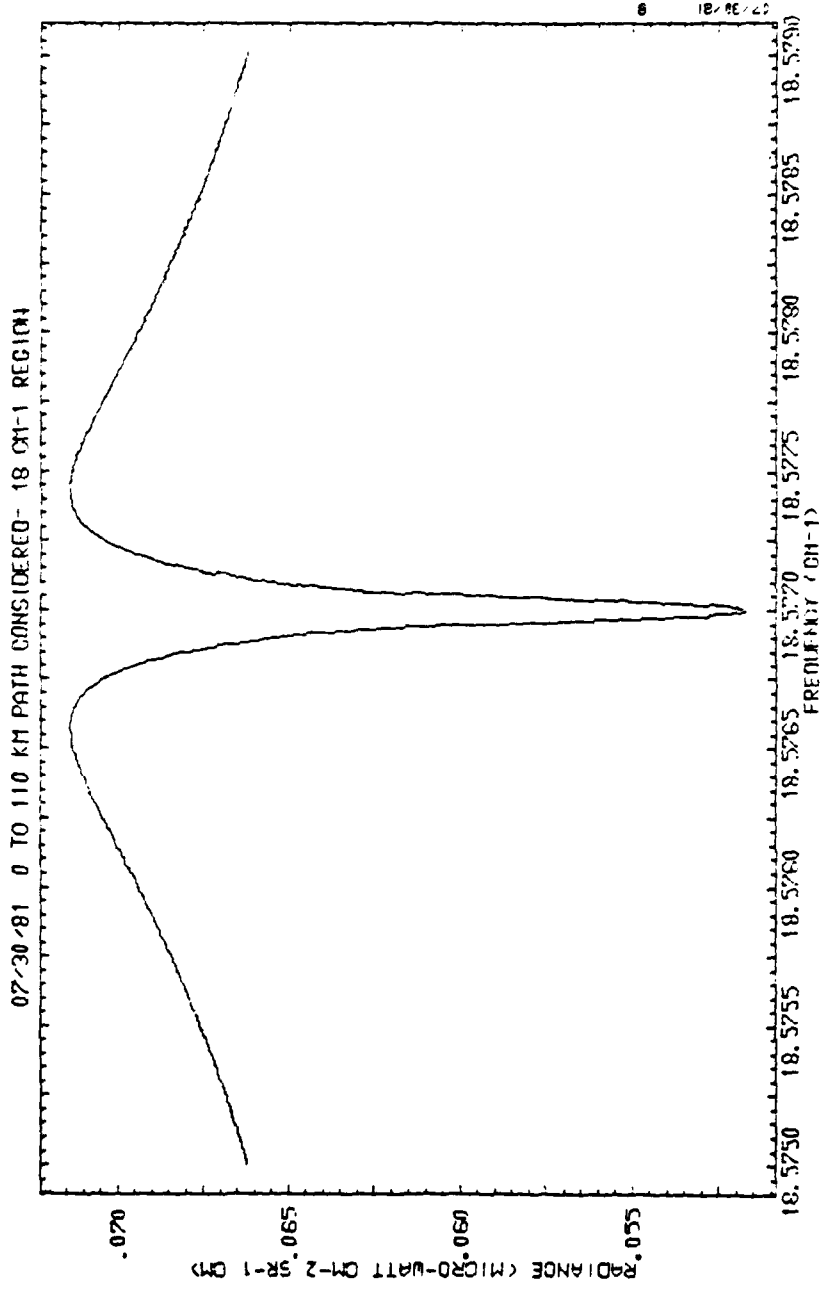


Fig. 21. Integrated Path Spectral Radiance

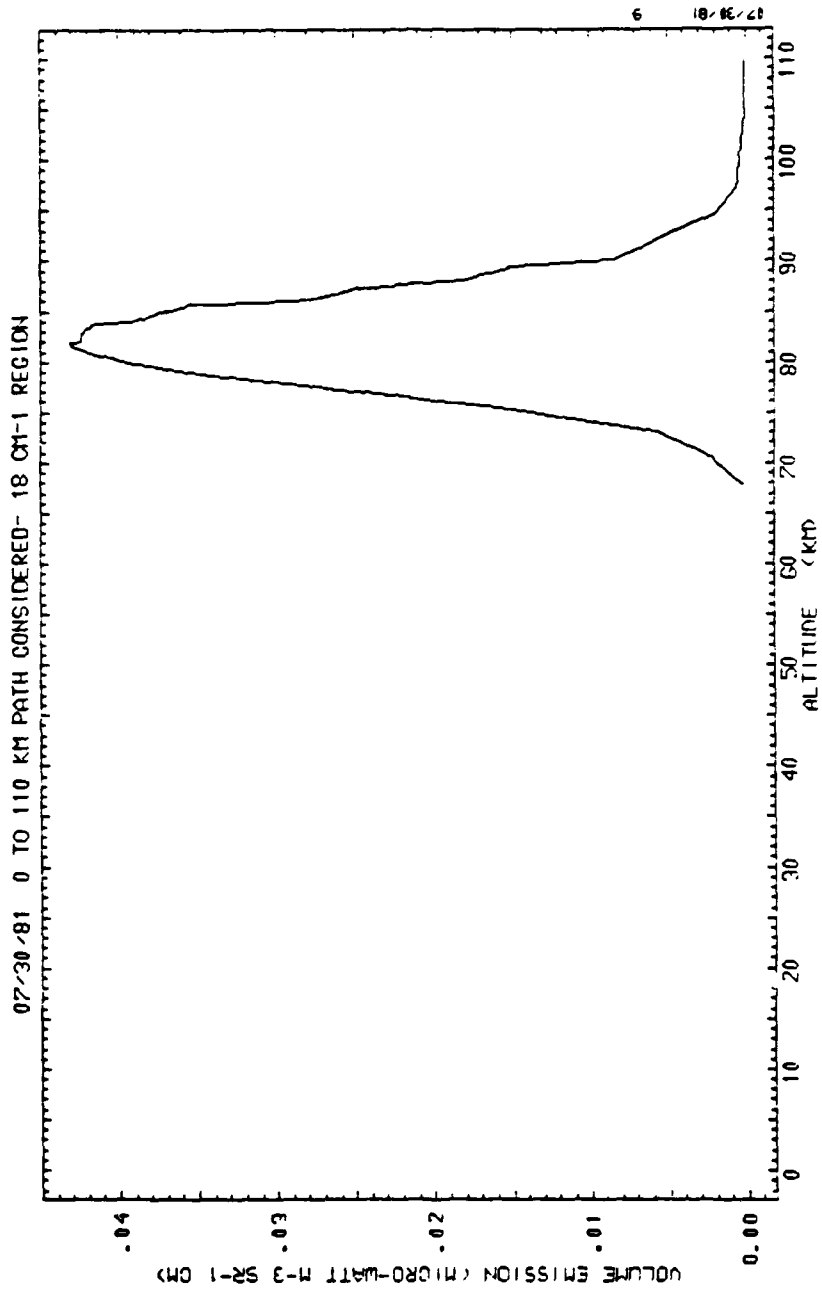


Fig. 22. Radiance Contribution Profile for 18.57699 cm^{-1}

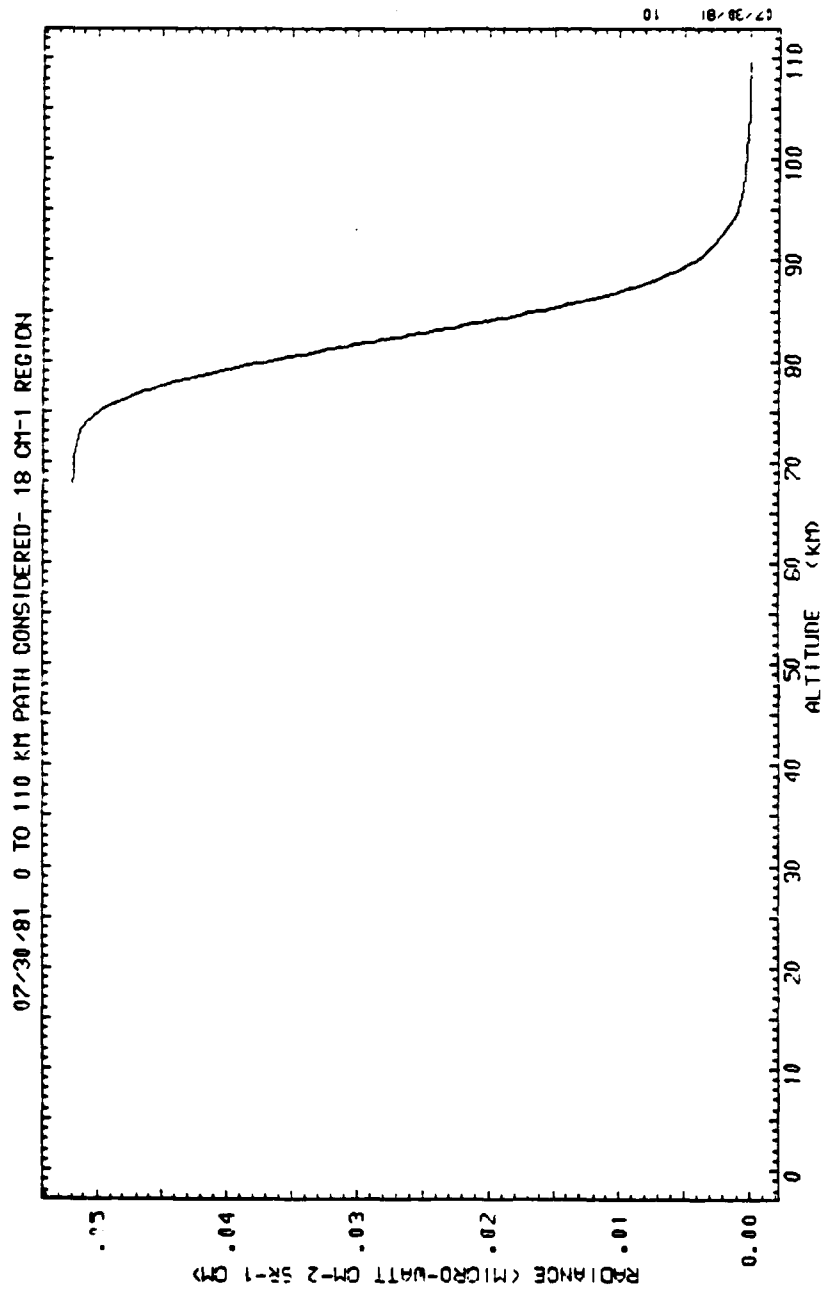


Fig. 23. Cumulative Radiance Profile for 18.57699 cm⁻¹

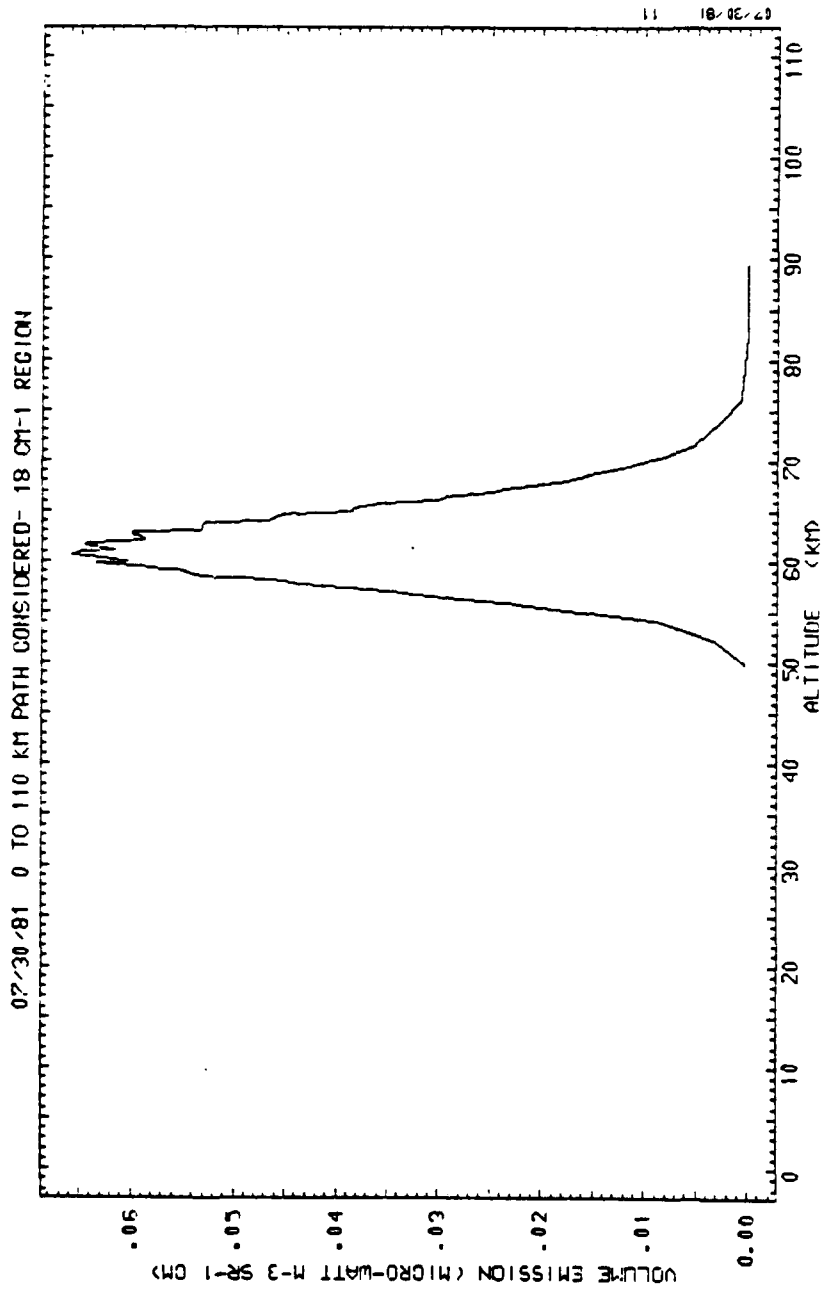


Fig. 24. Radiance Contribution Profile for 18.57709 cm⁻¹

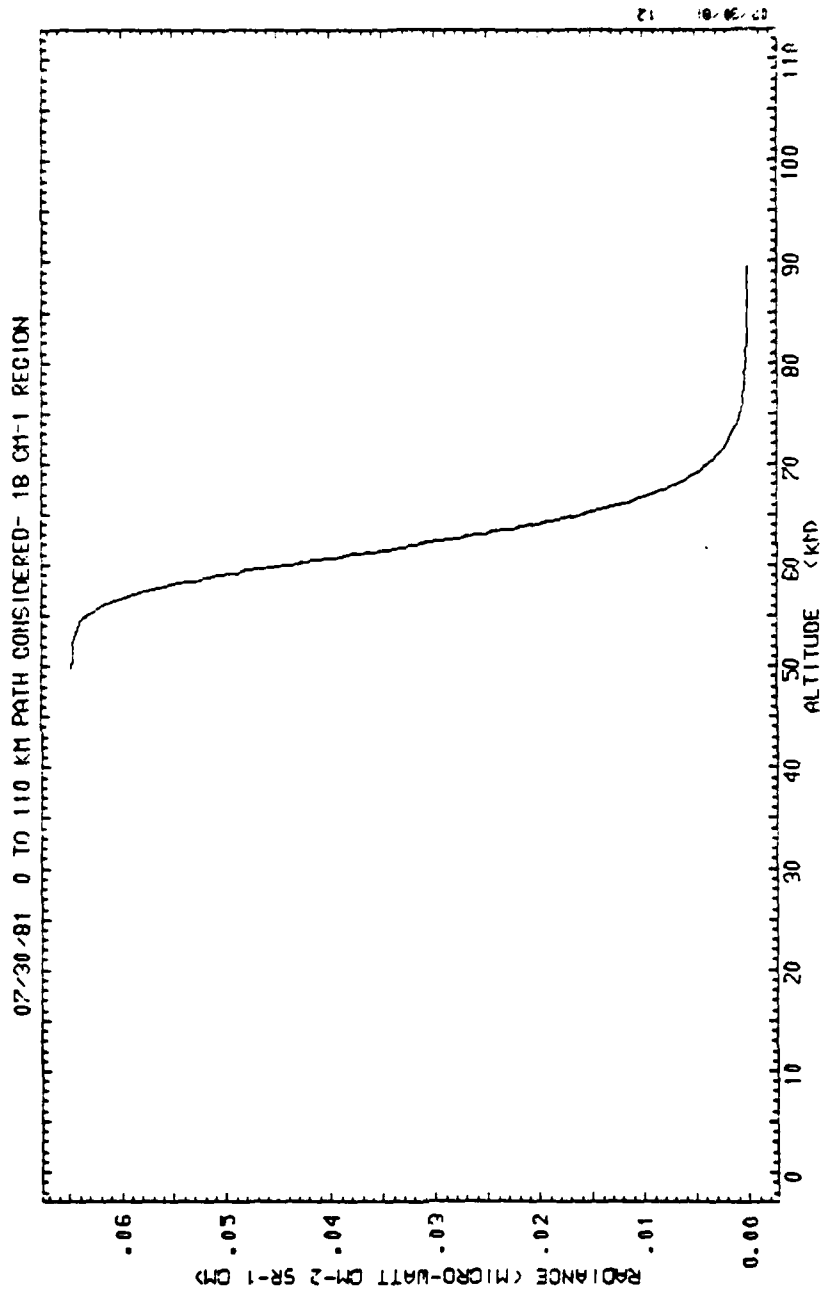


Fig. 25. Cumulative Radiance Profile for
18.57709 cm⁻¹

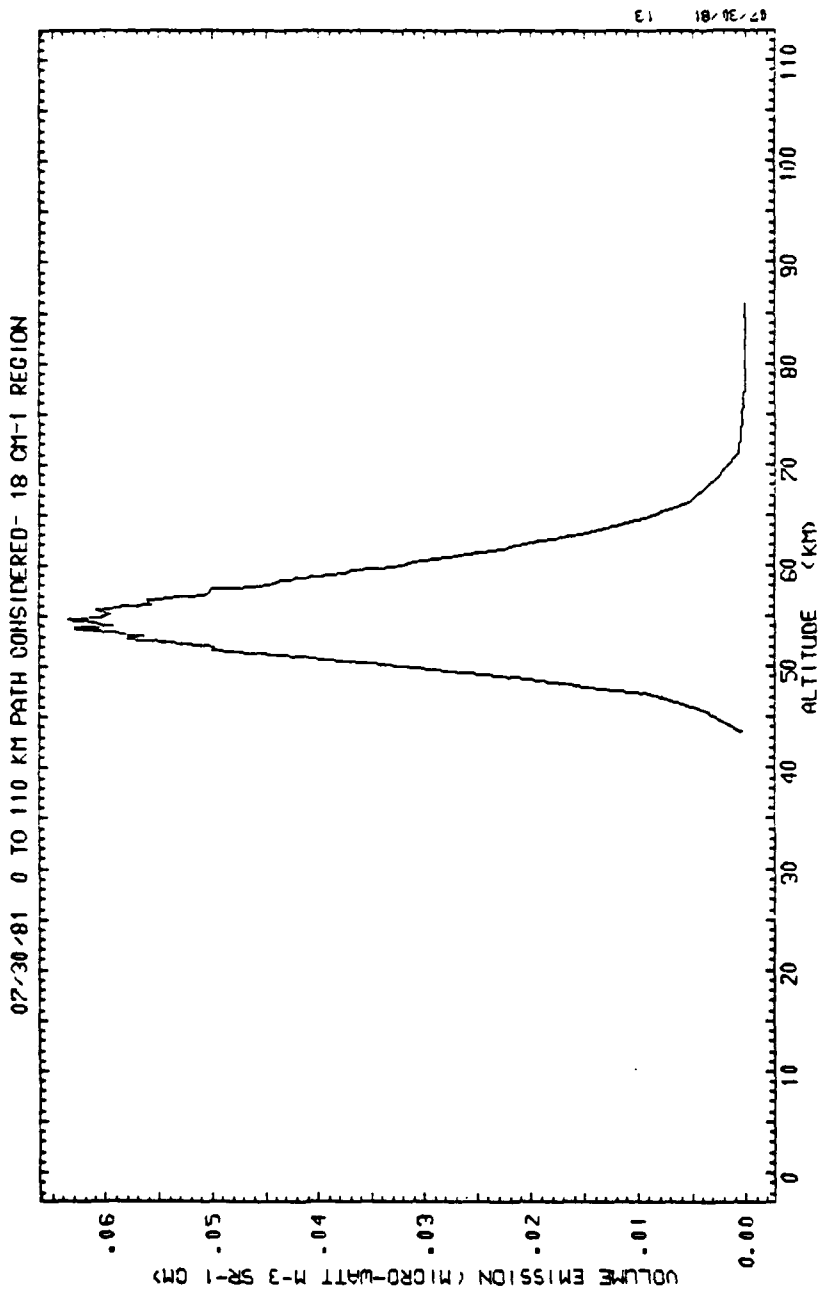


Fig. 26. Radiance Contribution Profile for
18.57719 cm

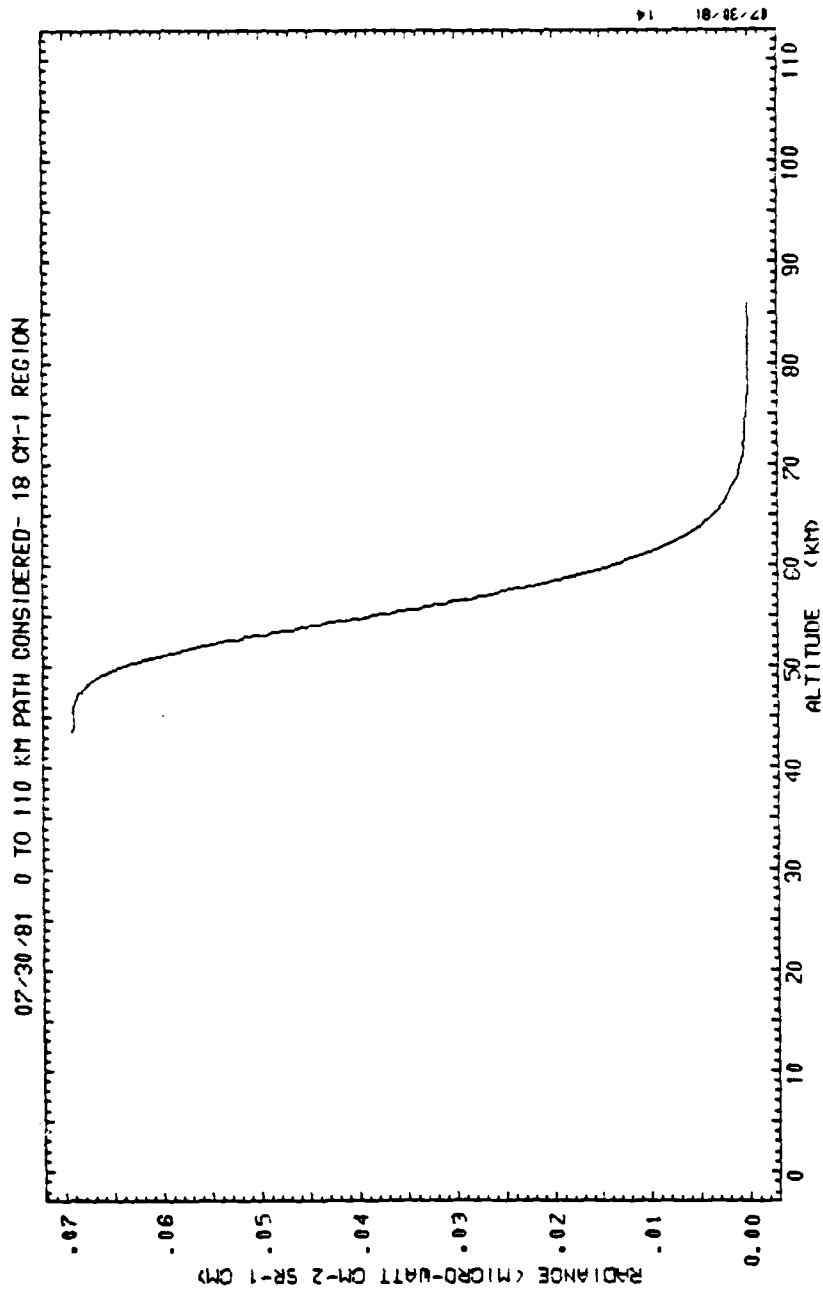


Fig. 27. Cumulative Radiance Profile for 18.57719 cm⁻¹

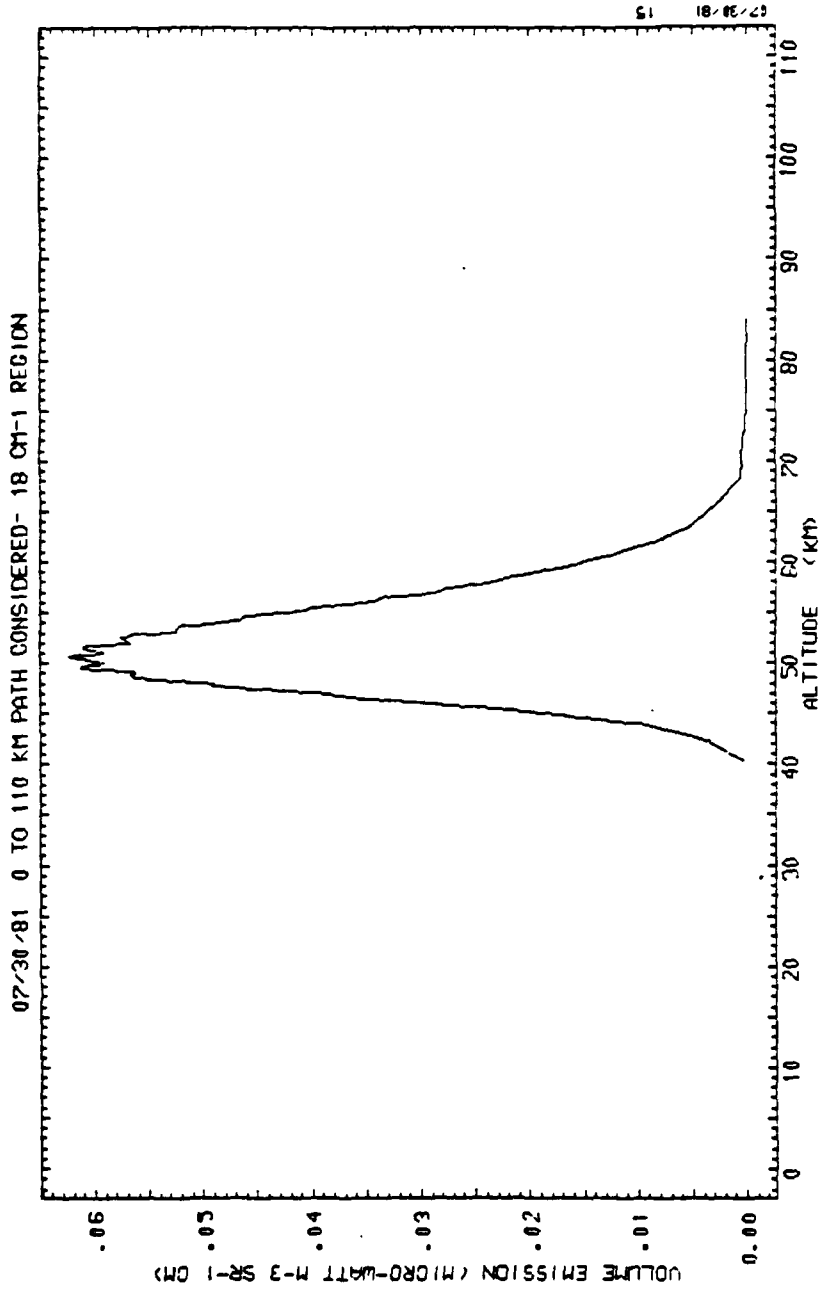


Fig. 28. Radiance Contribution Profile for 18.57729 cm⁻¹

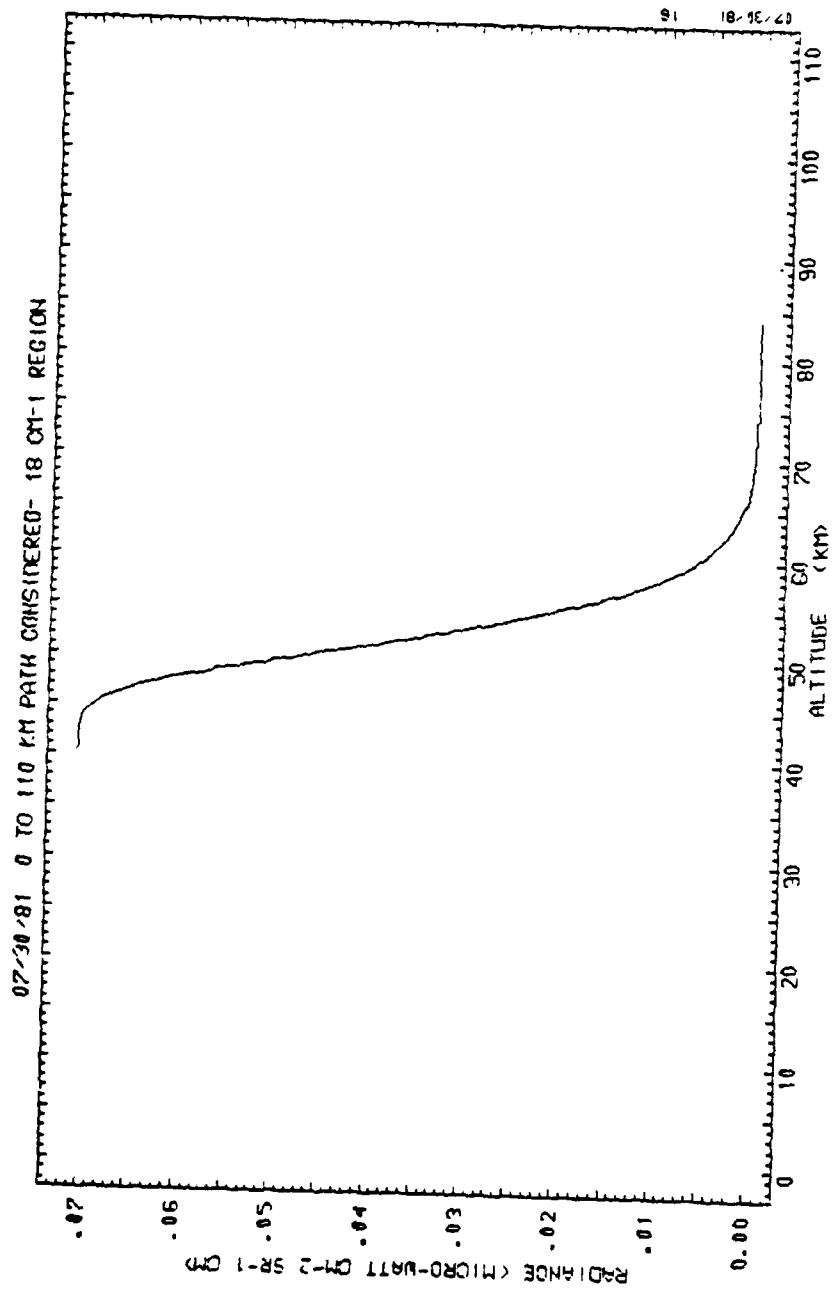


Fig. 29. Cumulative Radiance Profile for 18.57729 cm⁻¹

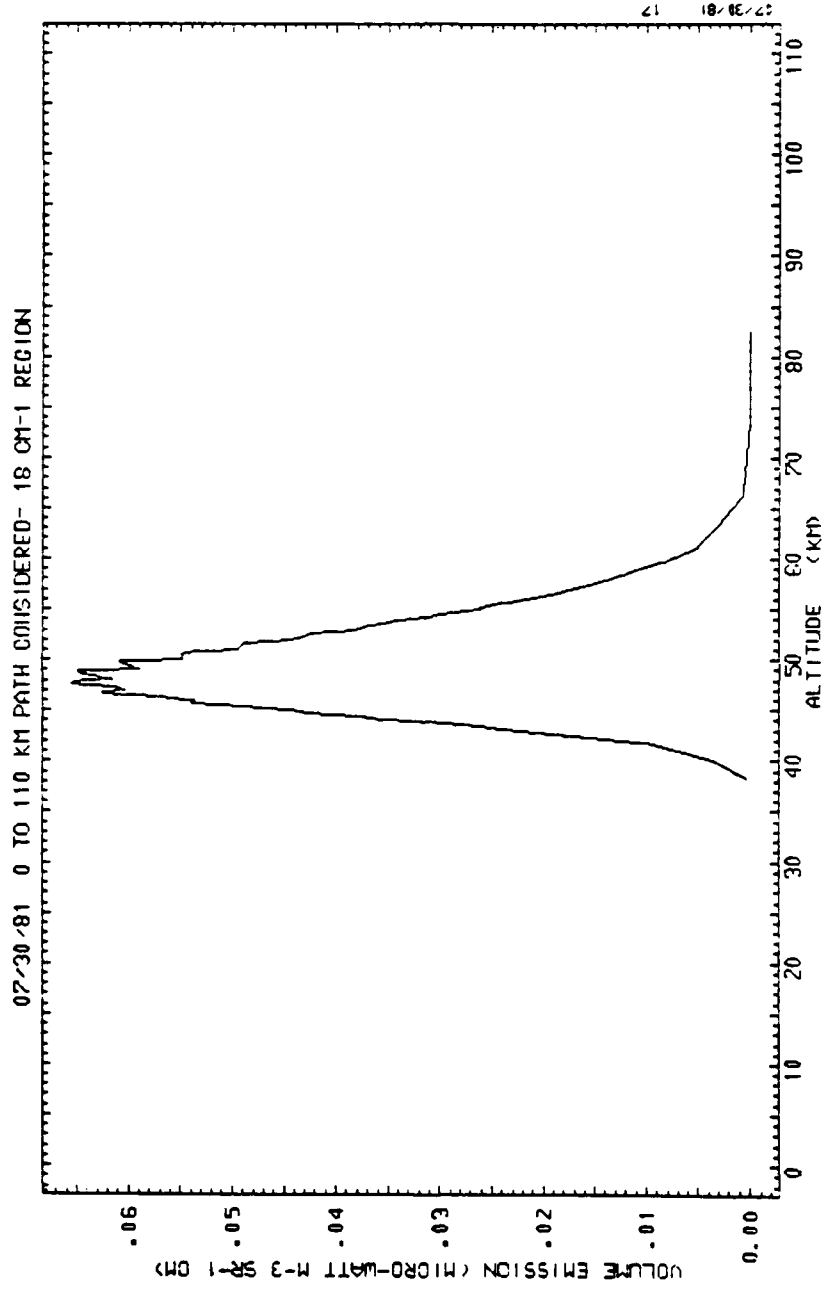


Fig. 30. Radiance Contribution Profile for 18.57739 cm⁻¹

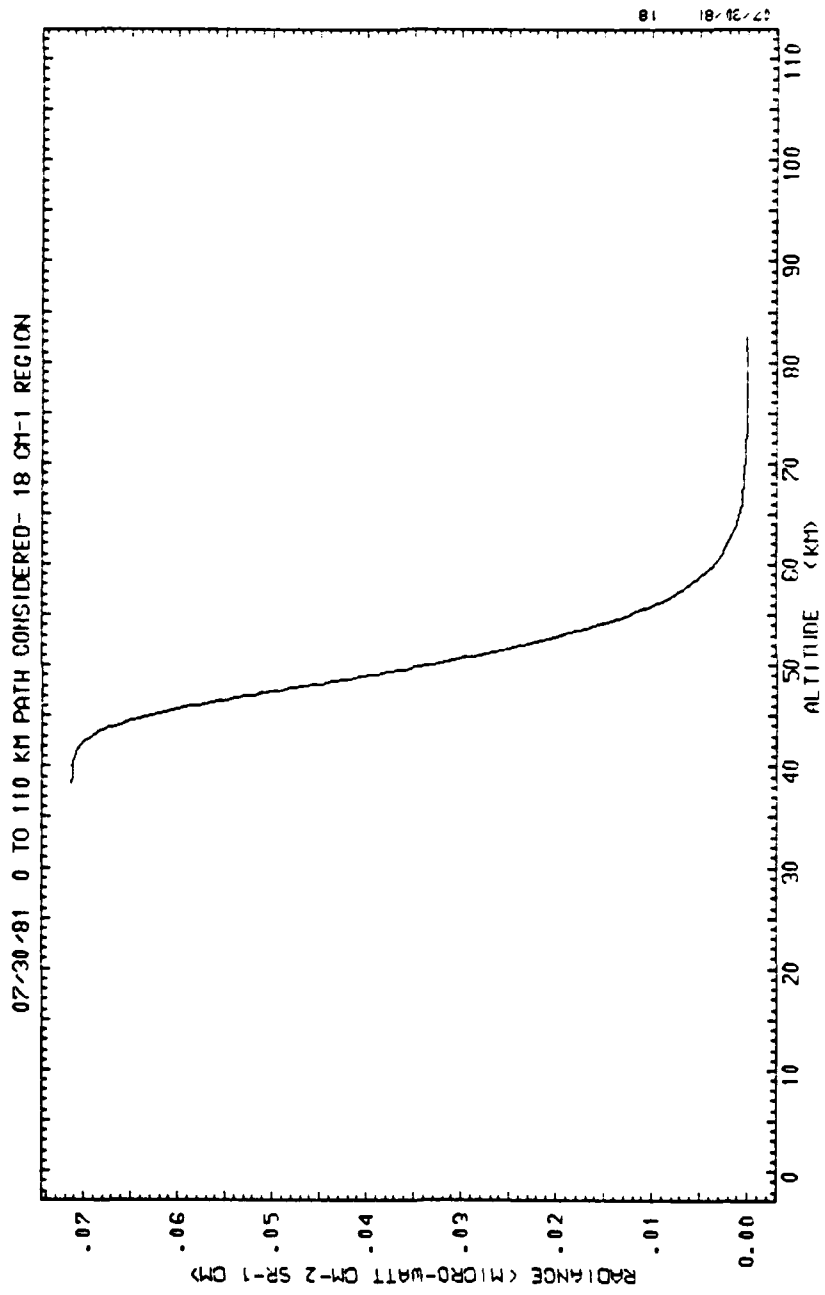


Fig. 31. Cumulative Radiance Profile for 18.57739 cm⁻¹

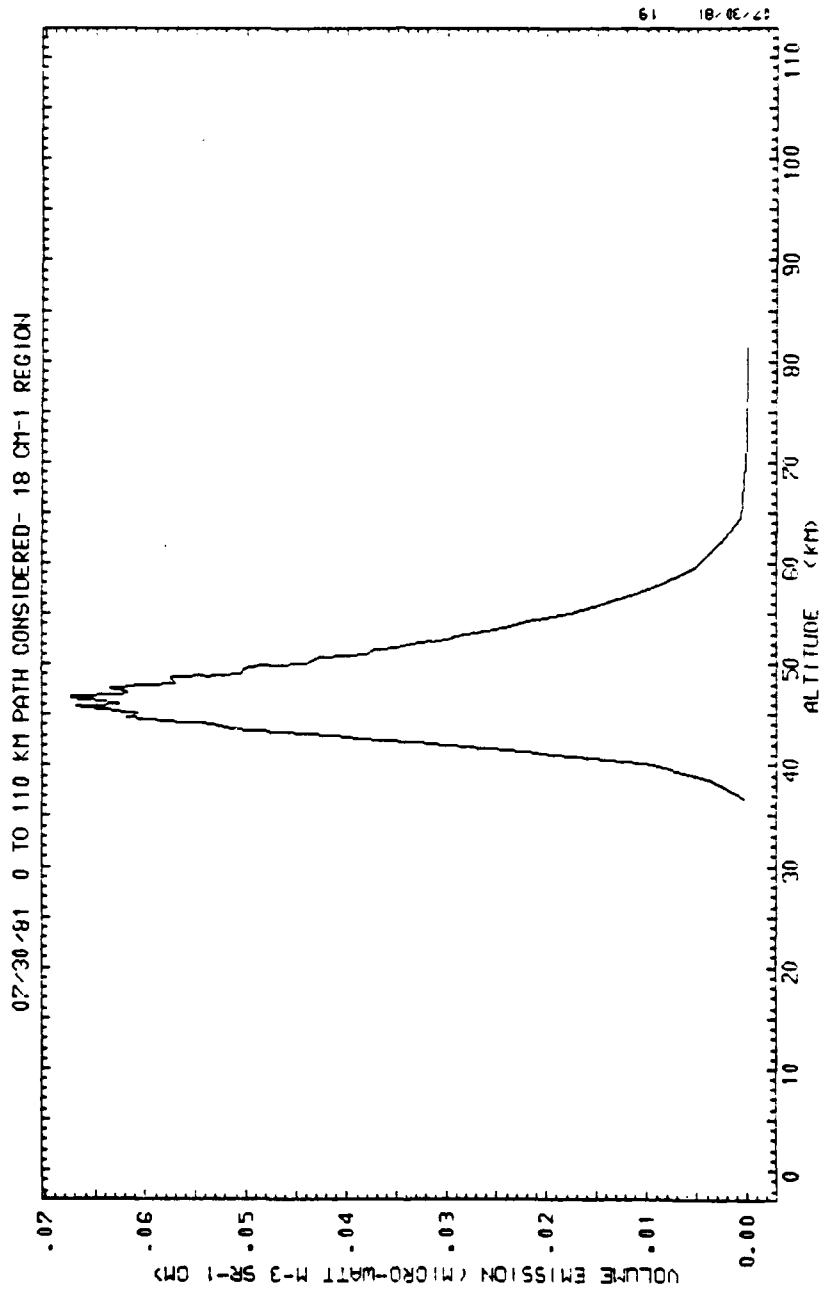


Fig. 32. Radiance Contribution Profile for
18.57749 cm⁻¹

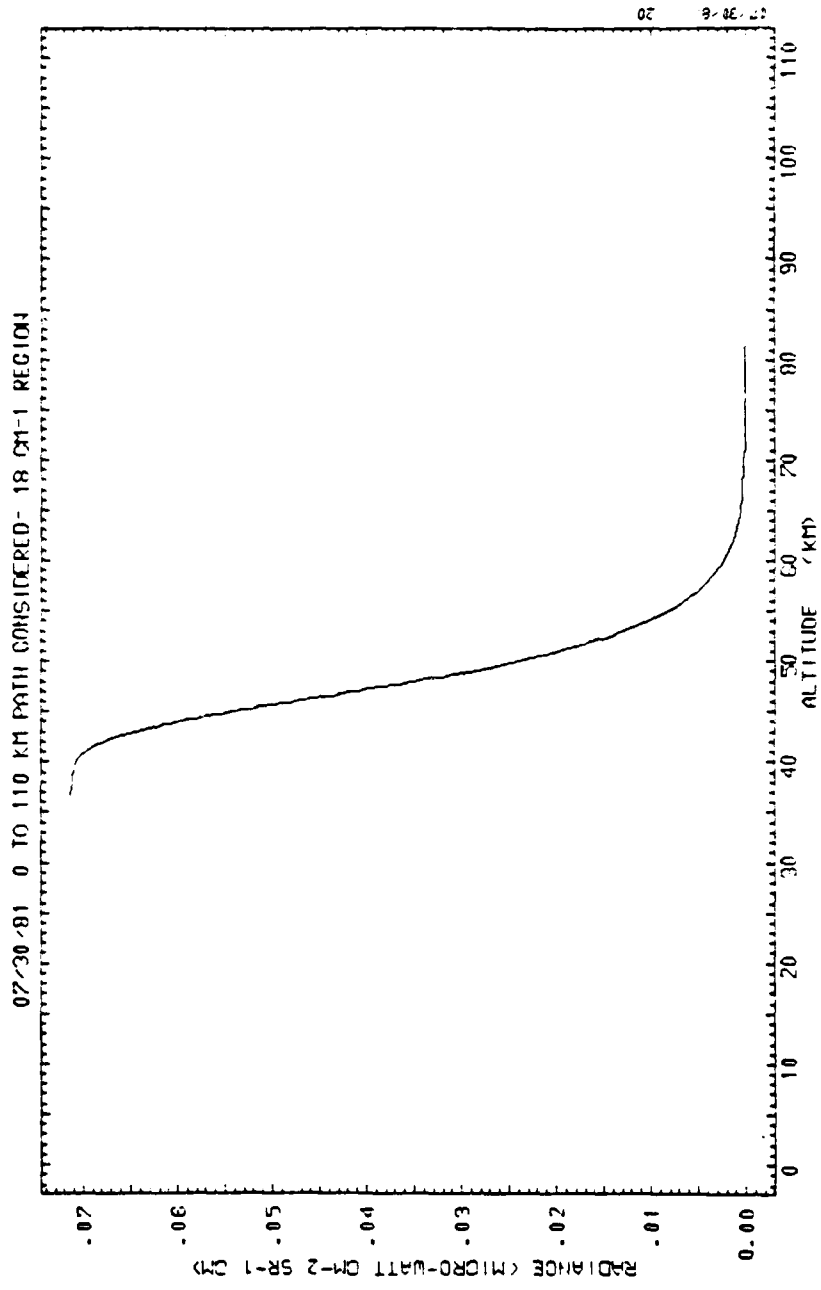


Fig. 33. Cumulative Radiance Profile for 18.57749 cm⁻¹

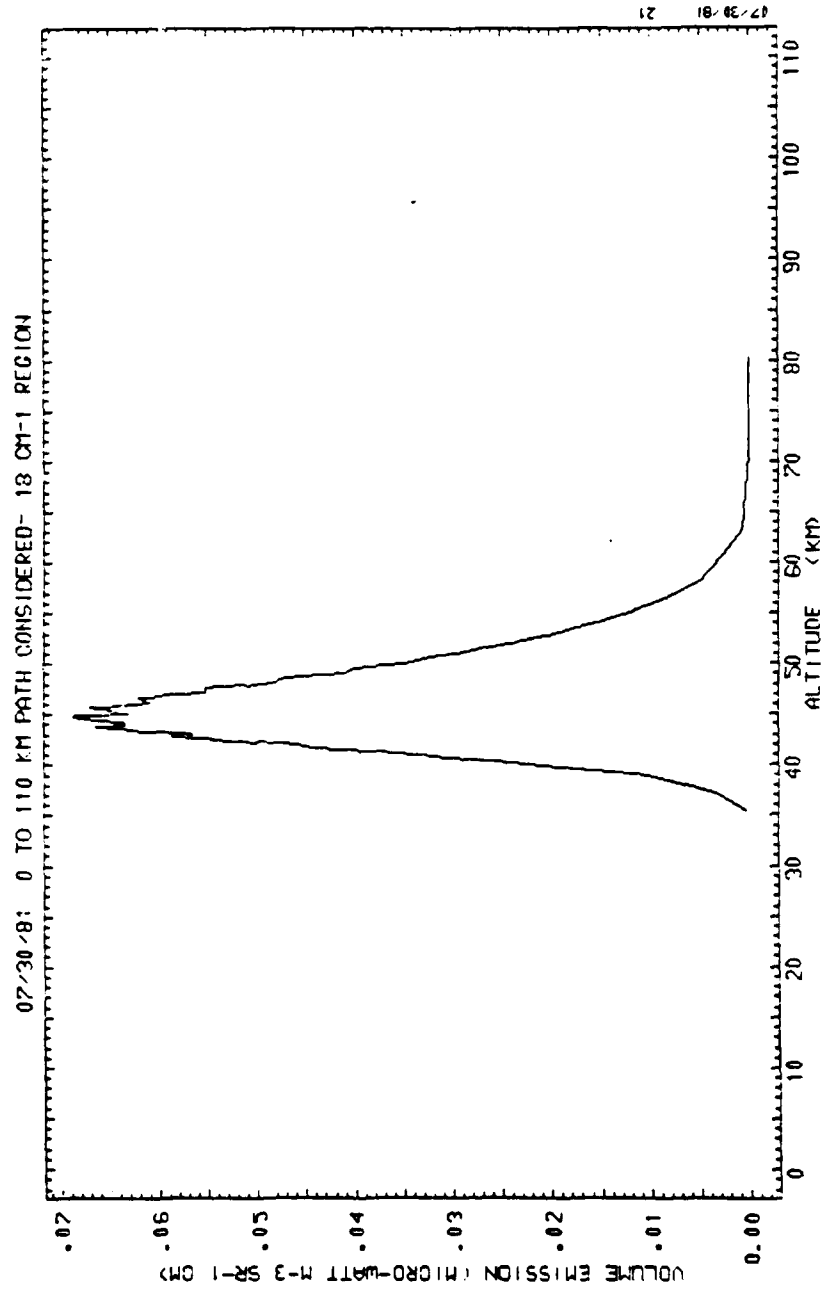


Fig. 34. Radiance Contribution Profile for
18.57759 cm⁻¹

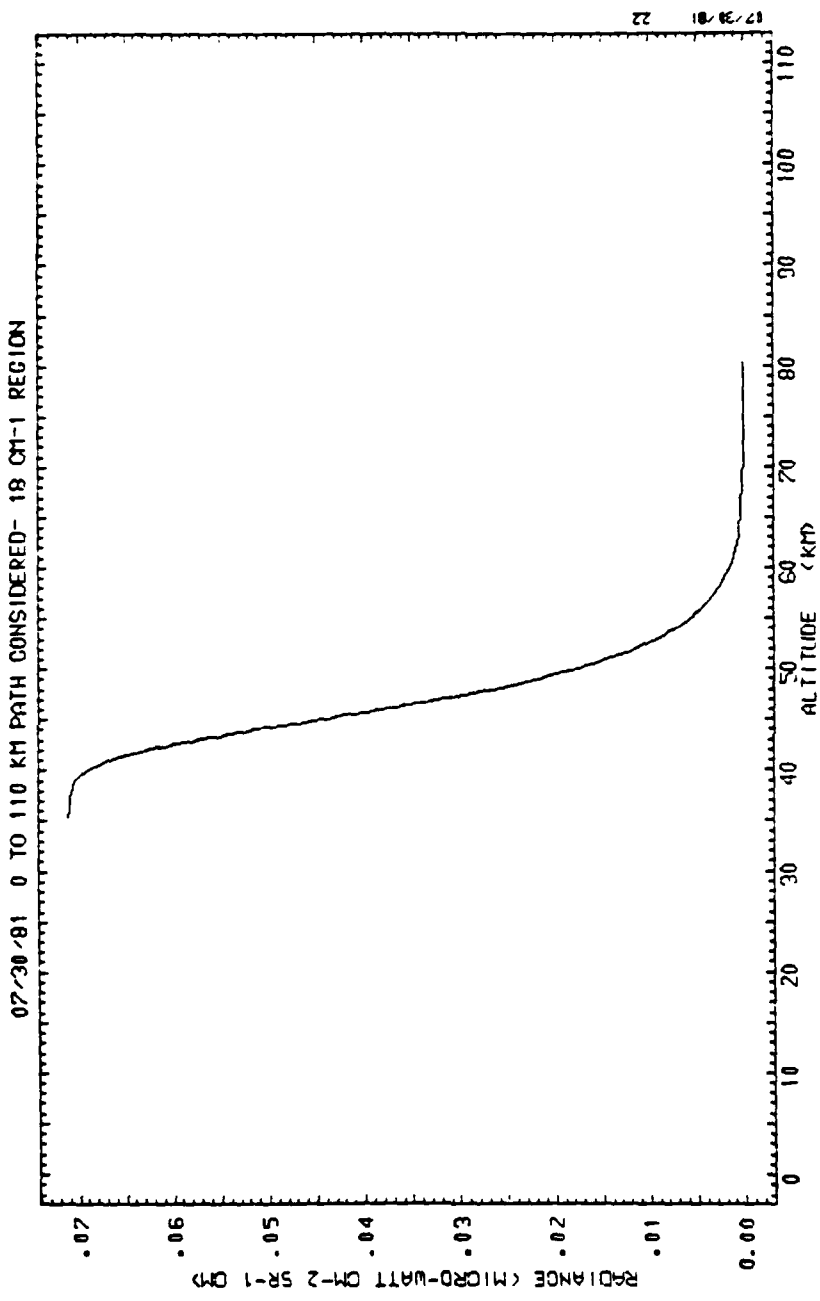


Fig. 35. Cumulative Radiance Profile for 18.57759 cm⁻¹

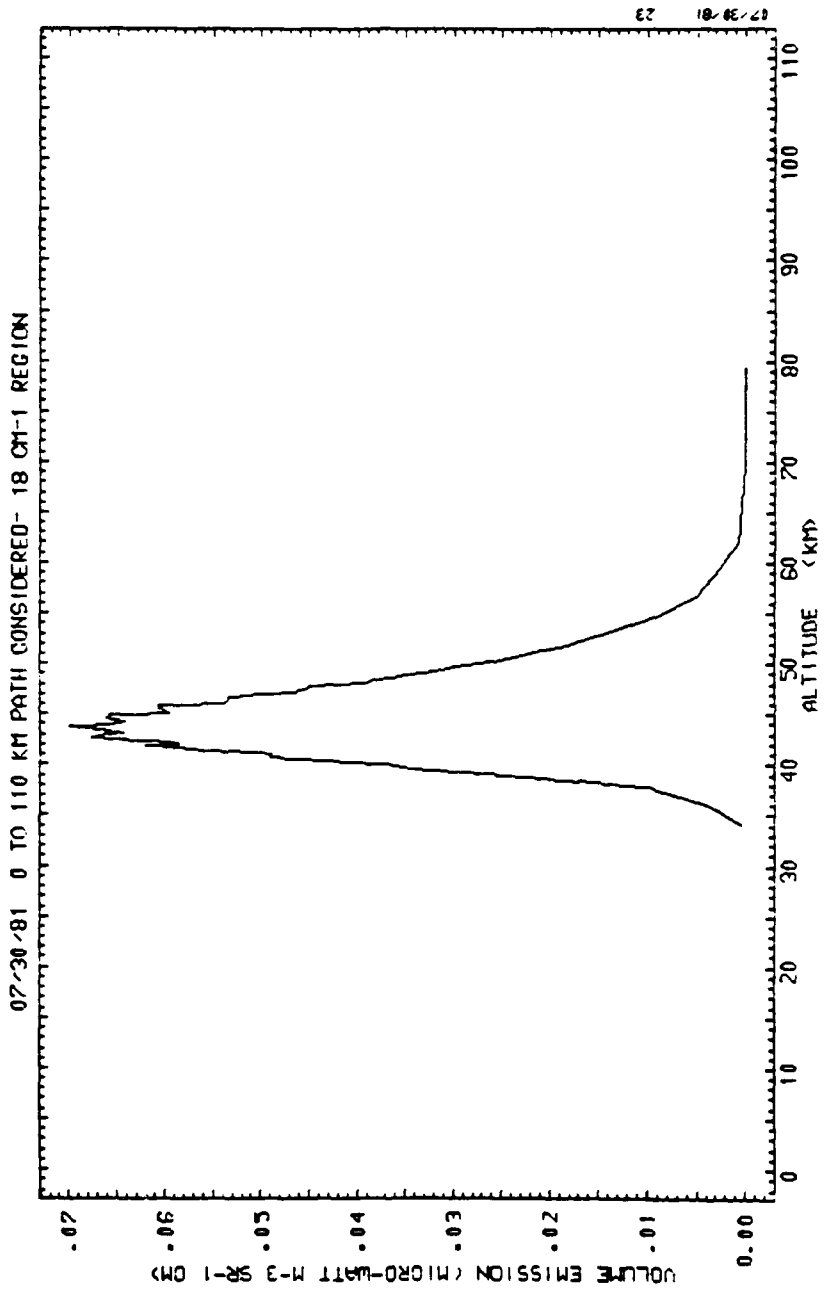


Fig. 36. Radiance Contribution Profile for 18.57770 cm⁻¹

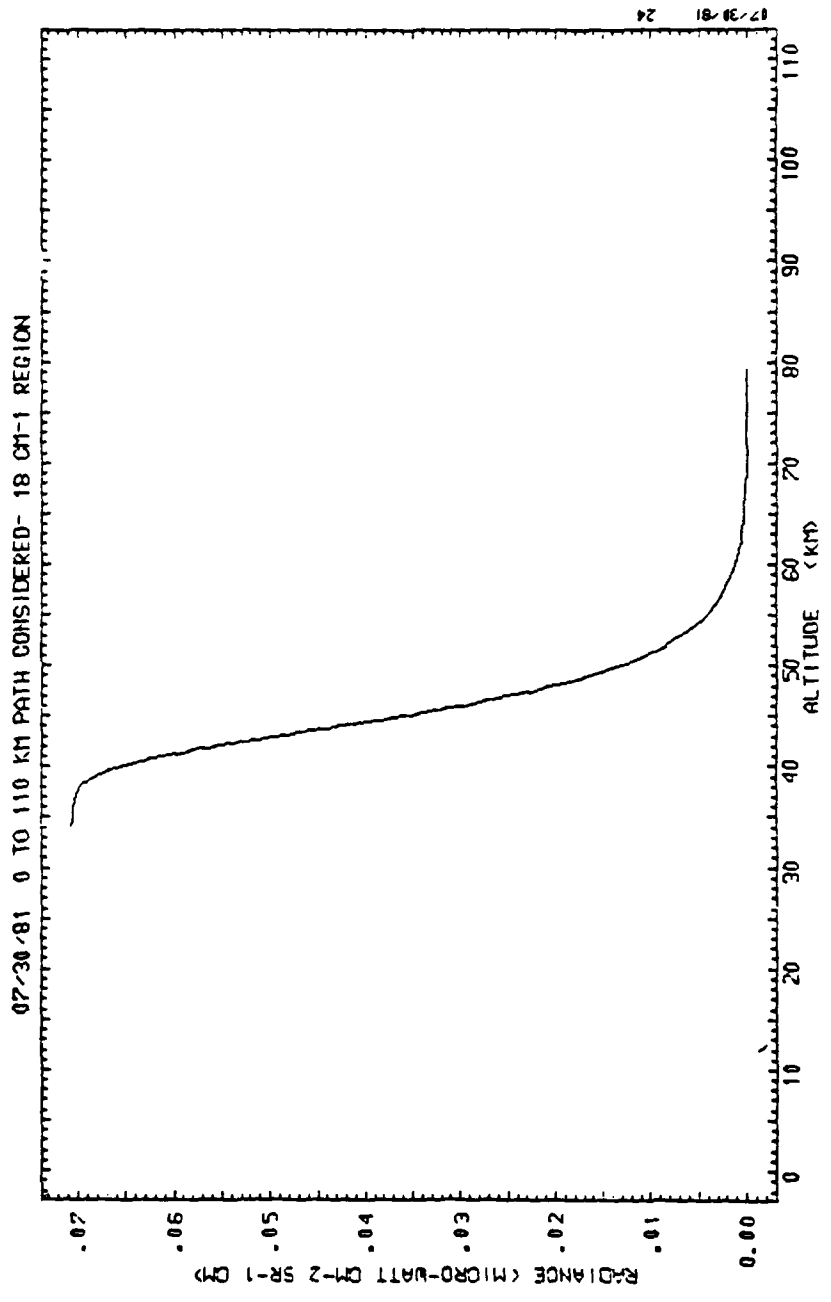


Fig. 37. Cumulative Radiance Profile for 18.57770 cm⁻¹

the relative cumulative spectral radiance at each of several fixed values of frequency. Similar plots are available from the authors for the remaining cases listed in Table 2.

The finer structure visible in the even-numbered plots of Figs. 22 through 36 is not real; it is a consequence of the artificial stratification of atmospheric properties into homogeneous layers of finite thickness as necessary to do the computer calculation. The structure is gradually removed as the number of layers in the calculation is increased, but the computation time increases proportionately.

Figures 22 through 36 substantiate the claim made in Sec. III that we are concerned with the altitude range from 35 to 100 km. Similar results for cases 1, 2, 4, and 5 (Table 2) give about the same altitude range.

The altitude at which the peak apparent spectral radiance occurs as a function of signal frequency, or Doppler shift, can be determined from these plots. The distribution for cases 1 through 5 is shown in Fig. 38, and is seen to be fairly independent of the atmospheric model for temperature or humidity. The thickness of the emitting layer can also be determined from these plots. The altitude range between the 10% and 90% points on the cumulative radiance plots is defined here as thickness. The distribution of thickness with signal frequency is shown in Fig. 39. Here there is some dependence on the water vapor model, but very little dependence on temperature distribution.

The spectral radiance of the background within the expected Doppler range is shown in Fig. 40 for cases 1 through 5. Also shown is the spectrum calculated by Litvak et al. (Ref. 1), the conditions of which correspond nominally to those of case 4. It can be seen that large differences in background spectra can be expected to occur with differing atmospheric temperature profiles. This confirms the suggestion that observations taken at places on the earth's disc that are separated by large distances (> 1000 km) may have significantly different background radiation. Clearly, in an operational system, algorithms with the purpose of identifying a missile plume from spectral absorption measurements with the earth's disc in the field of view will have to contend with a large variety of possible background spectra.

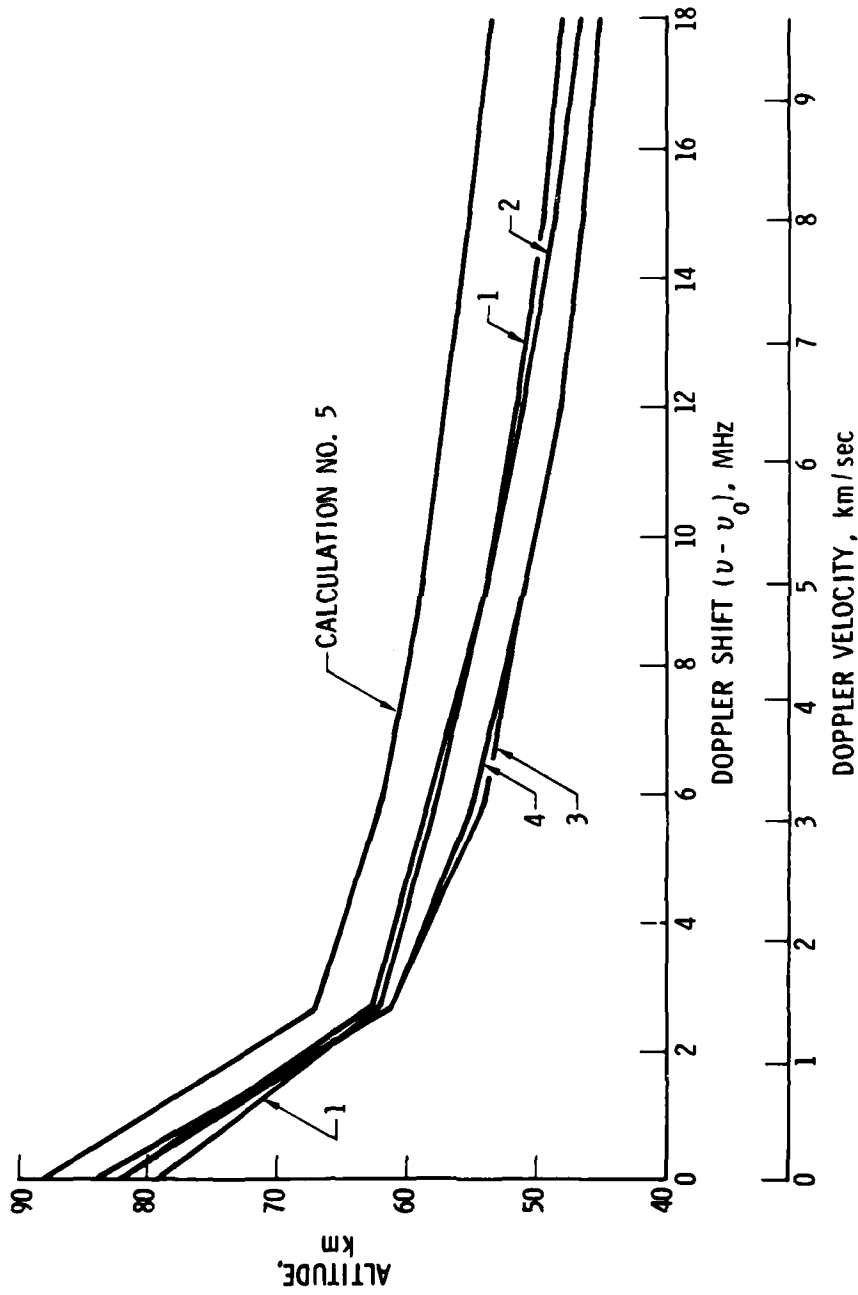


Fig. 38. Distribution of the Altitude of Peak Apparent Radiance with Doppler Shift from Line Center

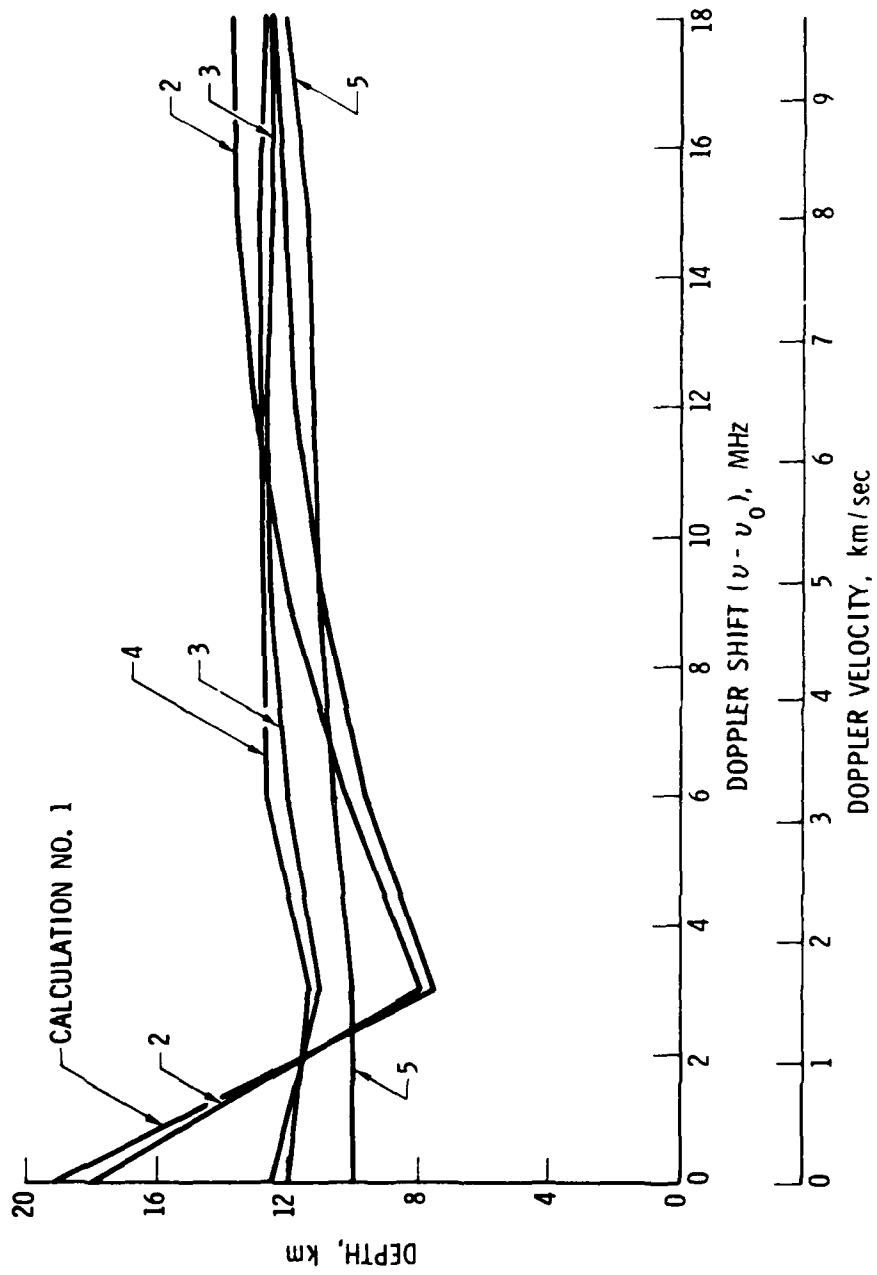


Fig. 39. Distribution of the Depth of the Emitting Layer with Doppler Shift from Line Center

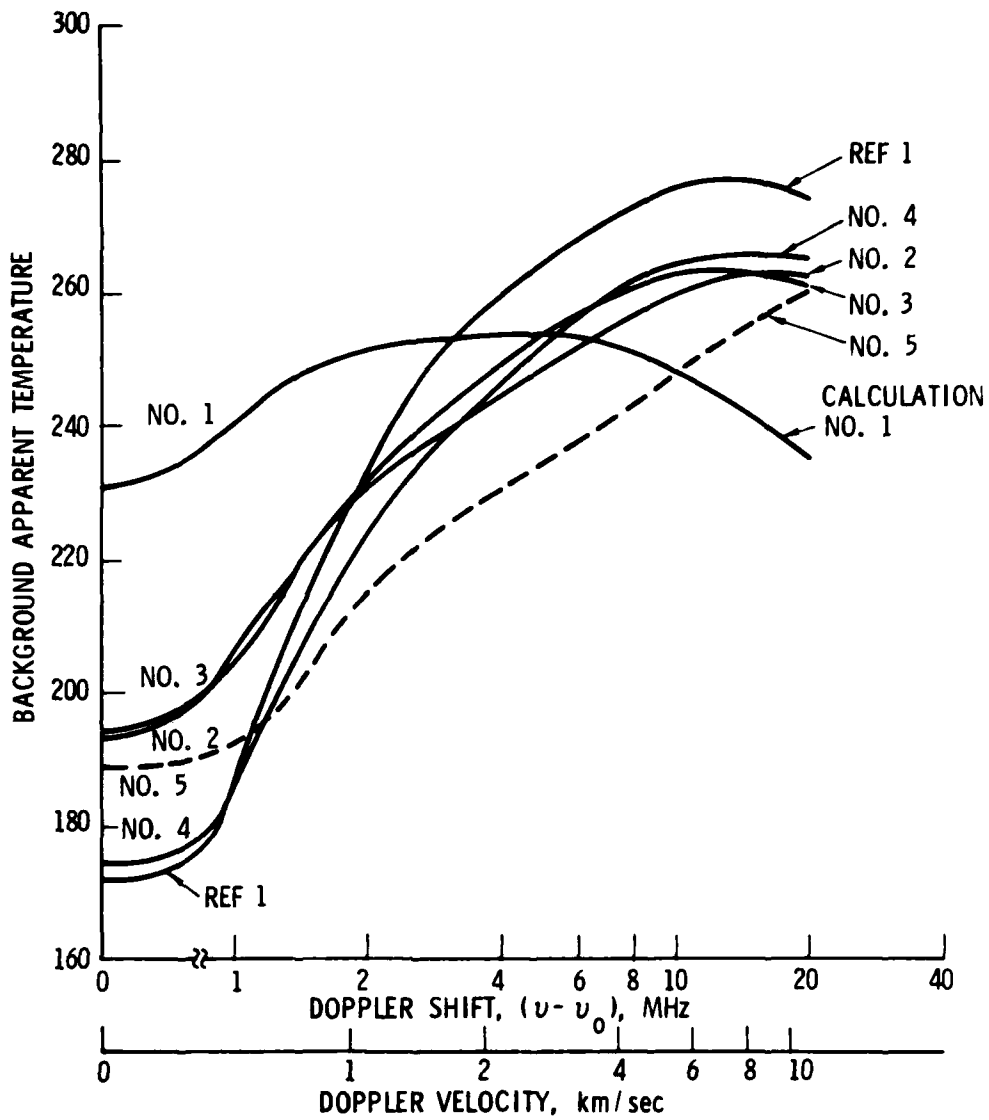


Fig. 40. Background Spectra for Various Model Atmospheres

Case 5 (Table 2) is identical with case 3, except that the line of sight is exactly tangential to the earth's surface instead of being vertical. It is seen in Figs. 38 through 40 that the effect of this different viewing geometry is slight, and it would appear that the background characteristics are only weakly dependent on the viewing geometry, provided that the line of sight intersects the earth's surface.

2. Limb Viewing

Two calculations (cases 6 and 7, Table 2) have been done in which the line of sight traverses at least some of the atmosphere, but does not intersect the earth's surface. These are distinguished by tangent height, the distance of closest approach to the surface.

Figure 41 shows spectral radiance for these two cases and also includes case 5 for comparison. One sees that the spectral radiance generally is quite different for limb viewing than for disc viewing geometries. The weighting functions, volume emission as a function of both altitude and slant path, are shown in Figs. 42 to 56 for cases 6 and 7. Clearly, the background spectral radiance undergoes a gradual transition from the character of Fig. 40 to that of a 3°K deep-space background as the line of sight moves from viewing the earth's disc to viewing above the limb. From the information presented here, that transition appears to begin at a tangent height of about 50 km and is essentially complete at a tangent height of 110 km. In between these two values, a wide variety of spectral shapes and atmospheric radiance profiles can be expected.

From the weighting functions in Figs. 44 to 56, it is seen that radiation is collected over a long slant path approaching several hundred kilometers for some combinations of tangent height and signal frequency.

The computations discussed so far give a broad view of the background characteristics on a global scale. We turn attention next to the variability of the background signature on a smaller scale, say, less than 1000 km horizontal distance.

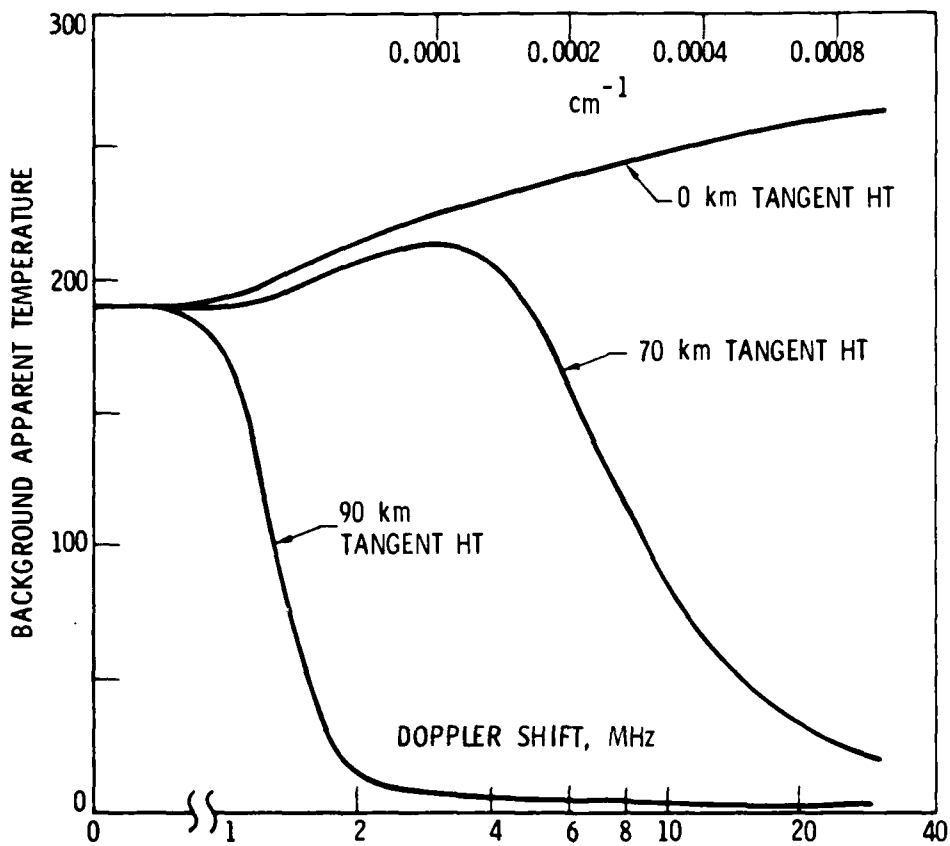


Fig. 41. Earth Limb Background Spectra

LIMB VIEWING

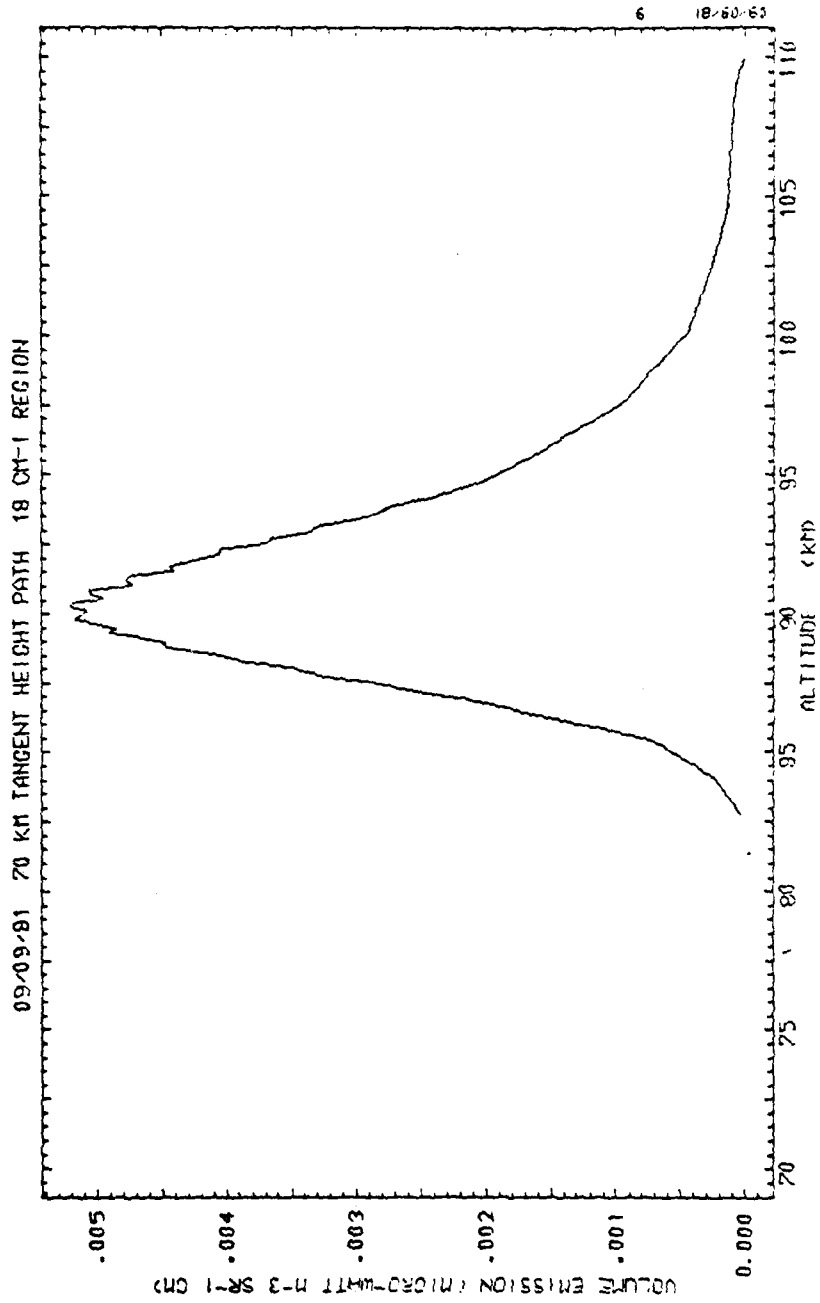


Fig. 42. Radiance Contribution Profile for 18.57699 cm^{-1}

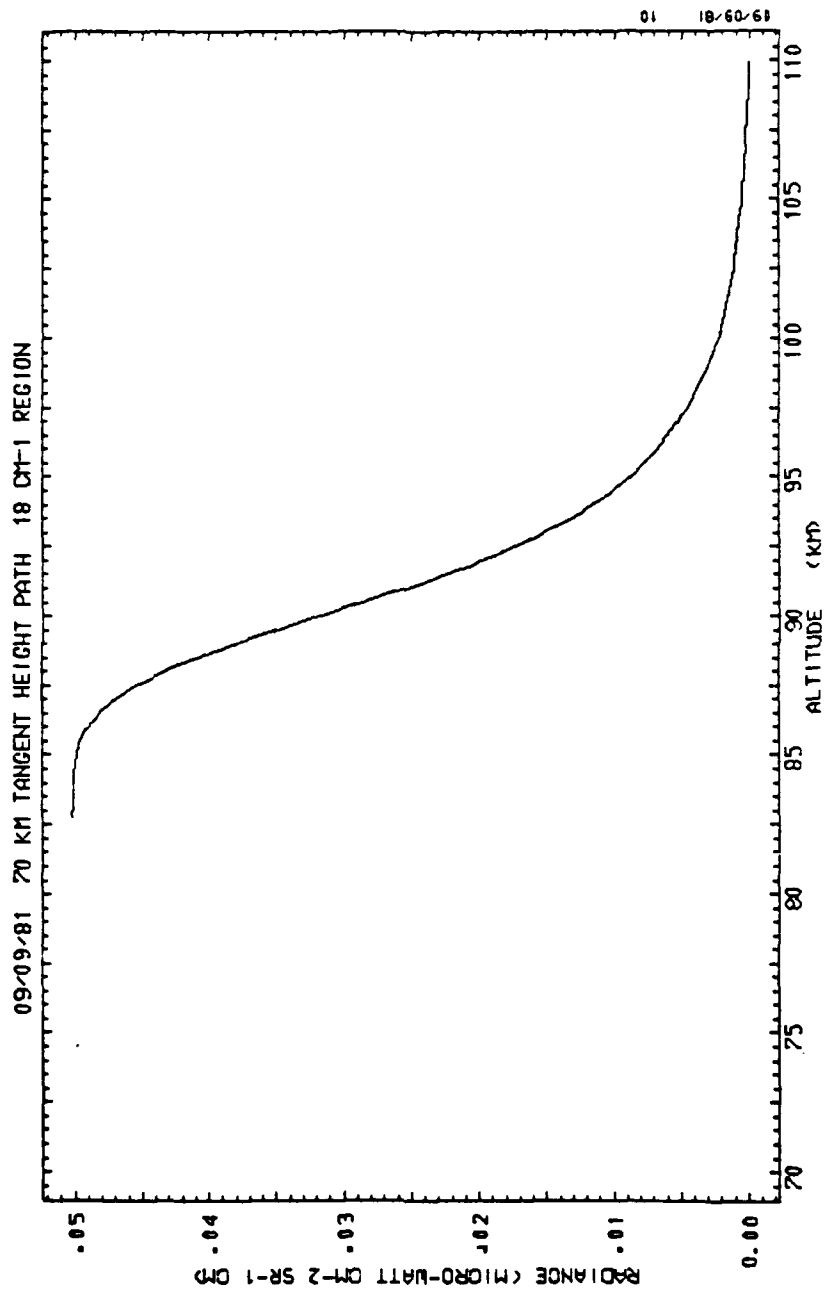


Fig. 43. Cumulative Radiance Profile for
18.57699 cm^{-1}

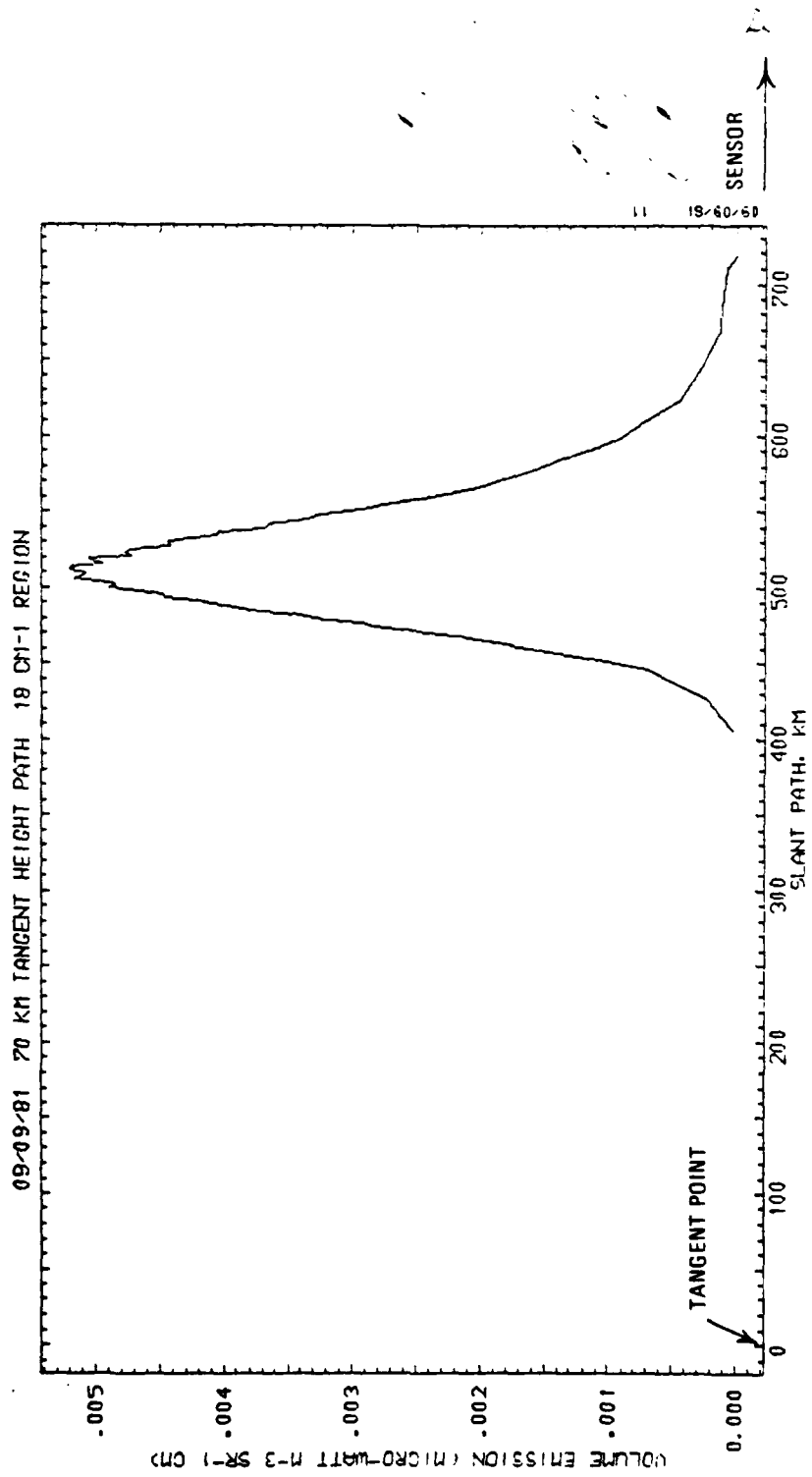


Fig. 44. Slant Path Radiance Profile for
18.57699 cm⁻¹

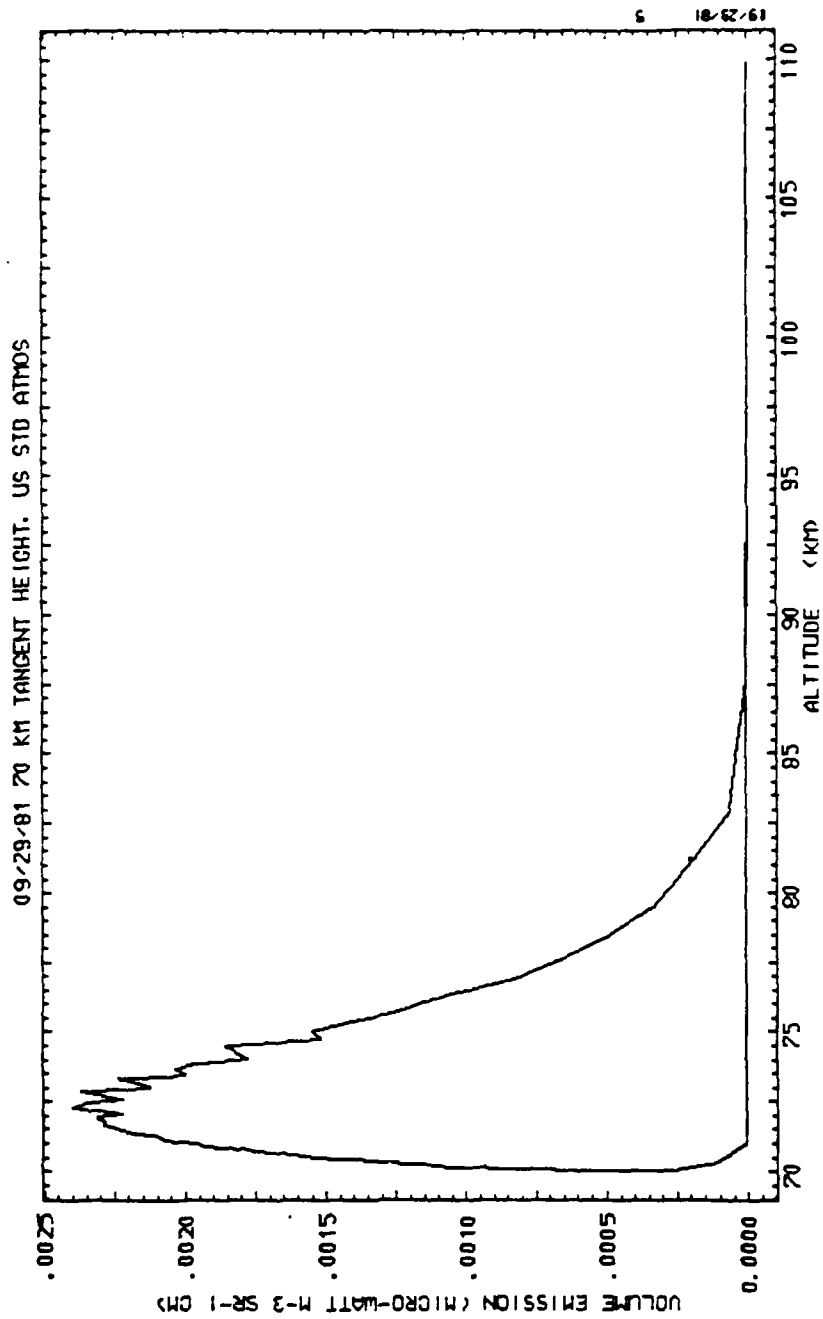


Fig. 45. Radiance Contribution Profile for 18.57710 cm^{-1}

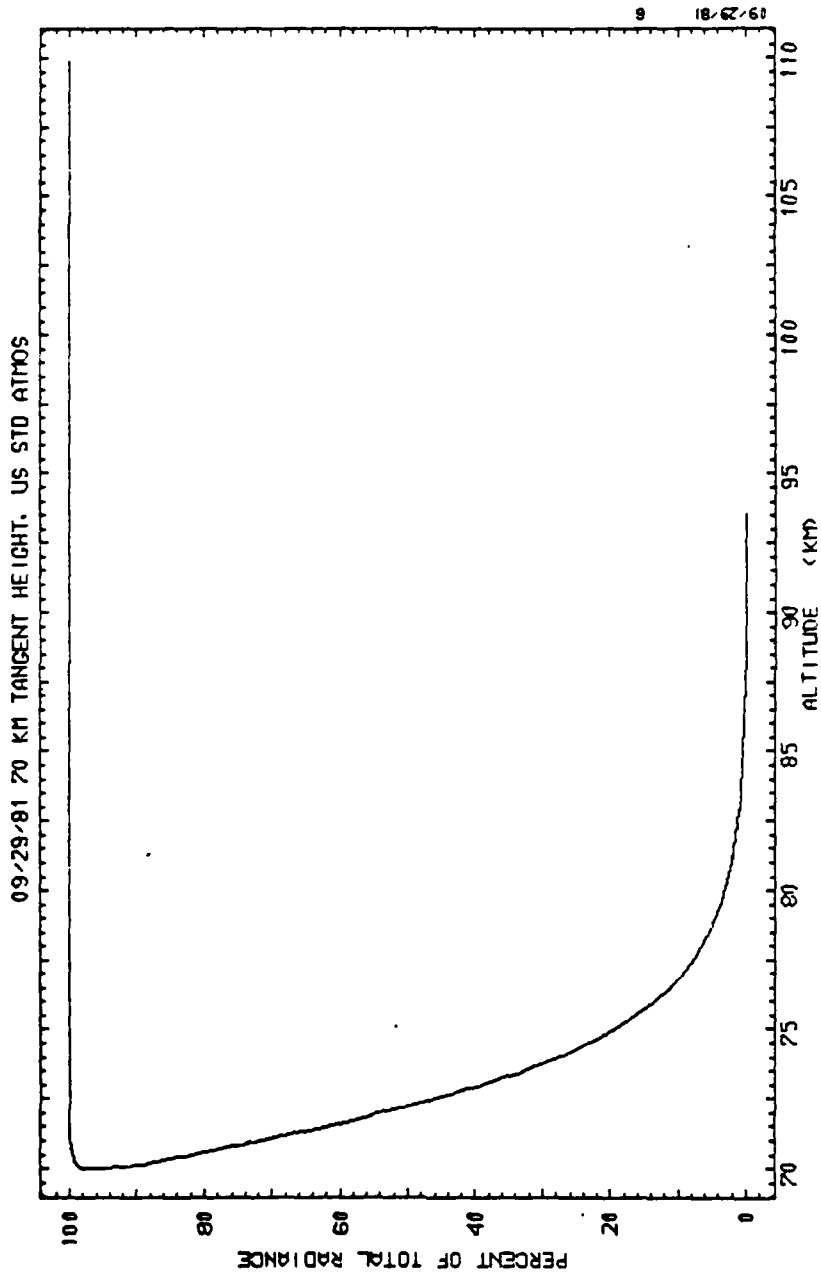


Fig. 46. Cumulative Radiance Profile for
18.57710 cm^{-1}

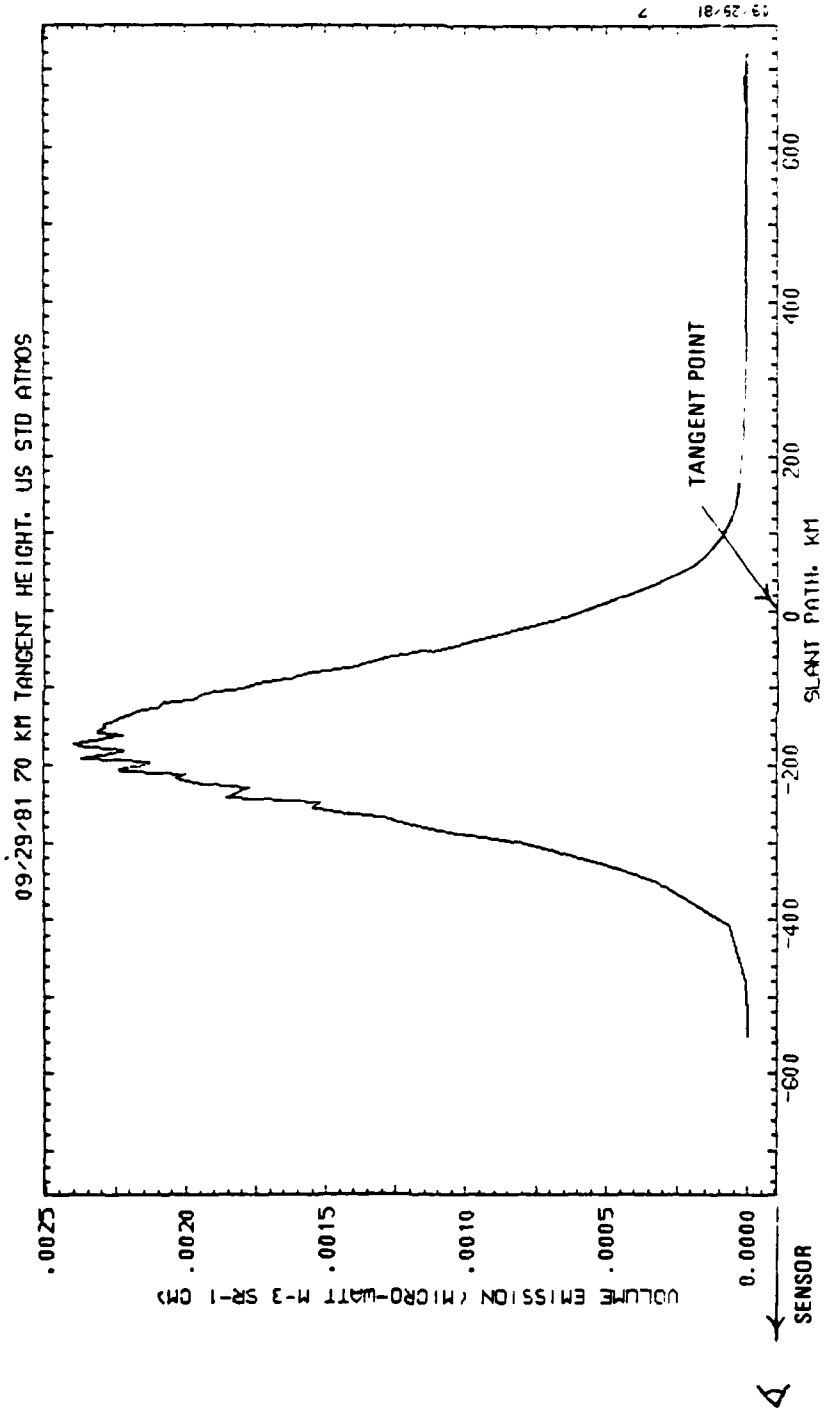


Fig. 47. Slant Path Radiance Profile for
18.57710 cm^{-1}

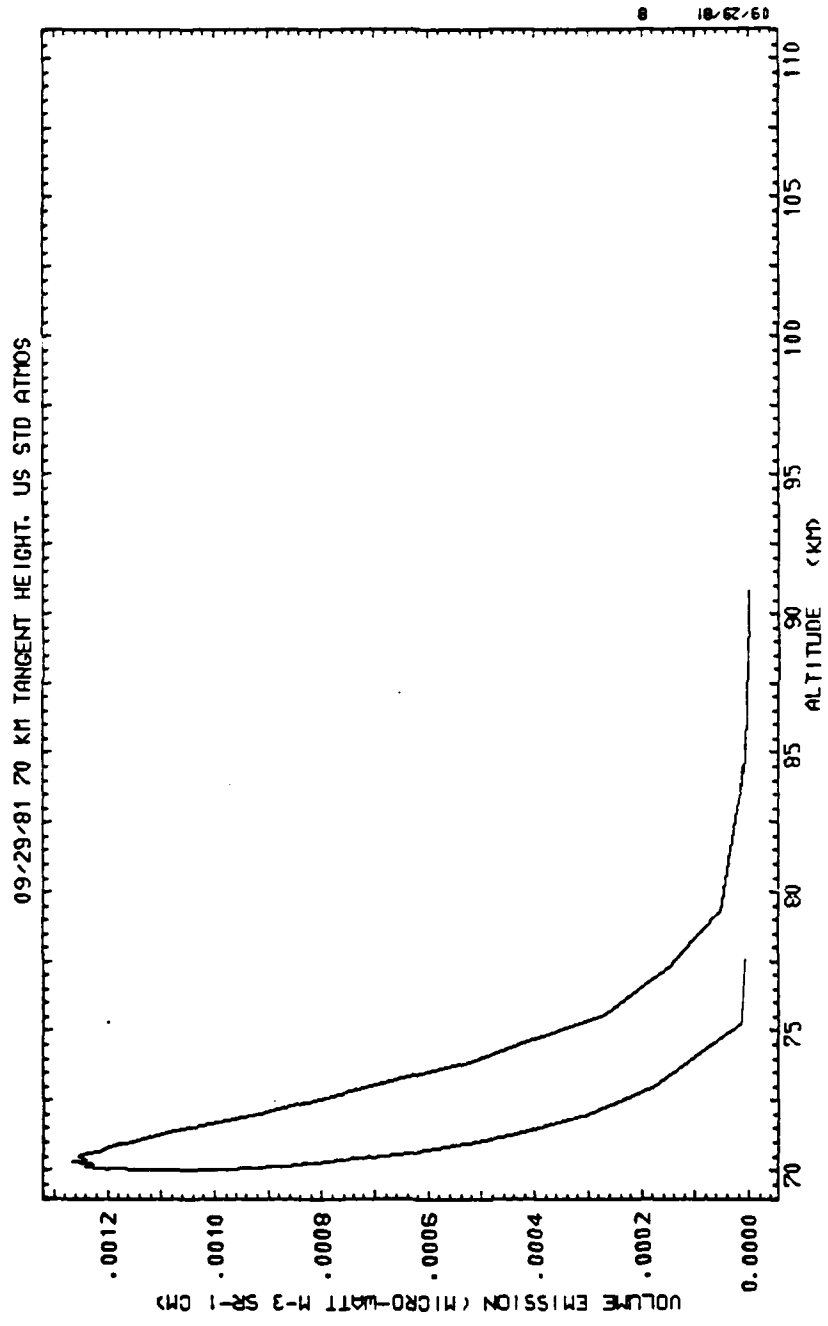
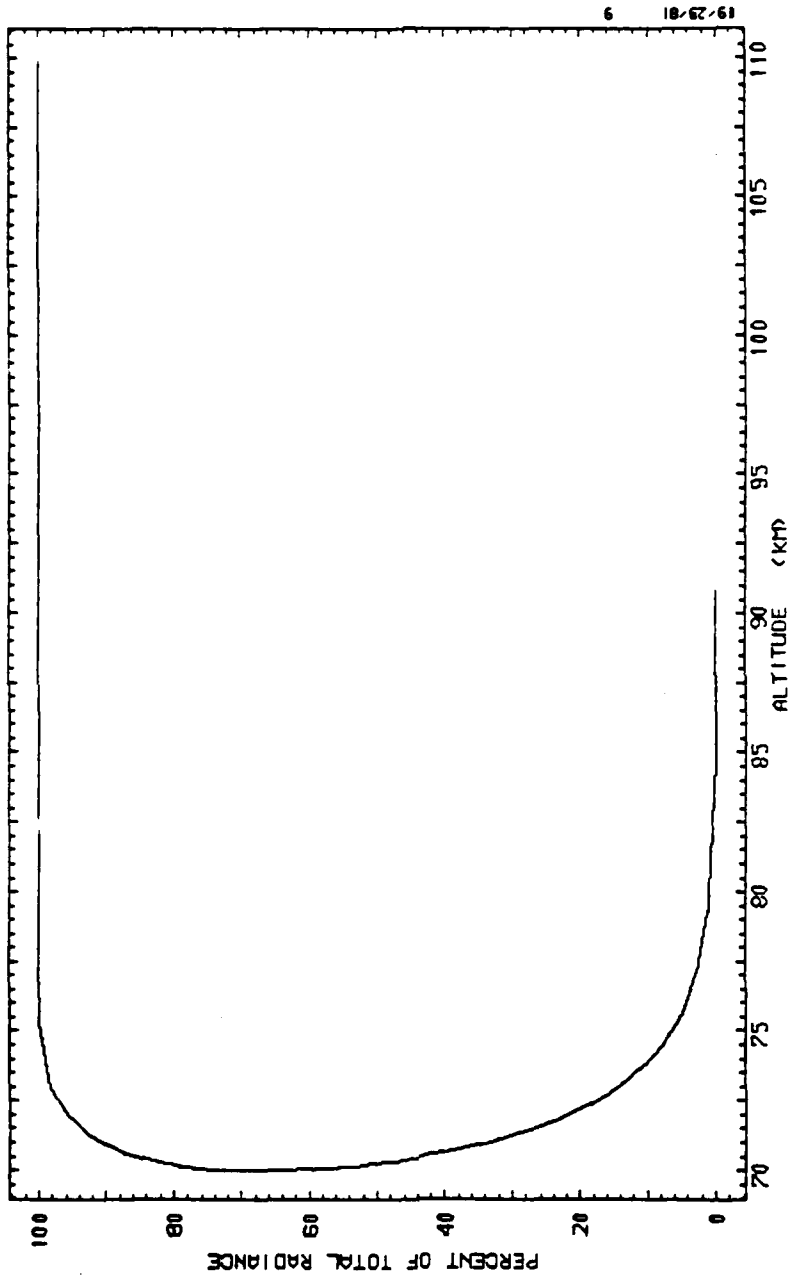


FIG. 48. Radiance Contribution Profile for
18.57720 cm⁻¹

09/29/81 70 KM TANGENT HEIGHT. US STD ATMOS



19/29/81 9

Fig. 49. Cumulative Radiance Profile for 18.57720 cm

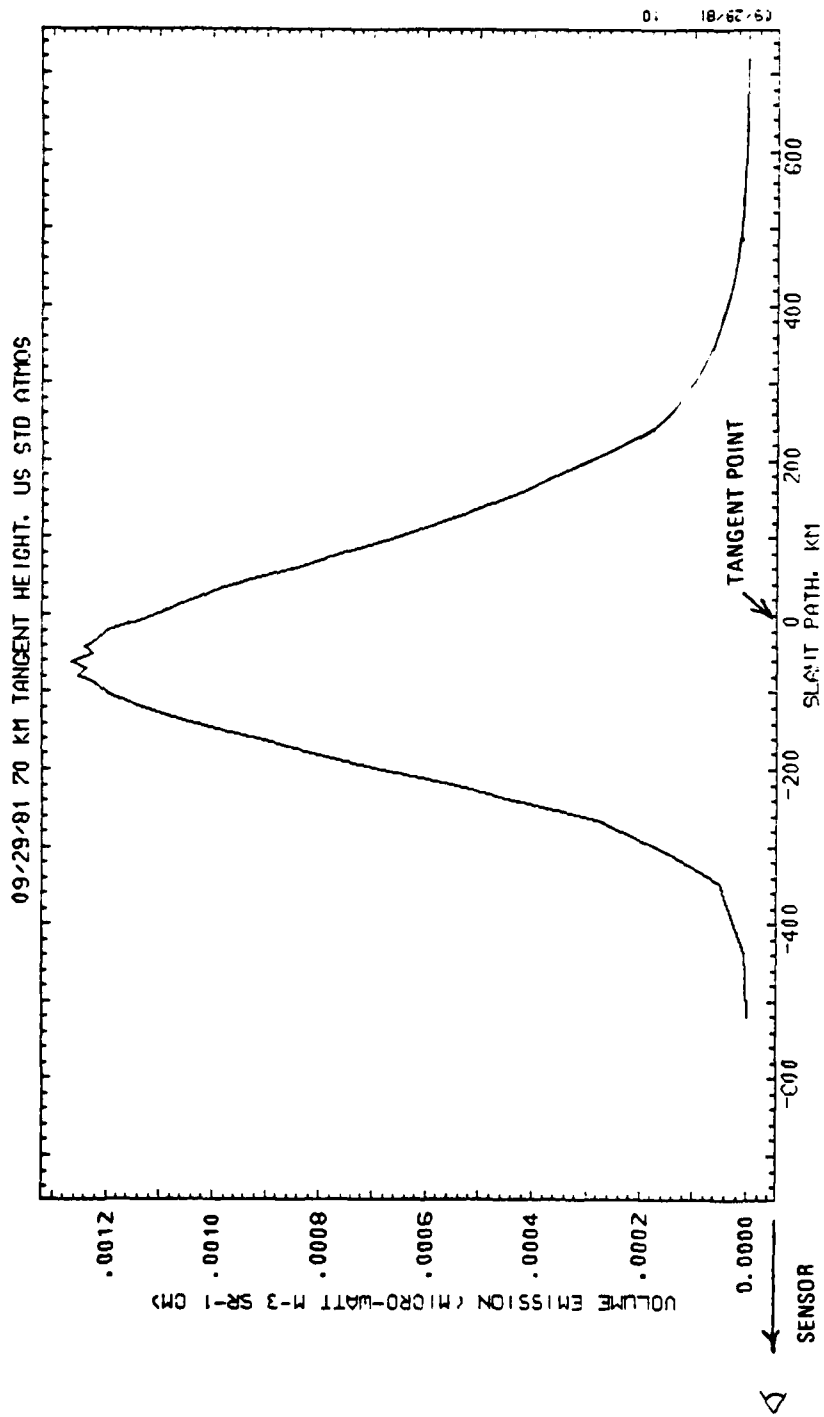


Fig. 50. Slant Path Radiance Profile for
18.57720 cm⁻¹

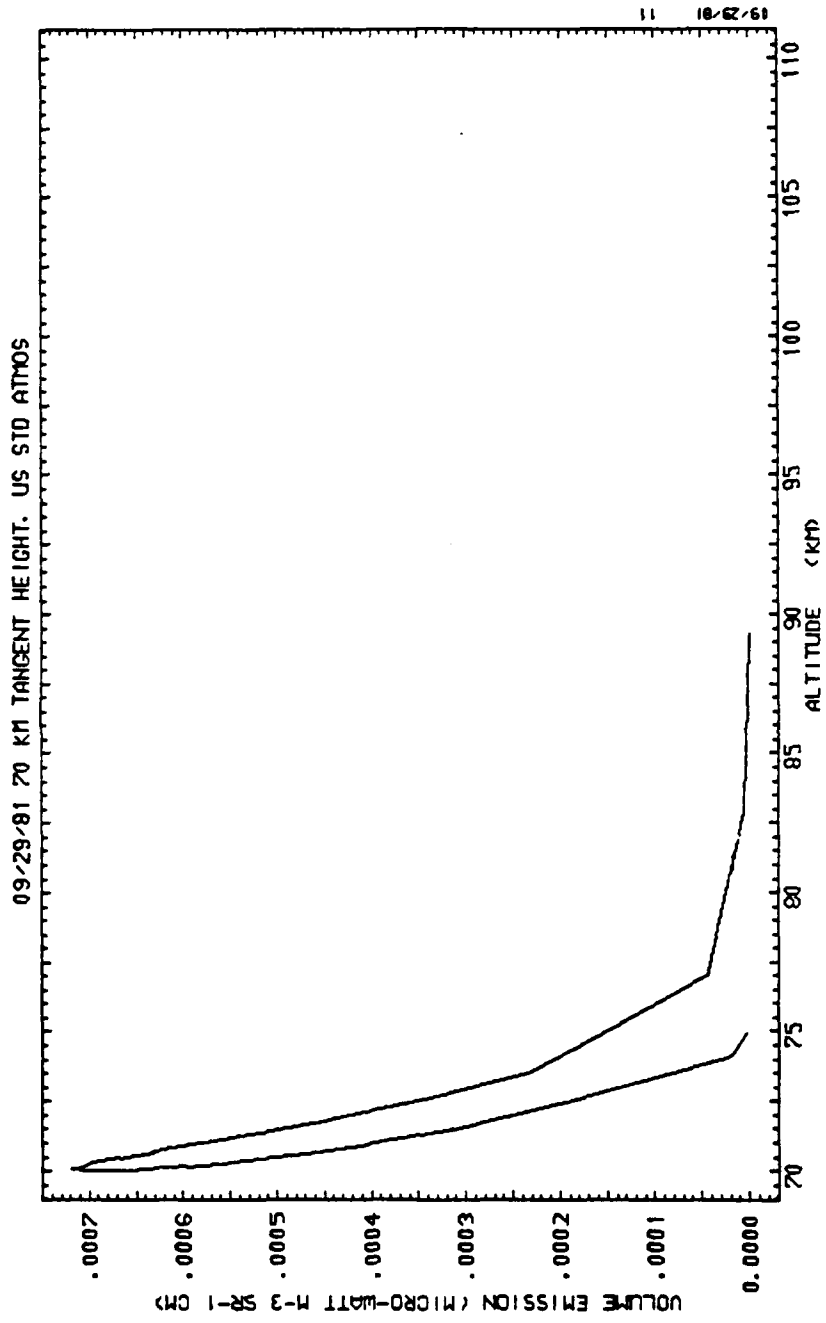


Fig. 51. Radiance Contribution Profile for 18.57730 cm^{-1}

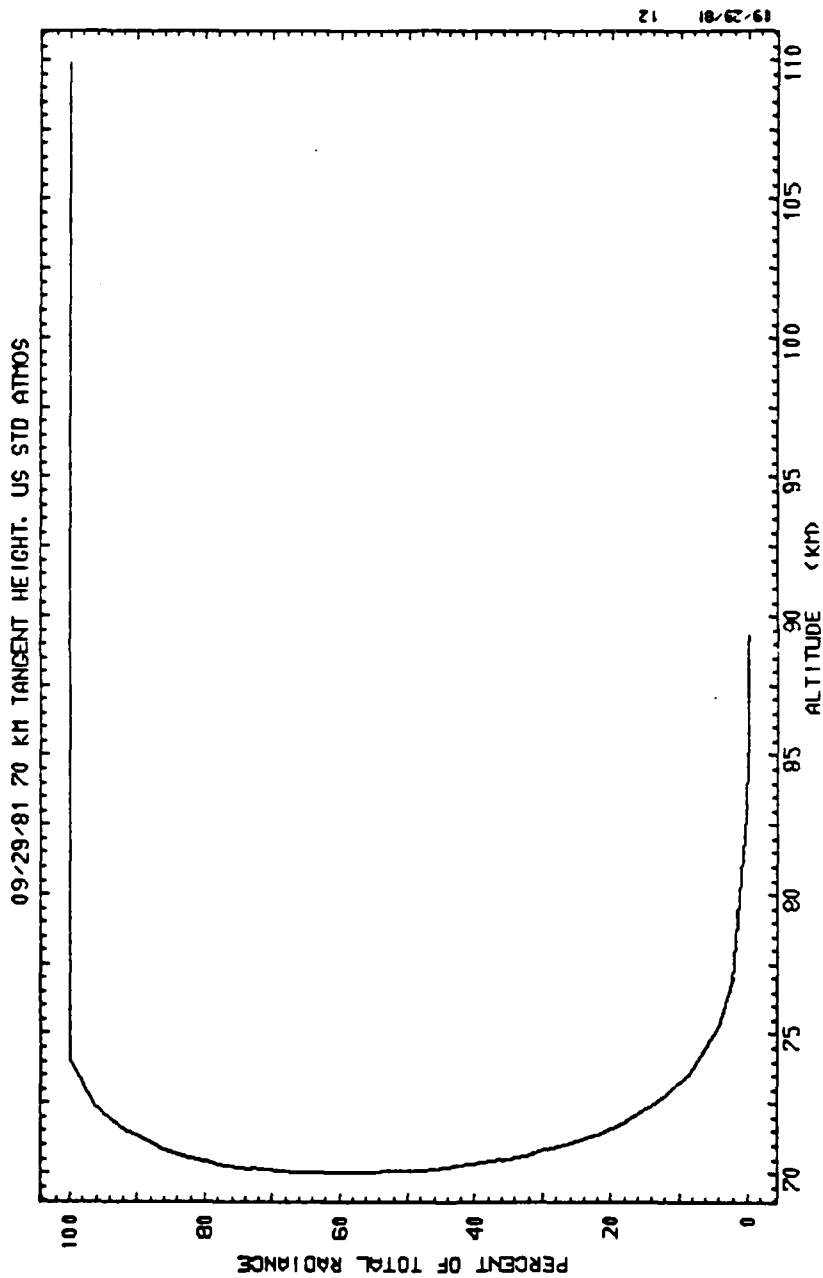


Fig. 52. Cumulative Radiance Profile for
18.57730 cm^{-1}

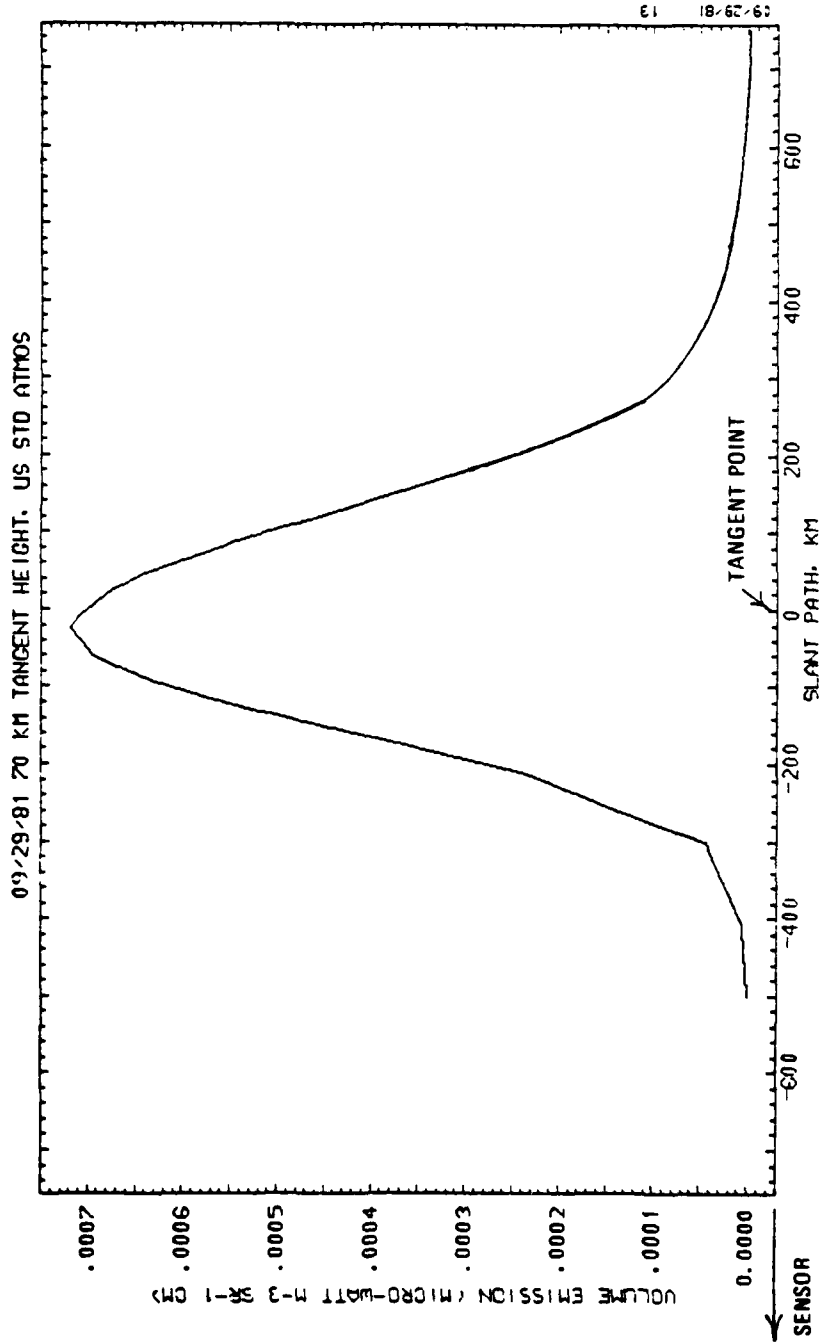


Fig. 53. Slant Path Radiance Profile for
18.57730 cm^{-1}

09/29/81 70 KM TANGENT HEIGHT. US STD ATMOS

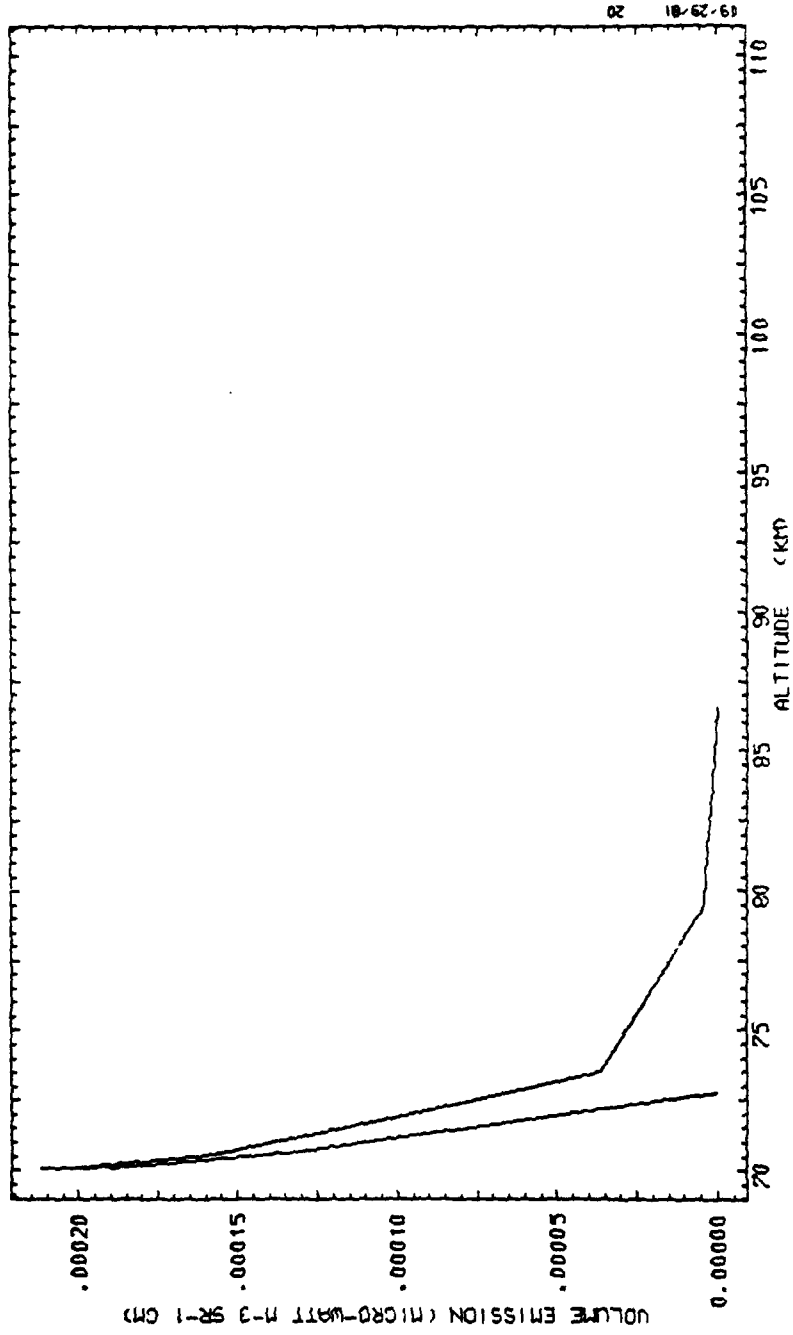


Fig. 54. Radiance Contribution Profile for 18.57760 cm⁻¹

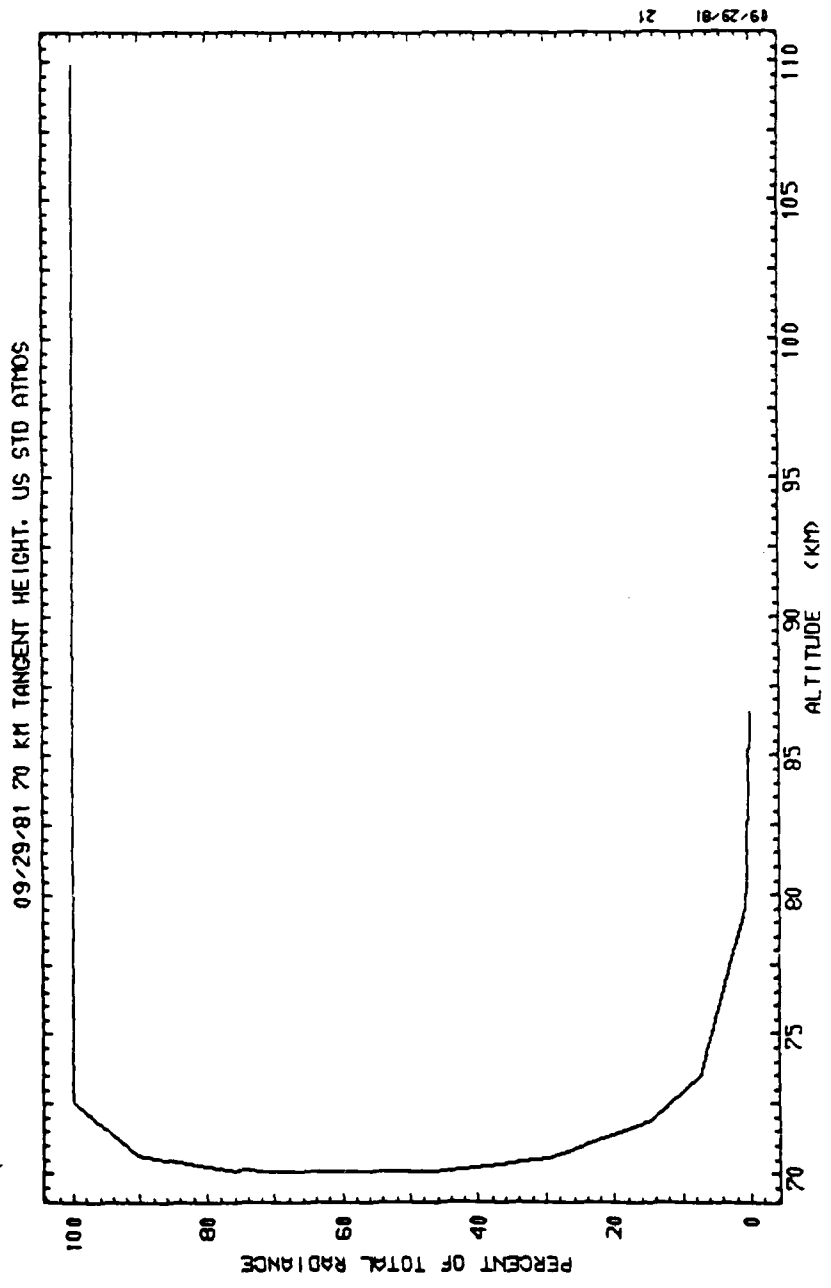


Fig. 55. Cumulative Radiance Profile for
18.57760 cm^{-1}

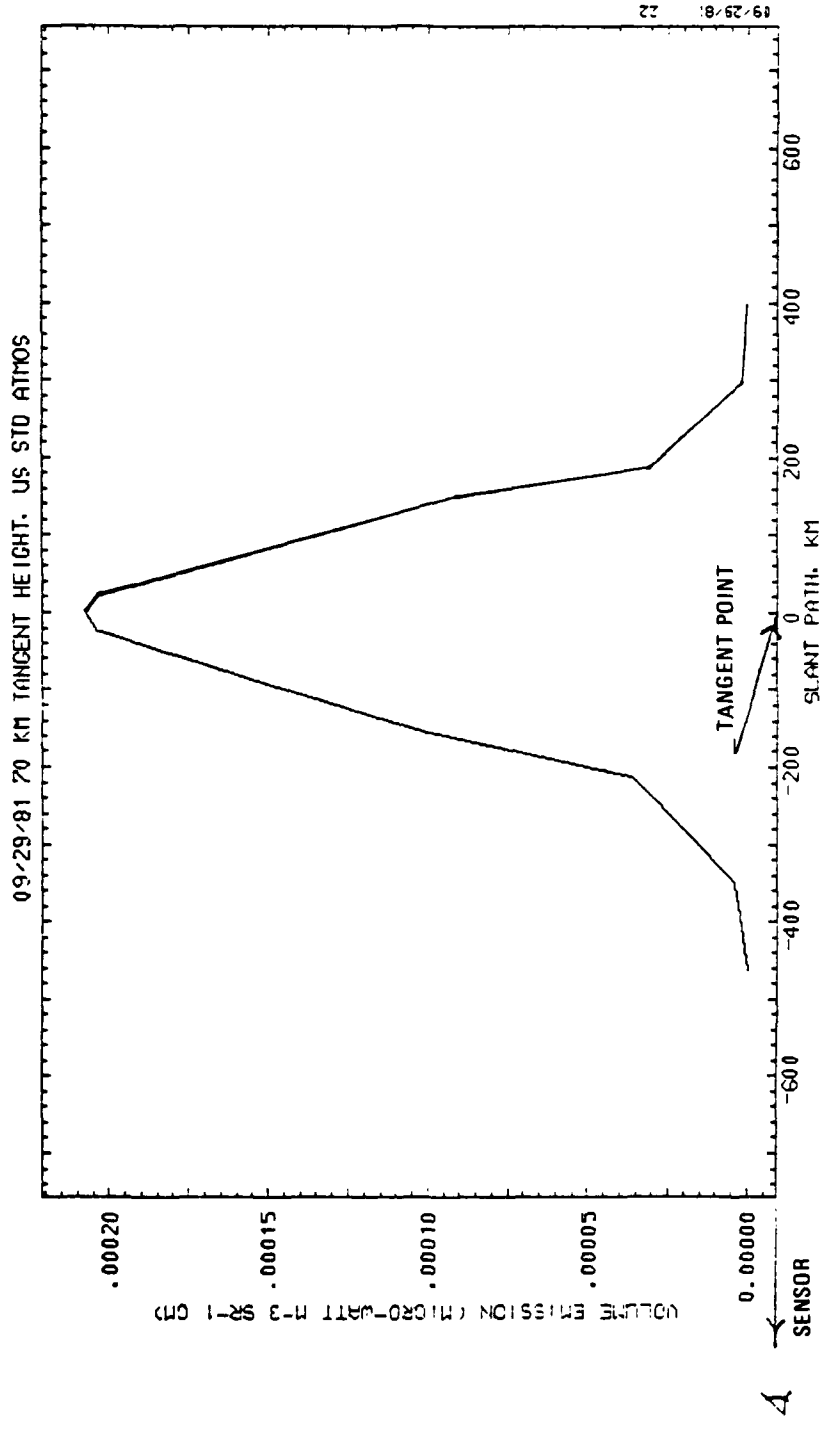


Fig. 56. Slant Path Radiance Profile for 18.57760 cm^{-1}

C. BACKGROUND SIGNATURE VARIABILITY AT SMALLER SCALE SIZES

1. Gravity Waves

The principal source of atmospheric structure of concern here is internal gravity waves, discussed in Sec. III. A. These produce perturbations, sometimes regular and periodic, in the density and temperature of the atmosphere at altitudes in the mesosphere and higher. The effects of gravity waves on atmospheric properties have been observed from the ground through their influence on

- (a) radar echoes from long-lived ionized meteor trails,
- (b) radar echoes from neutral-density gradients of the atmosphere,
- (c) luminosity patterns of noctilucent clouds, and
- (d) spatial and temporal luminosity patterns of the night-time hydroxyl airglow.

The radar measurements give a Doppler spectrum from which wind velocity properties are deduced. Studies of the hydroxyl airglow have been numerous and fruitful because the radiation is bright enough some of the time to be photographed in the near infrared, and because emission spectra can be interpreted for rotational temperature.

The hydroxyl emission occurs primarily in the altitude range from 80 to 100 km (Ref. 11). Horizontal wavelengths vary in the range 4 to 70 km (Ref. 12). Vertical depth of the emission layer varies from 6 to 20 km. Significant temperature changes have been measured down to a 30-sec time interval (Ref. 13). Fluctuations as large as $\pm 50^\circ\text{K}$ have been observed over times of 5 to 10 min (Ref. 14). Crests of single waves up to 600 km long have been observed (Ref. 12).

In two respects, there are reasonable questions about the proper interpretation of these observations. First, there is concern that the rotational-state population in OH may not always be in thermal equilibrium with the atmosphere. However, there is good evidence that thermal equilibrium pertains in most of the spectra. Second, it seems possible that time and spatial variations of rotational temperature may in fact result from a changing altitude of the emission layer in a region of steady temperature gradient in

altitude. If either of these concerns is valid, then the hydroxyl airglow gives at best only limited information relevant to the problem. Both of these issues have been addressed in the recent literature (Refs. 15 through 18), but without resolution.

To be conservative, we shall assume that these observations imply kinetic temperature fluctuations in any spatially fixed volume of space in the emission layer. It is likely that the water vapor rotational temperature varies in space and time in a similar manner.

Lacking a complete statistical description of the variation of temperature and density owing to gravity waves, we have elected instead to do an illustrative calculation using a reasonable approximation. Two calculations of background signature were done using the atmospheric properties as for case 3, Table 2, but with a depressed temperature of the mesopause of $T = 157^{\circ}\text{K}$. This represents a 30°K maximum reduction from the U. S. Standard Atmosphere at 90 km. The assumed temperature distribution is shown in Fig. 12 as the dashed line. No change was assumed for humidity and pressure distributions. Calculations were done for vertical viewing (case 8) and for 70-km tangent height limb viewing (case 9). Background spectral radiances for cases 3, 7, 8, and 9 are compared in Fig. 57. The only change occurs at and near the line center, as would be expected from the weighting functions displayed in Figs. 22 and 42. Because there is a fairly good match in altitude between the weighting functions at the line center and the assumed temperature perturbation, most of the maximum temperature decrement is reflected in the change in background apparent temperature.

The amplitude of gravity waves increases with increasing altitude. There will be some manifestations of gravity waves at altitudes below 80 km, but they will be progressively smaller with decreasing altitude. While there will be larger temperature excursions from gravity waves above 100 km, the atmosphere is optically thin there and these excursions will not affect the background signature.

It appears that spatial variation of temperature and density could have a substantial effect on background signature in the immediate vicinity of the

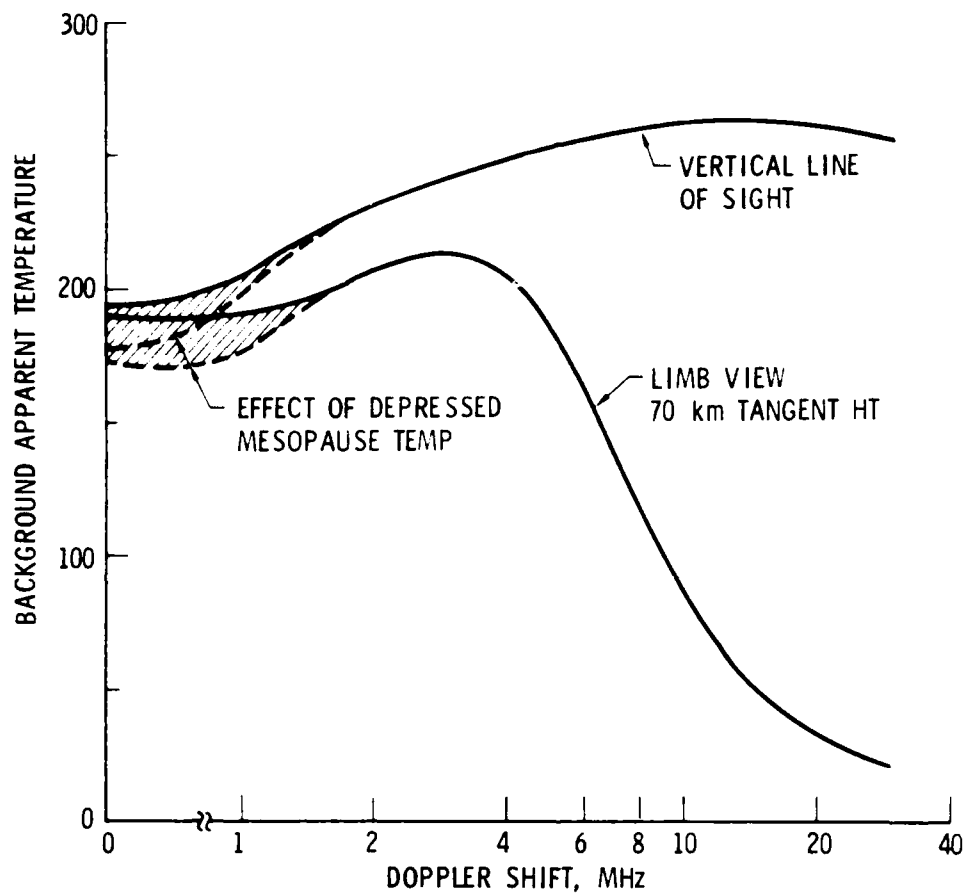


Fig. 57. Effect on Background Spectra of Variation in Mesopause Temperature

line center. To be sure, more calculations are required using more realistic models for the perturbations of temperature and density induced by gravity waves.

2. Turbulence

While turbulence appears to exist in the mesosphere, it is expected to have a negligible effect on the background signature. First, it is horizontally stratified so that a particular turbulence layer will occupy only a small fraction of the altitude range of the weighting function at any frequency, if the line of sight is, say, within 45° of the vertical. If the line of sight is more nearly horizontal, a turbulent layer can occupy a larger fraction of the range of the weighting function, but the full signal will be derived from a long column of turbulent gas over which the integrated effect of small-scale random fluctuations will tend to zero. Because of these geometrical considerations, it is difficult to see how turbulence could have a significant effect on background signatures and it is not considered further here.

IV. CONCLUSIONS

Based on the analyses reported here, it appears that the plumes of small rocket motors at high altitudes can be detected by observing their submillimeter optical properties. However, there are critical issues that have not been addressed here that would require a larger effort and could, depending on their resolution, change this tentative conclusion. These are given in Sec. V.

In the presence of a benign background from the atmosphere, that is, one with no spatial or temporal variation, the estimate outlined in Sec. II. C for a staring detector shows that a 100-lb-thrust motor would be detected with a signal-to-noise ratio of 20 under the assumed conditions and system parameters there specified. Against a background of deep space, the same plume results in a signal-to-noise ratio of about 4, lower because the plume is now being detected in emission rather than in absorption.

The calculations of atmospheric spectral radiance for different distributions of temperature and humidity and different viewing geometries show that the altitude range that gives rise to the background in the spectral range $(18.577 \pm .0006) \text{ cm}^{-1}$ is 35 to 100 km and that the system must be able to cope with a variety of background signatures. These relatively large differences in signature will occur at points separated by distances >1000 km across the earth's disk and, at any one point, over times as short as one day. Differences in background apparent temperature in the range 20 to 50°K can be expected at a particular spectral frequency. The shape of the atmospheric background spectra will change on the same distance and time scales.

On a smaller size scale, gravity waves appear to generate horizontal spatial variations in atmospheric temperature in the altitude range, which gives rise to background radiation that appears at and very close to (± 2 MHz) the line center. When the relative motions of sensor and plume are such that a significant component of the plume absorption is not Doppler shifted away from the line center, the plume detectability may be degraded by these background variations.

The situation is somewhat different when the line of sight passes through the earth limb, as opposed to viewing the always optically thick atmosphere over the earth disc. First, for a tangent height less than 50 km the atmosphere is optically thick at all frequencies of interest and the background is little different from that of vertical viewing. For a tangent height greater than ~ 110 km, the atmosphere probably contributes a negligible background. Between these values, the background spectral signature varies rapidly with tangent height. Because of this variation in background character across the limb, an exhaust plume between the sensor and the limb can appear either in absorption or in emission and the magnitude and sign of the plume signal will be a continuous function of the tangent height of the line of sight. In addition, if there are changes in the signal Doppler shift because of changes in the direction of the thrust vector, and if there are changes in the limb signature in a direction parallel to the earth's surface, one can see that the limb-viewing geometry detection problem is potentially complicated for this system.

V. ISSUES REQUIRING FURTHER STUDY

Some of the issues presented here are critical to the feasibility of this scheme. Others are important to the further understanding of when and how well the system will work. This list is by no means exhaustive. We have specifically excluded issues related to the feasibility and development of hardware, although some of these are suggested by the discussion.

A. CRITICAL ISSUES

1. In all of the foregoing discussion and analyses, it has been explicitly assumed that water vapor is the absorbing plume molecule. Such a scheme requires the presence of both hydrogen and oxygen atoms in the propellant system of the observed plumes. In order to be feasible for different propellant systems, in principle the system could be designed to sense the absorption from a rotational transition in any other major exhaust species having a permanent dipole moment. However, that species probably must also be present in quantity in the mesosphere or stratosphere in order to retain the relatively benign background characteristics found for water. If the species is not present in the upper atmosphere, the sensor will probably view background radiation that originates in the troposphere, where there are large spatial and temporal variations in temperature that create a cluttered background. The situation is illustrated in Fig. 58, which shows the altitude at which the optical depth is unity when viewed vertically from above in the frequency range 10 to 55 cm^{-1} . A note of caution in interpreting this figure: calculations were done only at intervals of 1.0 cm^{-1} , so some strong atmospheric absorption features are not accurately represented in the plot, for example, the 18.577 cm^{-1} line of water. For practical purposes, the question then becomes: Are there current or possible future bus engine propellant systems that do not produce substantial fractions of water vapor? If so, this scheme will probably not work as well for those motors.

2. There is strong evidence from observations of solar scattering of visible wavelengths at high altitudes that at least some condensation of water occurs in an exhaust plume. However, it is also known from infrared signatures

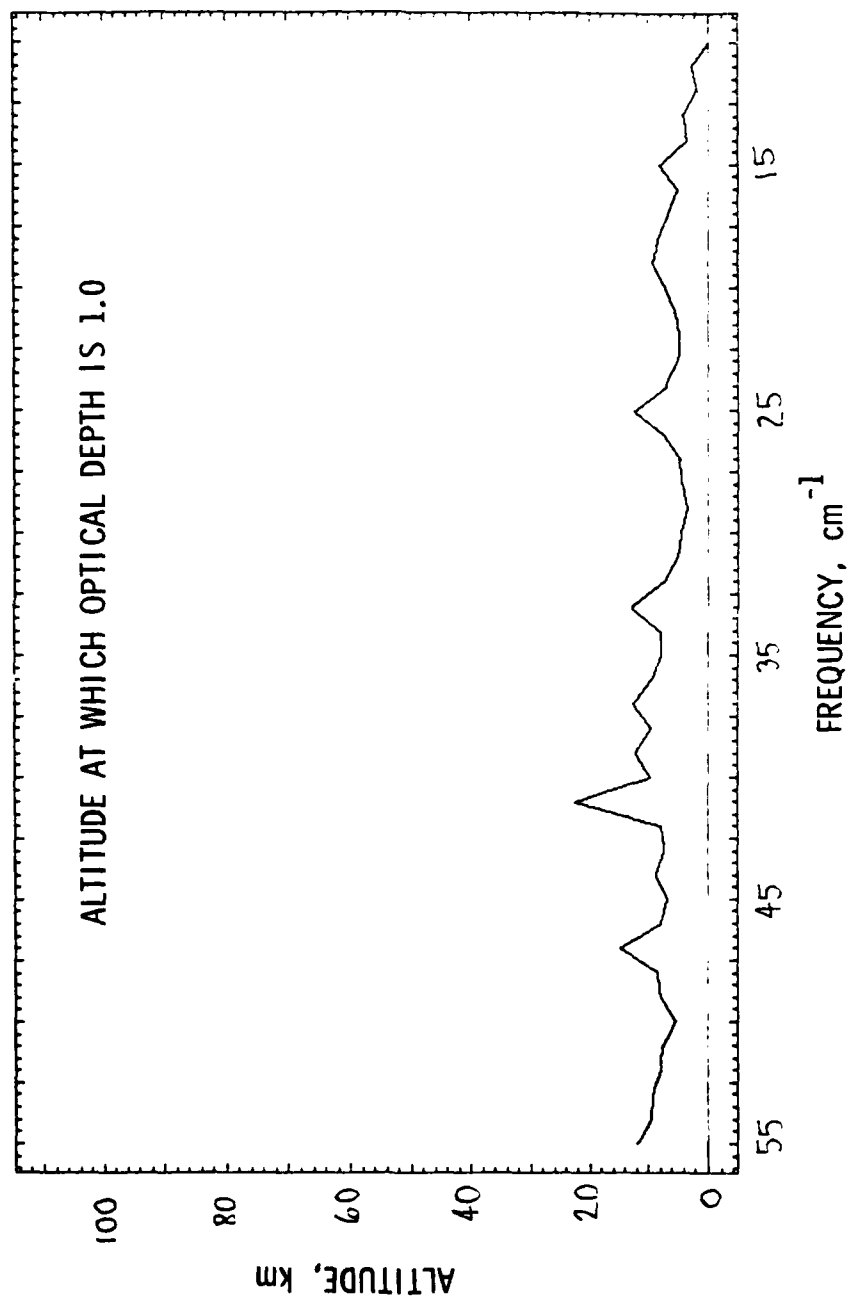


Fig. 58. Altitude at Which Optical Depth is 1.0

that most of the water is present as vapor in the plumes of larger motors. Clearly it is necessary that this be so for the smaller motors of interest here for the scheme to be feasible. In light of the apparent presence of condensed-phase water, it seems prudent to ascertain the quantity and distribution of vapor-phase water in the plumes of interest.

B. OTHER ISSUES

Provided that the two critical issues above can be resolved satisfactorily, other issues that need attention are as follows:

1. A detailed study of the relative merits of this and competing schemes is needed. Competing schemes that should be considered include the SWIR systems, as well as MWIR, LWIR, UV, and visible light systems.
2. The wind heating model used in Sec. II will cease to be even approximately valid below some altitude. Further studies are needed to characterize the performance of this system at the low end of the altitude range where it will function.
3. Comprehensive measurements are needed of the earth background signature in different viewing geometries, in different seasons, and in different parts of the globe at and near the center of the rotational lines of interest. These should include measurements of spatial and temporal spectra.
4. A computer model should be developed for calculating plume signals for arbitrary orientation of the plume axis and the vehicle velocity vectors in the presence of realistic background spectra.
5. Algorithms need to be developed for identification of plume signals in the presence of varying background signatures.

REFERENCES

1. M. M. Litvak, J. A. Weiss, and G. F. Dionne, "Submillimeter Wave Properties of Thermospheric Rocket Plumes," Int. J. of Infrared and Millimeter Waves 1, (4), 561-579 (1980).
2. M. A. Geller, "Dynamics of the Middle Atmosphere," J. Atmos. Terr. Phys. 41, 683-705 (1979).
3. J. C. Gille, "Middle Atmosphere Processes Revealed by Satellite Observations," J. Atmos. Terr. Phys. 41, 707-722 (1979).
4. C. O. Hines, "Motions in the Ionospheric D and E Regions," Phil. Trans. Roy. Soc. Lond. A 271, 457-471, (1972).
5. D. Rees, R. G. Roper, K. H. Lloyd, and C. H. Low, "Determination of the Structure of the Atmosphere Between 90 and 250 km by Means of Contaminant Releases at Woomera, May 1968," Phil. Trans. Roy. Soc. Lond. A 271, 631-663 (1972).
6. "U. S. Standard Atmosphere, 1976," U. S. Government Printing Office, Washington, D. C., (1976).
7. A. J. Kantor and A. E. Cole, "Monthly 90°N Atmospheres and High-Latitude Warm and Cold Winter Stratosphere/Mesosphere," Air Force Geophysics Laboratory, AFGL-TR-77-0289, 14 Dec. 1977. See Fig. 6, pg. 18; this is an example of a warm mesosphere and cold stratosphere.
8. A. J. Kantor and A. E. Cole, "Monthly Midlatitude Atmospheres, Surface to 90 km," Air Force Geophysics Laboratory, AFGL-TR-76-0140, 23 June 1976. For 45°N, July, see Table 2b; this is an example of a cold mesosphere.
9. This is a composite water distribution of our own choosing, but based on a summary of experimental data reviewed in the paper by H. W. Ellsaesser, J. E. Harries, D. Kley, and R. Penndorf, "Stratospheric H₂O," Planet. and Space Sci. 28, 827-835 (1980). In the altitude range from 45 to 70 km it is identical with the findings of H. E. Radford, M. M. Litvak, C. A. Gottlieb, E. W. Gottlieb, S. K. Rosenthal, and A. E. Lilley, J. Geophys. Res. 82, 472 (1977), with their 6.67-MHz bandwidth.
10. P. Crutzen, "A Review of Upper Atmospheric Photochemistry," Can. J. Chem. 52, 1569 (1974). We used the dashed line in Fig. 7.
11. A. Vallance-Jones, "The Infrared Spectrum of the Airglow", Space Sci. Rev. 15, 355, (1973).
12. G. Moreels, M. Herse, "Photographic Evidence of Waves Around the 85 km Level," Planet. Space. Sci. 25, pgs. 265-273, (1977).

13. M. V. Shagaev, "Fast Variations of Hydroxyl Night Airglow Emission," J. Atmos. Terr. Phys. 36, 367-71 (1974).
14. V. I. Krassovsky and M. V. Shagaev, "Inhomogeneities and Wavelike Variations of the Rotational Temperature of Atmospheric Hydroxyl," Planet. Space Sci. 22, 1334-37, (1974).
15. K. A. Dick, "On the Rotational Temperature of Airglow Hydroxyl Emissions," Planet. Space Sci. 25, 595 (1977).
16. V. I. Krassovsky et. al., "On the Equilibrium Nature of the Rotational Temperature of Hydroxyl Airglow," Planet. Space Sci. 25, 596 (1977).
17. B. P. Potapov, "Determination of the Effective Height of Fluctuations of Hydroxyl Emissions," Planet. Space Sci. 23, 1346, (1975).
18. L. Wallace, "The OH Nightglow Emission," J. Atmos. Sci. 19 (1), 1-16, (1962).

LABORATORY OPERATIONS

The Laboratory Operations of The Aerospace Corporation is conducting experimental and theoretical investigations necessary for the evaluation and application of scientific advances to new military space systems. Versatility and flexibility have been developed to a high degree by the laboratory personnel in dealing with the many problems encountered in the nation's rapidly developing space systems. Expertise in the latest scientific developments is vital to the accomplishment of tasks related to these problems. The laboratories that contribute to this research are:

Aerophysics Laboratory: Launch vehicle and reentry aerodynamics and heat transfer, propulsion chemistry and fluid mechanics, structural mechanics, flight dynamics; high-temperature thermomechanics, gas kinetics and radiation; research in environmental chemistry and contamination; cw and pulsed chemical laser development including chemical kinetics, spectroscopy, optical resonators and beam pointing, atmospheric propagation, laser effects and countermeasures.

Chemistry and Physics Laboratory: Atmospheric chemical reactions, atmospheric optics, light scattering, state-specific chemical reactions and radiation transport in rocket plumes, applied laser spectroscopy, laser chemistry, battery electrochemistry, space vacuum and radiation effects on materials, lubrication and surface phenomena, thermionic emission, photosensitive materials and detectors, atomic frequency standards, and bioenvironmental research and monitoring.

Electronics Research Laboratory: Microelectronics, GaAs low-noise and power devices, semiconductor lasers, electromagnetic and optical propagation phenomena, quantum electronics, laser communications, lidar, and electro-optics; communication sciences, applied electronics, semiconductor crystal and device physics, radiometric imaging; millimeter-wave and microwave technology.

Information Sciences Research Office: Program verification, program translation, performance-sensitive system design, distributed architectures for spaceborne computers, fault-tolerant computer systems, artificial intelligence, and microelectronics applications.

Materials Sciences Laboratory: Development of new materials: metal matrix composites, polymers, and new forms of carbon; component failure analysis and reliability; fracture mechanics and stress corrosion; evaluation of materials in space environment; materials performance in space transportation systems; analysis of systems vulnerability and survivability in enemy-induced environments.

Space Sciences Laboratory: Atmospheric and ionospheric physics, radiation from the atmosphere, density and composition of the upper atmosphere, aurorae and airglow; magnetospheric physics, cosmic rays, generation and propagation of plasma waves in the magnetosphere; solar physics, infrared astronomy; the effects of nuclear explosions, magnetic storms, and solar activity on the earth's atmosphere, ionosphere, and magnetosphere; the effects of optical, electromagnetic, and particulate radiations in space on space systems.